FABRICATION, PACKAGING, AND APPLICATION OF MICROMACHINED HOLLOW POLYMER NEEDLE ARRAYS

A Dissertation
Presented to
The Academic Faculty

by

Po-Chun “Kirk” Wang

In Partial Fulfillment
of the Requirements for the Degree
Doctor of Philosophy in the
School of Electrical and Computer Engineering

Georgia Institute of Technology
December 2013

FABRICATION, PACKAGING, AND APPLICATION OF MICROMACHINED HOLLOW POLYMER NEEDLE ARRAYS

Approved by:

Dr. Mark G. Allen, Advisor
School of Electrical and Computer Engineering
Georgia Institute of Technology

Dr. David C. Keezer
School of Electrical and Computer Engineering
Georgia Institute of Technology

Dr. Muhannad S. Bakir
School of Electrical and Computer Engineering
Georgia Institute of Technology

Dr. Mark R. Prausnitz
School of Chemical and Biomolecular Engineering
Georgia Institute of Technology

Dr. Pamela T. Bhatti
School of Electrical and Computer Engineering
Georgia Institute of Technology

Date Approved: November 10, 2013

To my parents, Su-Ni Lin and Kuo-Lung Wang,
for their endless love.

ACKNOWLEDGEMENTS

I would like to thank Dr. Mark Allen for his kind and patient guidance throughout my doctoral study. Observation of his dedication to the research, his demonstration of critical thinking and leadership composes a crucial part of my doctoral study.

Most of the experiments in this research are performed in the cleanroom facilities of the Pettit Microelectronic Research Center and the Marcus Nanotechnology Research Center at the Georgia Tech. Management of these facilities by Gary Spinner and support from his team to ensure all equipments are up and running are highly appreciated. I also would like to thank Purnima Sharma for her professional administration and Richard Shafer for his help and lab supervision in Dr. Allen's research group (the MSMA group). Valuable discussions and expertise from MSMA group members, including Dr. Seong-Hyok Kim, Dr. Florian Herrault, Dr. Swaminathan Rajaraman, Dr. Seung-Joon Paik, Dr. Shuodan Chen, and Dr. Jungkwun Kim, are greatly appreciated. Moreover, I would like to thank Dr. Jeong Woo Lee for his instruction and help on a force-displacement test station and Dr. James Norman for his help on working with skin tissues. Both Dr. Lee and Dr. Norman are with the Laboratory for Drug Delivery at the Georgia Tech and directed by Dr. Mark Prausnitz, whose research explores the application potential of microneedles and is greatly appreciated.

Company from current and previous MSMA Ph.D. students, including Andac Armutlulu, Jooncheol Kim, Minsoo Kim, Yuan Li, Mengdi Luo, Brock Peterson, Chao Song, Melissa Tsang, Xuehong (Shannon) Yu, Dr. Preston Galle, Dr. Wenjun Xu, Dr. Brock Wester, Dr. Zhan (Jennifer) Liu, Dr. Nisarga Naik, and Dr. Maxine McClain is

greatly appreciated, for their company both in the lab and in the office supports me through endless days and nights.

I would like to extend my special thanks to my wife, Wei-Ning Shih, for her love, support, and encouragement throughout my Ph.D. study. I also would like to extend special thanks to my three-year-old son, Joshua, for through his eyes I see another purpose of life.

TABLE OF CONTENTS

Page

LIST OF TABLES

Page

LIST OF FIGURES

Page

LIST OF ABBREVIATIONS

BD	Becton Dickinson
BSV	Backside vacuuming
CMC	Carboxymethylcellulose
CAD	Computer-aided design
DC	Dendritic cell
DRIE	Deep reactive ion etching
DXRL	Deep X-ray lithography
FDA	Food and Drug Administration
HMN	Hollow microneedle
HMP	2-hydroxy-2-methyl-propiophenone
HN	Hypodermic needle
HNL	Hypodermic-needle-like
IPA	Isopropyl alcohol
LC	Langerhans cell
MN	Microneedle
NMP	N-methyl-2-pyrrolidone
NRS	Numerical rating scale
PDMS	Polydimethylsiloxane
PEB	Post-exposure bake
PEG	Polyethylene glycol
PEGDA	Polyethylene glycol diacrylate
PET	Polyethylene terephthalate

PGA	Polyglycolic acid
PGMEA	Propylene glycol methyl ether acetate
PMMA	Polymethyl methacrylate
POM	Polyoxymethylene
PT	Pyramidal tip
PTH	Parathyroid hormone
PU	Polyurethane
PVA	Polyvinyl alcohol
PVP	Polyvinylpyrrolidone
RIE	Reactive ion etching
SC	Stratum corneum
SEM	Scanning electron microscope
SMN	Solid microneedle
UD	Upper dermis
UV	Ultraviolet
VAS	Visual analog scale
VE	Viable epidermis
3D	Three-dimensional

SUMMARY

The aim of this research is to demonstrate that micromachined hollow polymer needle arrays fabricated using UV lithography into micromolds, a potential batch-manufacturable process, can exhibit comparable insertion and injection performance to conventional hypodermic needles for drug delivery into skin.

A dual-exposure-and-single-development process flow is proposed for the above-mentioned UV lithography into micromolds approach to construct a pyramidal-tip hollow microneedle array with an integral baseplate and fluidic manifold. The developed process ultimately resulted in the ability to fabricate a 10×10 array of hollow SU-8 microneedles measuring 825 μm in height, 400 μm in width, and possessing a lumen of 120 μm in diameter. The tip diameter of the microneedles ranges from 15 μm to 25 μm. Mechanical characterization shows the pyramidal tip of the fabricated microneedles fractures against a rigid surface at a driving force of 12.0 ± 0.8 N. The insertion force of single needles characterized using excised porcine skin as a substrate is 2.4 ± 1.2 N. Moreover, the application of a 90 N force on a single needle against excised porcine skin causes minor tip deformation with no fracture observed under an optical microscope, leading to a margin of safety (ratio of fracture force to insertion force) higher than 37. Nevertheless, the high insertion force of 2.4 N per needle may cause a significant concern when a large number of needles are required to insert into skin for drug delivery.

Conventional hypodermic needles have two key structural characteristics: a sharp beveled tip and a large side-terminated lumen. The sharp beveled tip reduces insertion

force and pain perceived by patients, while the large side-terminated lumen provides a large fluid uptake area in the skin and reduces susceptibility to tissue clogging during insertion. Integration of these two key characteristics of hypodermic needles into microneedle design can potentially enhance microneedle performance. To reduce the insertion force and to incorporate the two key characteristics of hypodermic needles into the design of microneedles, a new needle tip design, namely the hypodermic-needle-like design, is presented. With the change from a pyramidal mold to a beveled one, the geometry of the microneedle tip can be optimized three-dimensionally with two dimensions from the design of the photomask pattern and one dimension from the slope angle of the beveled mold. A 6 × 6 array of hypodermic-needle-like microneedles of 1 mm in height, approximate 350 μm in width, and with a lumen of 150 μm in diameter is demonstrated with successful insertion of the needle array into skin and an 85% lumen openness yield. The insertion force is significantly reduced by an order of magnitude with the new needle tip design and is 0.275 ± 0.113 N per needle, comparable to that of hypodermic needles, i.e., 0.284 ± 0.059 N. The hypodermic-needle-like microneedles exhibit a margin of safety of 180 for successful needle insertion into skin prior to needle fracture. A successful manual fluid injection into skin using single microneedle is demonstrated.

The micromachined hypodermic-needle-like polymer needle arrays presented in this dissertation are fabricated using UV lithography into micromolds, a potentially batch-manufacturable process, and exhibit comparable insertion performance to conventional hypodermic needles. Injection capability into skin is also demonstrated with a hypodermic-needle-like microneedle, illustrating the utility of these devices.

CHAPTER 1

INTRODUCTION

Two popular approaches to drug delivery are oral administration and needle injection. Because of enzymatic degradation in the gastrointestinal tract, oral administration may not be feasible for delivery of drugs that are made of macromolecules. [1, 2] When oral administration is not suitable for drug delivery, an injection using a hypodermic needle (HN) is commonly utilized. This is often painful and typically also requires the intervention of healthcare professionals.

The pain or discomfort caused by the insertion of an HN into the skin is attributed to the direct contact between the HN and the nerve fibers, which reside primarily in the dermis of the skin. [3] Significantly reducing the dimensions of a needle can make the insertion of a needle into the skin much less perceptible. [4] The concept of using needles with micrometer dimensions for drug delivery into the skin can be traced back to a patent granted in 1976. [5] Nevertheless, no empirical demonstration of this concept was reported in the 1970s and 1980s, since no fabrication technique was available to construct such microscopic structures during this period of time.

With the advent of high-precision microelectronics industrial tools and microfabrication techniques in the 1990s, it became possible to create microscopic structures with micrometer dimensions. [3] Microneedles (MNs) constructed by using microfabrication techniques were reported by Hashmi et al. and Henry et al. in 1995 and 1998, respectively. [6, 7]

An illustration of a cross section of human skin and a pathway created by the insertion of an MN is shown in Figure 1. To deliver drugs into skin, MNs are first pressed perpendicularly against skin, followed by the rupture of the outermost layer of skin, which is the stratum corneum (SC). The SC has a thickness of 10-20 μm in human skin and forms a substantial barrier to essentially all high-molecular-weight drugs. [2, 8] Underneath the SC are the viable epidermis (VE) of 50-100 μm thickness, and the dermis with a thickness of 1-2 mm. With the rupture of the SC, pathways to the VE or upper dermis (UD) are subsequently created by the further penetration of MNs, followed by the delivery of drugs to the VE or UD.

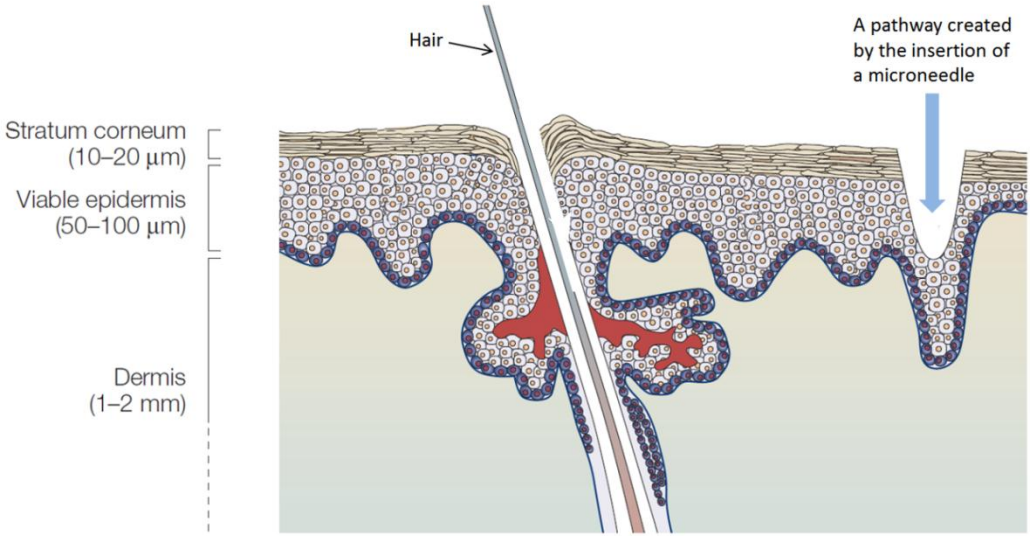

Figure 1. A schematic depiction of a cross section of human skin and a pathway created by the insertion of an MN. [8]

In addition to the painless insertion of MNs reported in human studies, potential advantages of MNs include blood-free insertion, minimal skin trauma, non-skilled / self-administration, reduced risk of needle-stick injury, and ease of disposal. [8, 9]

In addition to the delivery of traditional drugs, an additional potential application of microneedles is vaccine delivery. The immune system, protecting the body against foreign invaders, consists of two interconnected systems: innate immunity and adaptive immunity. [10] When pathogens enter the body through a breach in the epidermis, Langerhans cells (LCs) in the epidermis, dendritic cells (DCs) and macrophages in the dermis engulf and destroy pathogens. These immune responses constitute the innate immunity in the skin. The LCs and DCs subsequently migrate to lymph nodes, where they present pathogen-derived antigens to naive T cells, initiating adaptive immune responses against pathogens. Adaptive immunity provides the body with broader responses to pathogens and a means of retaining memory of past pathogens. [11] The purpose of vaccination is to initiate the development of long-lasting adaptive immunity against specific pathogens. Recent studies suggest that MN delivery of drugs targets the LCs and/or DCs in the skin, leading to the subsequent activation of adaptive immune responses.[12-14]

Drug delivery with MNs has been shown to induce immune responses or biological effects that are comparable to those induced by an HN injection in animal studies with influenza, Hepatitis B, Hepatitis C, and diabetes. [1, 15, 16] In addition, one human study with influenza reported that the influenza vaccines delivered with MNs produced immune responses similar to those from an HN vaccination. [17]

MNs can be categorized into two groups, solid microneedles (SMNs) and hollow microneedles (HMNs), depending on the absence or presence of a needle lumen, respectively. HMNs allow aqueous drugs to flow through the lumen and into the skin, leading to faster rates of drug delivery than those with SMNs that rely on the diffusion of

drugs into the skin. [1] Moreover, with HMNs, it is possible to deliver drugs to a well-defined depth in the skin, and the depth can be controlled by the location of the lumen opening. By adjusting the flow rate with a syringe or pump [4], well-controlled drug delivery over time, e.g., an intermittent delivery, is possible. Nevertheless, the fabrication of HMNs involves a more elaborate process than that of SMNs because of the need for construction of the lumen.

The objectives of a previous dissertation [18] were to develop fabrication processes for SMNs and to integrate metal traces into SMNs for electroporation. In this dissertation, new fabrication processes for HMNs based on those fabrication techniques developed in the previous dissertation are developed. The aim of this research is to demonstrate that micromachined hollow polymer needle arrays fabricated using ultraviolet (UV) lithography into micromolds, a potential batch-manufacturable process, can exhibit comparable insertion and injection performance to conventional hypodermic needles for drug delivery into skin.

The literature on both SMNs and HMNs is reviewed in Chapter 2 to provide a complete overview of the microfabrication and packaging involved in the MN researches.

In Chapter 3, a polymer-based fabrication process using UV lithography into micromolds is presented, allowing the fabrication of microneedle shafts, tips, lumens, and substrate baseplate using lithography. Using UV lithography into micromolds allows complex three-dimensional structures to be defined, since both mask patterns and mold topography are available to define the structures. A hollow microneedle array and baseplate, in which the needle lumens extend through the thickness of the baseplate, is demonstrated. Fabricated polymer microneedles are 825 μm in height and 400 μm in

width, with a pyramidal tip (PT); the needle lumen 120 μm in diameter intersects with one of the faces of the pyramidal tip. Mechanical characterization of the fabricated microneedles shows that the fracture force of a single needle against a rigid surface is 12.0 N. The insertion force of a single needle into porcine skin is empirically determined as 2.4 N. The fracture force of the needle against porcine skin was observed to be in excess of 90 N.

In Chapter 4, a hollow polymer microneedle array with tips and lumens that mimic conventional hypodermic needles, fabricated using UV lithography and a single-step micromolding technique, is presented. This 6×6 needle array consists of 1 mm tall high-aspect-ratio hollow microneedles with sharp beveled tips and 150 μm diameter side-opened lumens. A two-dimensional lithographic mask pattern and the topography of the micromold are utilized simultaneously to define the geometry of the beveled tip and the position of the lumen. Mechanical insertion and fluidic injection characterization of these hypodermic-needle-like (HNL) microneedles (MNs) is performed using excised porcine skin as a substrate. The required insertion force of an HNL MN is 0.275 N, which is comparable to that of a 26-gauge hypodermic needle, 0.284 N. These results are an order of magnitude reduction in insertion force over pyramidal-tip (PT) MNs of comparable tip diameter. This insertion force reduction confirms that the tip geometry is an important factor in utilization of MNs in these applications. No needle fracture was observed under an optical microscope following the pressing of an HNL MN against excised porcine skin with application force of 50 N. Preliminary manual injection of dye through an HNL MN from a syringe into excised porcine skin verifies the injection functionality of HNL MNs. For potential continuous drug delivery application, medical transfer skin adhesive is

patterned and applied onto the baseplate between MNs within an HNL MN array to increase the adhesion between the needle array and the skin.

A summary of this research, contributions of this dissertation, and suggestions for future work are presented in Chapter 5.

CHAPTER 2

BACKGROUND

2.1 Microneedles for Drug Delivery into Skin

The concept of using micron-sized needles to create pathways through the outmost layer of skin, SC, and to deliver drugs underneath the SC can be traced back to a patent granted in 1976. [5] Early demonstrations of MNs were published in the late 1990s. The delivery of biomolecules into the skin of live animals using SMNs was published in 1995. [6] In 1998, Henry et al. reported the successful insertion of SMNs into the epidermis of human cadaver skin and observed a four-order-of-magnitude increase in the permeability of cadaver skin to a model drug following the insertion of the MNs. [7] Since the year 2000, researchers have reported a variety of MNs for drug delivery into skin. Both SMNs and HMNs reported to date can be categorized according to their structural materials. Silicon, metals, and polymers are the three commonly-used structural materials for MNs and are discussed in Section 2.2 and Section 2.3.

2.2 Solid Microneedles

To fabricate needles with characteristic dimensions in the microns to hundreds of microns (MNs) for insertion into skin, the choice of the structural material is important. The mechanical strength of the structural material is required to be sufficiently high such that MNs can be inserted into the skin and do not break during insertion. In addition, it would be beneficial if the fabrication processes associated with the structural material were simple, well established, and cost effective.

Silicon has a high Young's modulus of 160 GPa (Pascal, Pa = N/m^2). [19] Moreover, silicon is commonly used in the microelectronics industry, and its associated microfabrication techniques are well established. In both of the early MN demonstrations discussed in Chapter 1, silicon was used as the structural material, and conventional silicon microfabrication techniques (e.g., photolithography and wet / dry etching) were involved. [6, 7] The silicon MNs reported by Henry et al. are 150 μm in height with a tip diameter of less than one μm. [7] Figure 2 shows scanning-electron-microscope (SEM) images of the silicon MNs reported by Henry and his colleagues. Other silicon microfabrication techniques have also been used by researchers to construct MNs. Shikida et al. reported the creation of pen-shaped SMNs by using a combination of saw dicing and anisotropic wet etching of silicon. [20] The fabricated pen-shaped MNs are 300 μm in height with a tip diameter of less than 0.1 μm.

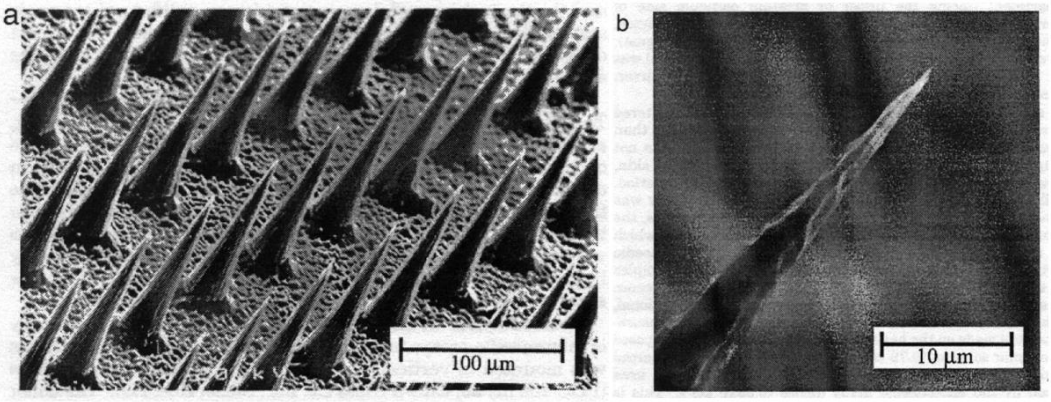

Figure 2. SEM images of the silicon MNs reported in [7]. (a) A section of a 20-by-20 array of the MNs. (b) Close-up view of the tip of an MN.

In addition to silicon, metals are another group of materials that possess high Young's moduli. For instance, the Young's moduli of titanium and stainless steel are 110 GPa and 190 GPa, respectively. [21] Cormier et al. reported titanium arrowhead-shaped

MNs that are 330 μm in height. The arrowhead portion of the MNs has a maximum width of 170 μm with a thickness of 35 μm and a tip sharpness of 10 μm. [22-24] The titanium MNs were fabricated by using photochemical etching into a titanium sheet with a pre-defined arrowhead pattern, followed by bending in-plane MNs 90 ° to form out-of-plane devices. The fabricated MNs with a desmopressin coating on the arrowhead portion are shown in Figure 3. In addition to titanium, stainless steel was also used as a structural material for metal MNs. Martanto et al. reported cutting a stainless-steel sheet in a reversed-V pattern with an infrared laser, followed by hot-water cleaning, bending of in-plane MNs by 90 °, and electropolishing to remove debris. [25] The fabricated stainless-steel MNs are 1000 μm in height with a base of 200 μm and a thickness of 50 μm.

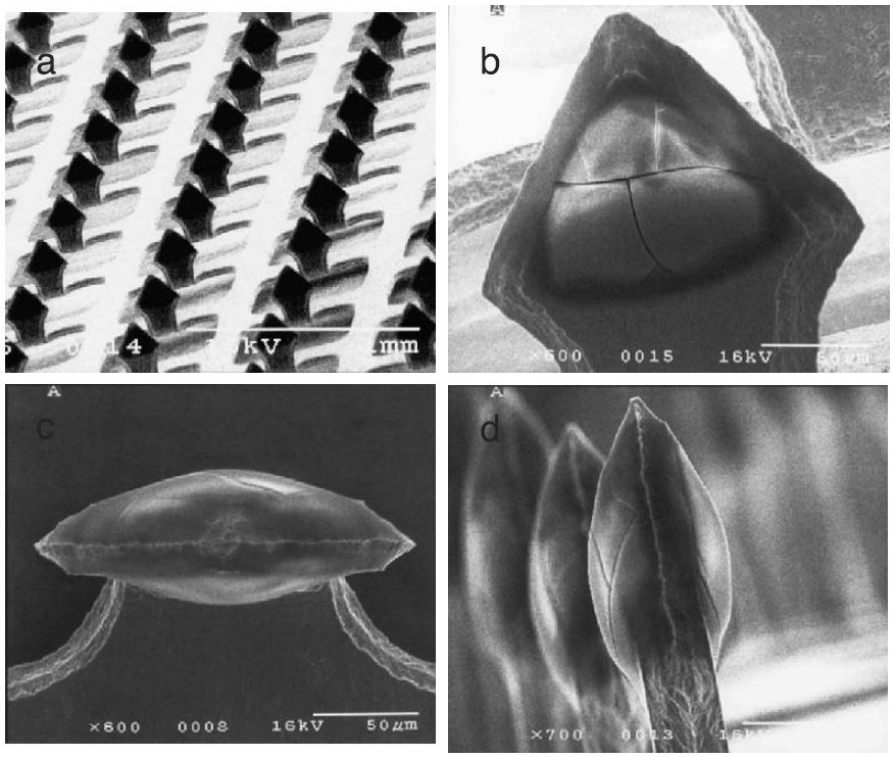

Figure 3. SEM images of the titanium MN array reported in [24]. The arrowhead portion of each MN is coated with desmopressin. (a) Front view of the MN array. (b) Close-up view of the arrowhead portion of an MN. (c) Top view of an MN. (d) Side view of a row of MNs. The scale bar is one mm in (a) and 50 μm in (b)-(d).

Polymers, because of their ability to be processed by cost-effective molding techniques and the fact that many of them are biocompatible or biodegradable, have been intensely studied as structural materials for MNs in recent years. [26] In 2005, Park et al. reported three different polymer MNs fabricated using a micromolding technique. [26] These three polymer MNs are different in their tip profiles but are all made of the same biocompatible polymer, polyglycolic acid (PGA). The master structures of the MNs are made of either a photosensitive polymer, which is SU-8, or polyurethane (PU) using photolithography and wet / dry etching techniques. Polydimethylsiloxane (PDMS) was then cast onto the master structures to replicate the shapes of the MNs, followed by the removal of these female PDMS molds from the master structures. The PGA MNs were subsequently fabricated by casting PGA into these female PDMS molds, followed by the removal of the PGA MNs from the molds. The fabricated PGA MNs are 600-1500 μm in height with a 100-200-μm base and a tip diameter of 10-20 μm. Figure 4 shows an SEM image of a row of the fabricated chisel-tip MNs. The Young's modulus of PGA is 6.5 GPa. [27] Successful insertion into human cadaver epidermis as well as the finger of a human subject was demonstrated with the PGA MNs. [26, 28]

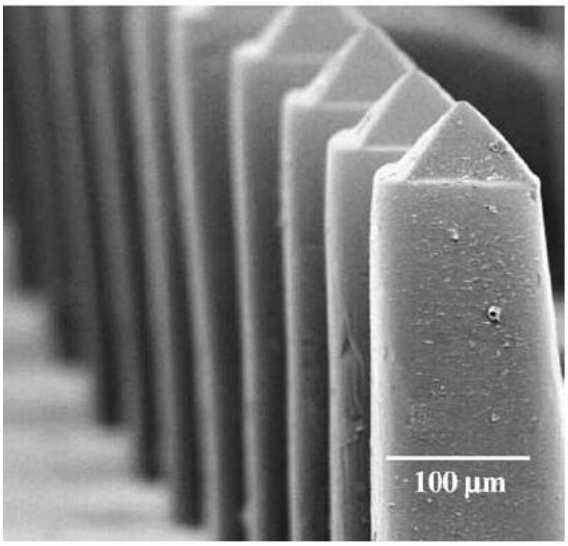

Figure 4. An SEM image of a row of the fabricated chisel-tip PGA MNs reported in [26]. Each MN is 570 µm in height with a 10-µm-wide tip.

To prevent biohazardous sharp tips of MNs from accidental or intentional reuse following administration, Prausnitz et al. reported the use of water-soluble polymers as the structural materials to construct MNs. [29, 30] After successful insertion into skin, the water-soluble MNs dissolve inside the skin when they are in contact with the interstitial fluid in the skin. Polyvinylpyrrolidone (PVP) and carboxymethylcellulose (CMC) were chosen as the structural materials for the dissolvable MNs because of their mechanical strength, high water solubility, and biocompatibility. The fabricated PVP and CMC MNs are 600-750 µm in height with a base diameter of 250-300 µm and a tip diameter of 5-10 µm. One fabricated PVP MN array is shown in Figure 5. The PVP and CMC MNs were shown to insert successfully into excised porcine skin. The upper half of each MN dissolved in the skin within one minute following the insertion, leaving no biohazardous sharp tips. [29-31]

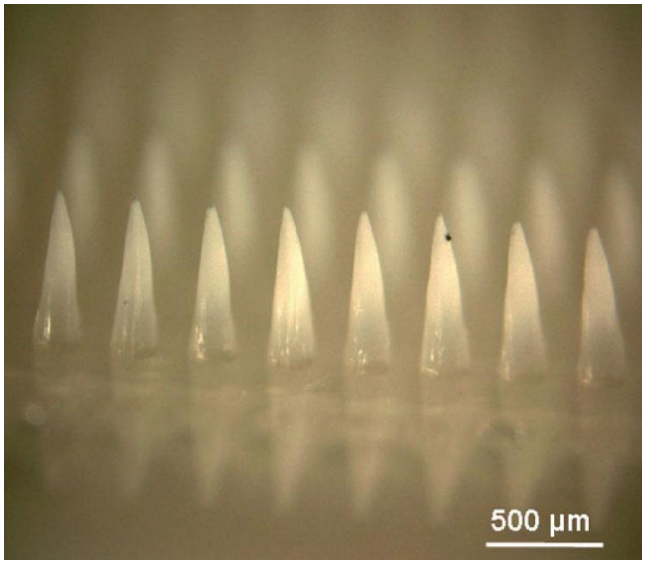

Figure 5. An optical micrograph of the side view of a PVP MN array. Each MN is 750 µm in height, 250 µm in base diameter, and 5 µm in tip radius. [29]

In terms of the commercialization of SMNs, several private companies around the globe either have their SMN products commercially available on the market or currently work on the clinical trial / commercialization of their products. These private companies include Dermaroller, Zosano Pharma, MITI Systems, and TheraJect. The products from Dermaroller are for cosmetic purposes and are commercially available. These products consist of a handle with a roller whose outer surface is covered by out-of-plane SMNs that are made of stainless steel and are 200-1500 µm in height. [33] Zosano Pharma has a lead product that is being prepared to enter Phase III clinical trials. This lead product consists of an array of titanium MNs, and the array is attached to an adhesive backing and a patch applicator. These titanium MNs are coated with parathyroid hormone (PTH) for patients with severe osteoporosis.

2.3 Hollow Microneedles

Compared to SMNs, HMNs have a lumen inside their structures, resulting in an increase in the complexity of the fabrication process. Several microfabrication techniques and approaches have been reported to successfully construct the lumen and are discussed in this section. Analogously to the classification of solid microneedles, HMNs reported to date can also be categorized by the materials comprising their mechanical structure. The three commonly-used structural materials for HMNs are silicon, metals, and polymers.

2.3.1 Silicon as the Structural Material

When silicon is used as the structural material for HMNs, the lumen is often constructed by using a deep-reactive-ion-etching (DRIE) technique, which is an anisotropic dry etching process for high-aspect-ratio (up to 30:1) profiles. To form the shape of HMNs, several fabrication approaches have been reported by different researchers. These approaches include anisotropic wet etching, isotropic dry etching, and saw dicing.

Anisotropic wet etching is typically used to create a slope from the top to the bottom of the MN on one side of the MN, resulting in a bevel tip. Gardeniers et al. reported bevel-tip silicon HMNs that are 350 μm in height with a base of 250 μm in width and a lumen of 70 μm in diameter (shown in Figure 6). [35] The lumen was fabricated by using a DRIE process on both sides of the silicon wafer. The side opening of the lumen is located on the slope that was created during the anisotropic wet etching. The drawback of this fabrication approach is that to construct taller MNs the base width of the MNs increases, because the angle of the slope is determined by the (111) crystal

plane of silicon. A wider base of the MN may lead to more tissue damage during insertion and may increase patient discomfort.

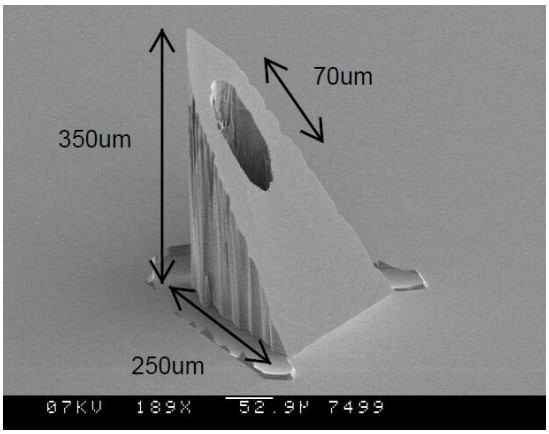

Figure 6. An SEM image of the fabricated silicon HMN reported by Gardeniers. [35]

Isotropic dry etching is another technique reported to form the shape of HMNs. Stoeber and Liepmann reported volcano-like HMNs that are 200 μm in height and have a lumen of 40 μm in diameter. The lumen opening can be located either at the center of the MN tip or on the side of the MN structure. [36, 37] The volcano shape of the MN was formed by using isotropic dry etching with SF_6 plasma on the front side of the silicon wafer. The lumen was constructed by using a DRIE process to etch the silicon wafer from the back side of the wafer. Using the isotropic etching to create the shape of the MN also results in the disadvantage that the base width of the MN increases with the height of the MN. Roxhed et al. reported a combination of isotropic and anisotropic etching to construct a tall MN structure without increasing the base width of the MN. [38] This combination of the processes consists of a continuous alternation between isotropic dry etching with the SF_6 plasma and anisotropic dry etching. The isotropic etching was

primarily used to construct the sharp tips, and the anisotropic etching was performed to form the tall MN structure. The lumen was constructed by using the DRIE process from the back side of the silicon wafer. The fabricated HMNs are 400 μm in height with a base of 100 μm in diameter and a tip of less than 0.1 μm in radius, as shown in Figure 7.

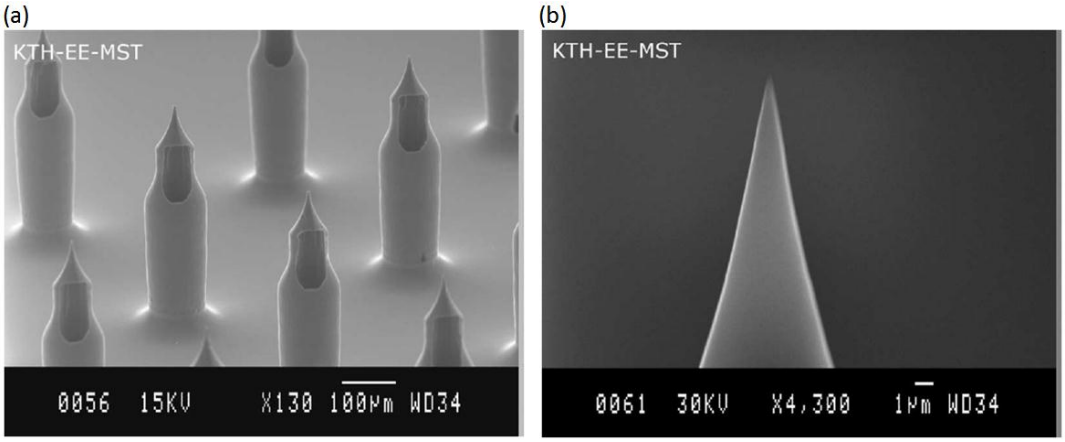

Figure 7. SEM images of the fabricated silicon HMN array reported in [38]. (a) Top view of the HMN array. (b) Close-up view of the tip of an HMN.

In addition to conventional wet and dry etching techniques, saw dicing that is usually used to cut individual silicon chips from a silicon wafer was adapted to create the shape of HMNs. Baron et al. reported construction of the shape and the bevel tip of silicon HMNs by using the saw dicing technique. [39] The lumen was constructed by using the DRIE process from the back side of the silicon wafer. The process started with a one-mm-thick silicon wafer, and the fabricated HMNs are 700 μm in height and 150-200 μm in base width. The diameter of the lumen is 40-60 μm.

2.3.2 Metal as the Structural Material

When metals are used as the structural materials for HMNs, nickel is commonly chosen because of its mechanical strength and feasibility of electroplating. [40] To construct a nickel HMN, an MN mold is first constructed by a variety of fabrication approaches, which are discussed in this subsection. Nickel is then electroplated on the constructed MN mold. Subsequently, the mold is etched completely with a chemical solution, resulting in the release of the nickel HMN.

Kim et al. reported the use of a photosensitive material, SU-8, to construct the MN mold. [41] The SU-8 MN mold was prepared by using two backside UV exposures, resulting in an SU-8 base block and tapered SU-8 cylinders on the base block. Nickel was then electroplated onto the constructed MN mold. Another layer of SU-8 was cast onto the sample and soft baked to planarize the sample surface, followed by a mechanical polish to remove the nickel that was deposited on the top surface of the SU-8 cylinders. This planarizing SU-8, which was not exposed to UV light, was then removed by the SU-8 developer. The SU-8 mold itself was removed by using dry etching with O_2/CF_4 plasma, releasing the final structure of the nickel HMNs. The fabricated nickel HMN has a tapered-cylinder profile. The lumen opening is located at the center of the MN tip. The height of the MN is 400 μm. The top and bottom inner diameters of the MN are approximately 35 μm and 75 μm, respectively. The thickness of the nickel wall of each HMN is 20 μm.

The SU-8 MN mold can also be fabricated by a drawing-lithography technique. Lee et al. reported using an array of stainless-steel drills to vertically draw SU-8 pillars from a layer of SU-8 that is spin-coated on a flat glass substrate. [42] The drawing

process was performed at 60 °C with a pulling rate of 10 μm/s for six minutes, followed by a curing process at room temperature for 30 minutes. A sudden pull at 700 μm/s was applied to separate the drills from the tapered SU-8 pillars, which later served as an MN mold. The top ends of the SU-8 pillars were then coated with enamel in a dipping process to prevent nickel from being deposited on the top ends during the subsequent electroplating process. Following the completion of the nickel electroplating process, the SU-8 pillars were removed by the SU-8 developer, resulting in the release of the nickel HMNs. The fabricated nickel HMNs are 2000 μm in height with a base diameter of 300 μm, as shown in Figure 8. The lumen opening is located at the center of the MN tip, and the diameter of the lumen is 20 μm. The wall thickness of the nickel HMN ranges from 10 μm to 30 μm, depending on the parameters used in the electroplating process. To create a beveled tip with a side-opened lumen, a laser cutting step was implemented following the nickel electroplating process [43]. The needle tip was exposed to the laser beam at an angle of 15 ° between the needle shaft and the laser beam. The SU-8 development step was performed following the laser cutting step to release the final nickel HMN structure.

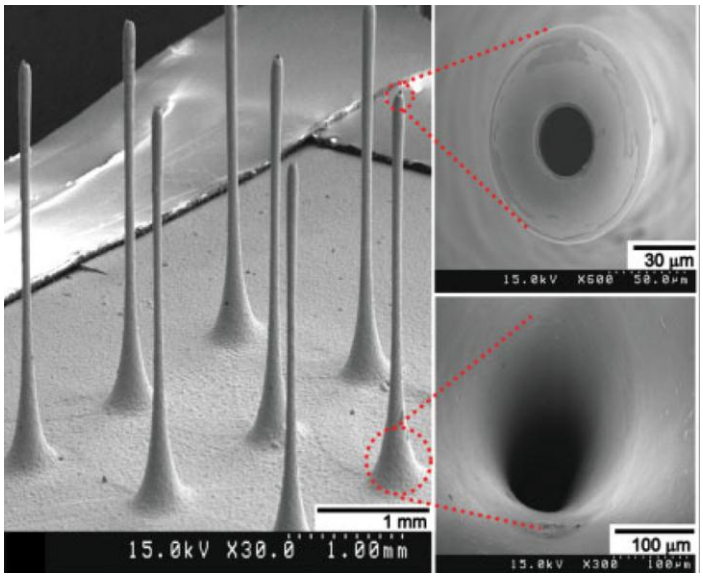

Figure 8. SEM images of the nickel HMNs reported by Lee et al. in [42]. These nickel HMNs measured 2000 µm in height and 300 µm in base diameter with a lumen diameter of 20 µm at the top of a needle tip.

In addition to these two protruding SU-8 MN molds, Davis et al. reported a recessed polymer mold for the construction of nickel HMNs. [40] To create the recessed polymer mold, an excimer laser was used to drill a tapered through hole into a 500-µm-thick sheet of polyethylene terephthalate (PET), which was chosen as the mold material for its ease of removal and its relatively inexpensive cost. The tapered hole is wider on the top surface of the PET sheet and narrower on the bottom surface. Subsequently, nickel was electroplated onto the constructed PET MN mold. The PET mold was removed in a concentrated sodium hydroxide (NaOH) solution, leading to the release of the final tapered nickel HMN structure with the lumen opening at the center of the tip. The fabricated HMN is 500 µm in height with a 300-µm-wide base tapering to a tip of 75 µm in diameter, as shown in Figure 9. The nickel wall thickness is 10 µm.

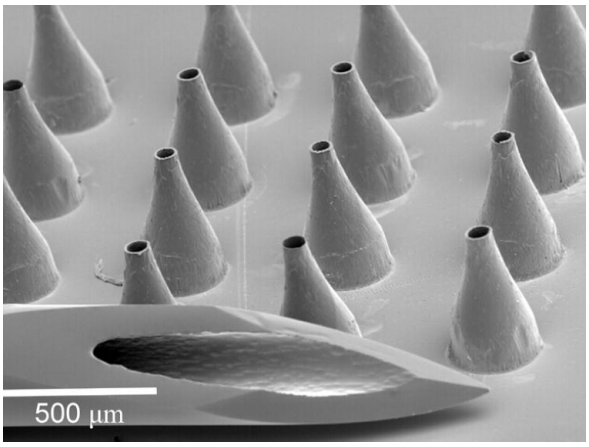

Figure 9. An SEM image of the nickel HMN array presented in [40] and a 27-gauge HN for comparison.

Furthermore, Laurent et al. with Becton Dickinson (BD) reported mounting a single 30-gauge HN of 1.5 mm in height to the tip of a glass syringe for intradermal vaccine delivery. [44]

2.3.3 Polymer as the Structural Material

Polymers have been more frequently reported as the structural materials for HMNs in recent years, because researchers started to take advantage of photosensitive polymers and micromolding techniques. Photosensitive polymers, micromolding techniques, or a combination of both have been reported to construct polymer HMNs.

Several photosensitive polymers have been reported to construct polymer HMNs. Luttge et al. reported 430-μm-tall and 250-μm-wide cylindrical SU-8 HMNs with a bevel tip, as shown in Figure 10. The lumen opening is on the bevel slope, and the diameter of the lumen is 75 μm. [45] To fabricate these SU-8 HMNs, a silicon mold was first constructed by using anisotropic wet etching to form V-groove trenches on the surface of a silicon wafer. The V-groove trench served as a mold to define the bevel slope of the

SU-8 HMNs. The first layer of SU-8 was spin-coated onto the silicon mold and patterned photolithographically with a photo mask to define the tip and the shaft of the HMNs. The second layer of SU-8 was subsequently spin-coated and patterned with another photo mask to define a base plate for the HMNs. The entire sample was then immersed in SU-8 developer to remove the unexposed SU-8, leading to the release of the final SU-8 HMNs with a base plate. Using the anisotropic wet etching of silicon to define the bevel tip of HMNs results in limited options for the bevel angle because of the crystal orientation of silicon. More recent work using UV lithography of SU-8 in silicon molds has proposed [46] and demonstrated [47] extension of the previous silicon mold work to heights of approximately 1000 μm.

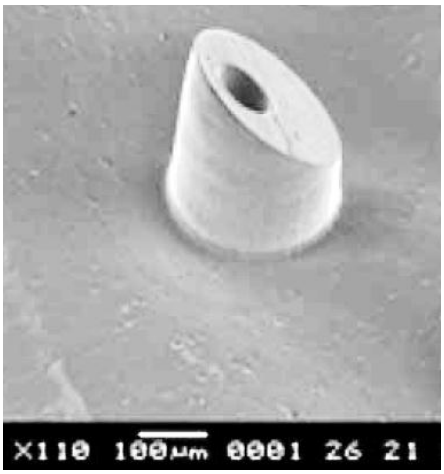

Figure 10. An SEM image of the bird's-eye view of an SU-8 HMN presented by Luttge et al. in [45]. The SU-8 HMN measured 430 μm in height and 250 μm in width with a bevel tip.

Fabrication of 980 μm tall HNL MNs with a functional baseplate based on UV lithography of SU-8 into elastomeric polymer molds was presented in [48]. The use of elastomeric molds not only allowed for ease of separation of the optically-defined MNs

from the molding substrate, but also allowed the bevel angle of the MN tips to be modified, since the elastomeric mold used was constructed using an inclined UV lithography process with an adjustable incline angle. The fabrication approach of UV lithography of SU-8 into elastomeric polymer molds is discussed in more detail in Chapter 3 and Chapter 4.

HMNs with a water-soluble tip, a photo-defined SU-8 shaft and baseplate were demonstrated by Paik et al. [49] The water-soluble tip is expected to dissolve and be absorbed into surrounding tissue following the needle insertion, and therefore no sharp tip is present after use of the needles. The conical water-soluble tips were fabricated by casting a mixture of polyvinyl alcohol (PVA), PVP, and water with a weight ratio of 3:2:4 onto the conical trenches of a pre-constructed PDMS mold, followed by the removal of excessive mixture from the surface of the PDMS mold with a PDMS block. The SU-8 shaft and baseplate were obtained using UV lithography with a gray-tone photomask. The water-soluble tips were subsequently contact-transferred onto the top of the needle shafts. The final needle structure measured 710 μm in height, consisting of a 240-μm-tall tip and a 470-μm-tall shaft. An optical micrograph of the SU-8 HMNs with a water-soluble tip is shown in Figure 11. In addition to the molding technique, dissolvable tips can be fabricated using a drawing-lithography technique. Xiang et al. demonstrated 1000 μm tall conical maltose tips on top of 350 μm tall SU-8 shafts using the drawing lithography technique where SU-8 shafts were used to vertically draw conical maltose tips from a layer of maltose on a glass substrate. [50]

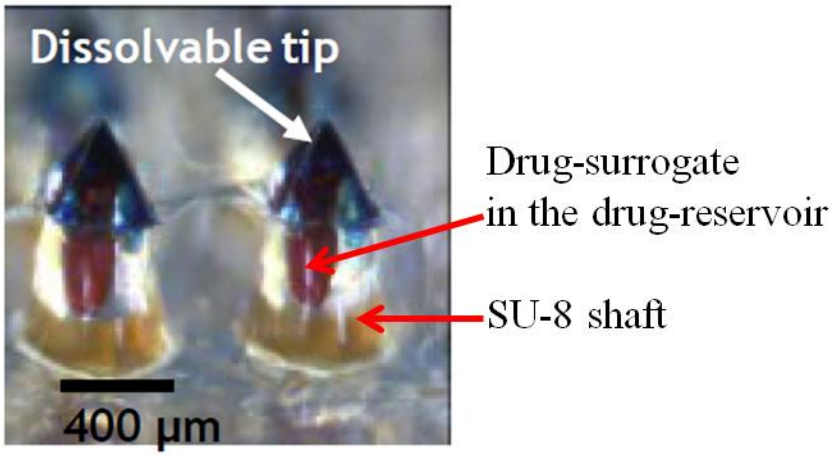

Figure 11. An optical micrograph of the SU-8 HMNs with a dissolvable tip reported in [49]. The dissolvable tip was dyed blue for visibility. A drug-surrogate was filled into the drug reservoir inside the SU-8 shaft.

Choi et al. reported the construction of SU-8 HMNs by using photolithography, reactive ion etching (RIE), and laser drilling. [51] The first step of the fabrication process was to spin coat the first SU-8 layer on the chromium-patterned side of a glass substrate, followed by the front-side i-line (365nm) UV exposure with a photo mask to define an SU-8 baseplate for the subsequent SU-8 HMNs. The second SU-8 layer was then cast onto the first layer of SU-8 and was exposed to UV light through the back side of the glass substrate to pattern SU-8 cylinders through the SU-8 baseplate. The patterned chromium on the glass substrate served as a photo mask during the second UV exposure. The sample was immersed in the SU-8 developer to release the SU-8 cylinders and SU-8 baseplate. The SU-8 cylinders were sharpened using RIE with O_2 and CHF_3 gases to form the SU-8 MNs. An excimer laser was then used to drill through holes from the back side of the SU-8 baseplate to the top end of the SU-8 MN to create a side-opened lumen. The fabricated SU-8 HMNs, shown in Figure 12, are 410 μm in height with a 100-μm-wide base and a lumen of 20 μm in diameter.

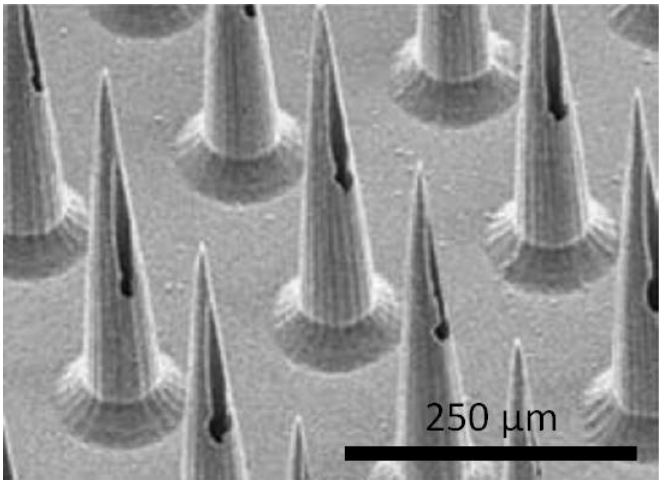

Figure 12. An SEM image of a section of the SU-8 HMN array reported by Choi et al. in [51].

In addition to SU-8, polymethyl methacrylate (PMMA) was also used to construct HMNs by using a deep X-ray lithography (DXRL) and micromolding technique. To perform the DXRL, a synchrotron radiation source is required to provide X-rays with a wavelength of 0.1 nm. [52] Perennes et al. reported 400-µm-tall PMMA HMNs, which have a triangular base of 350 µm in width and a bevel tip. The opening of the lumen is located on the bevel slope, and the diameter of the lumen is 84 µm. [53] Two DXRL steps were first performed with two separate masks to construct the PMMA HMNs on a conductive substrate. The PMMA HMNs on the conductive substrate subsequently served as an MN mold to construct a female intermediate PVA mold. Another PMMA layer was cast onto the intermediate PVA mold. The PMMA / PVA assembly was then immersed in water to dissolve the PVA mold, releasing the final PMMA HMNs with a baseplate. The fabricated PMMA HMNs with a base plate are shown in Figure 13.

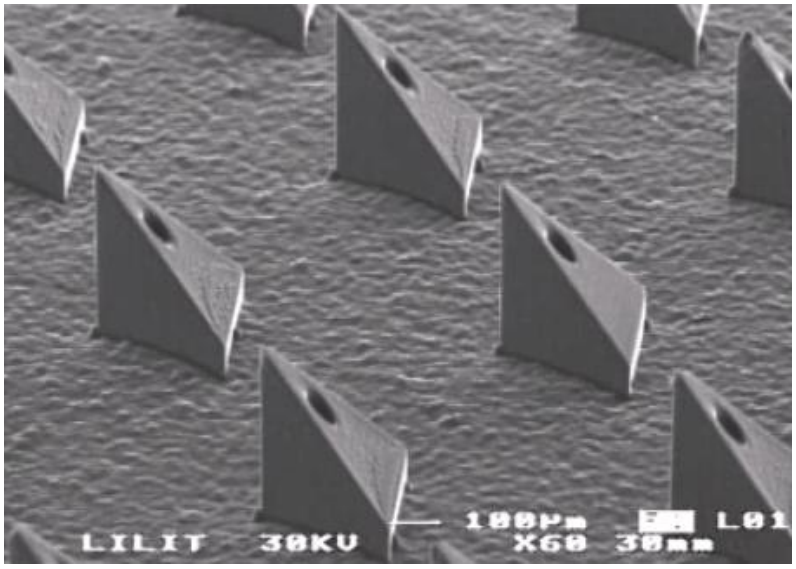

Figure 13. An SEM image of a section of the PMMA HMNs reported by Perennes et al. in [53].

Two-photon polymerization (2PP), was reported to construct HMNs out of a photosensitive polymer. [54] Compared to traditional photolithography processes, the 2PP technique polymerizes a very small focal volume of a photosensitive polymer with femtosecond laser pulses. The smallest lateral dimension of the focal volume demonstrated to date is 0.1 μm. [54, 55] To expose the volume of a particular shape that is larger than the focal volume, the polymer sample is moved in a three-dimensional fashion (XYZ) by a micropositioning system. The unexposed portion of the polymer is subsequently removed by a developer solution to release the final HMN structure. Ovsianikov et al. reported 800-μm-tall conical HMNs with a base of 150 μm in diameter and side-opened lumens, as shown in Figure 14. [54] The photosensitive polymer used by Ovsianikov et al. was an organically modified ceramic (Ormocer®) hybrid material, and the material was exposed by 780 nm femtosecond laser photons from a titanium:sapphire

laser. This fabrication approach is a serial process, and the fabrication time for a single HMN is approximately two minutes.

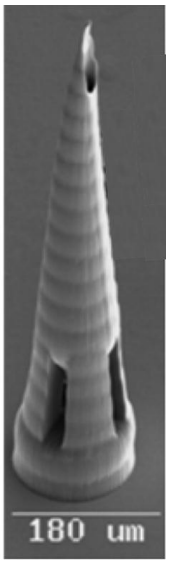

Figure 14. An SEM image of the fabricated Ormocer® HMN by using two-photon polymerization. [54]

Mansoor et al. reported 250 μm tall volcano-like HMNs formed on a mold during a solvent evaporation process. [56] Conical SU-8 pillars were defined using backside UV exposure of SU-8 through a photomask and a glass substrate, followed by coating of Parylene C and PDMS. The PDMS surface of the constructed pillar mold was treated using oxygen plasma to improve the surface wetting of the PDMS for the subsequent deposition of a composite mixture of nanoclay powder, a polyimide solution, and a polyimide solvent. The polyimide solvent, i.e. N-methyl-2-pyrrolidone (NMP), evaporated in the baking process of the composite mixture, resulting in volcano-like HMNs whose lumens were defined by the pillars. The HMNs were mechanically released from the pillar mold, followed by polishing of the HMN tips with a fine aluminum oxide

polishing film to open the lumens at the HMN tips. The final volcano-like HMNs is 250 μm tall with a tip diameter of 50 μm with a top-opened lumen, as shown in Figure 15.

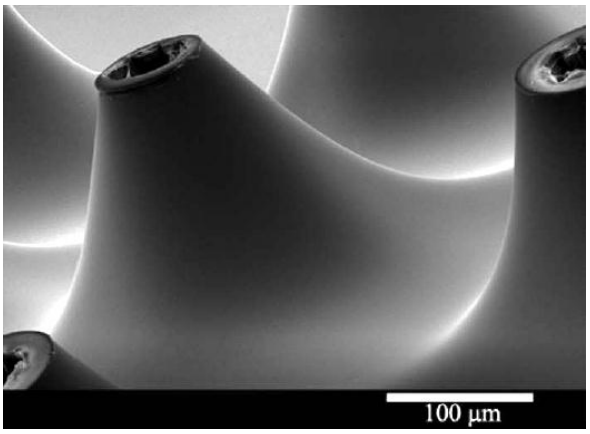

Figure 15. An SEM image of the volcano-like HMNs formed on a pre-constructed pillar mold during a solvent evaporation process. The structural material of the HMNs is a polyimide/nanoclay composite. [56]

Injection molding is another fabrication technique reported to create HMNs. Hansen et al. reported 900-μm-tall and 400-μm-wide cylindrical HMNs with a bevel tip, as shown in Figure 16. The lumen opening is located on the bevel slope and is elliptical, with major and minor radii of approximately 100 μm and 50 μm, respectively. [57] The HMN was constructed by using the injection molding of polycarbonate, followed by laser drilling to create the lumen. [58, 59] The injection molding is a batch process; nevertheless, the laser drilling for each lumen is a serial process. HMNs fabricated using a fully injection molding approach with polyoxymethylene (POM) as a structural material were demonstrated by Yung et al. [60] The HMNs measured 500 μm in height and 200 μm in bottom width with a beveled tip and a side-opened lumen of 60 μm in diameter, as shown in Figure 17.

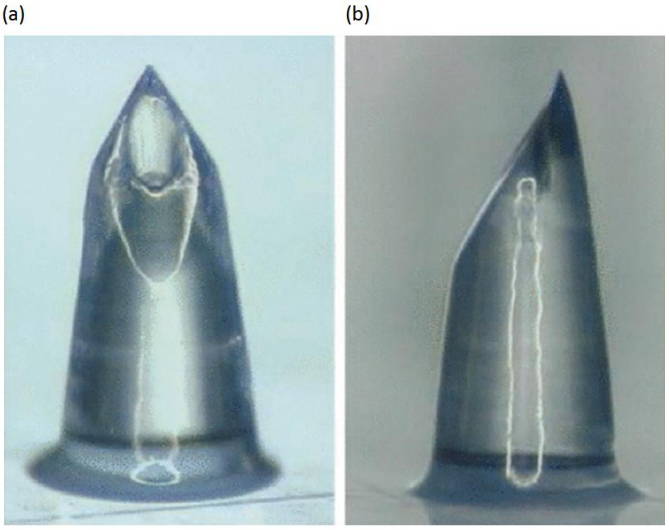

Figure 16. Optical micrographs of the fabricated polymer HMN presented in [57]. Each HMN is 900 µm in height. (a) Front view of the HMN. (b) Side view of the HMN.

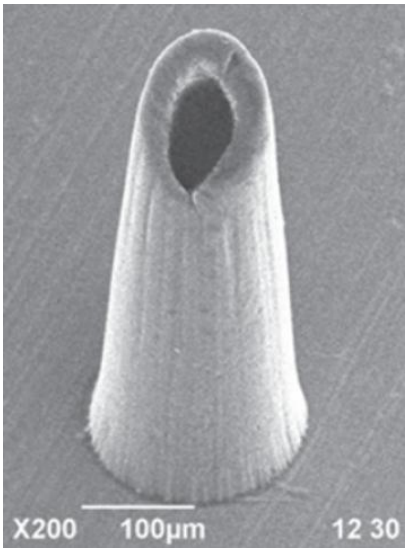

Figure 17. An SEM image of an HMN fabricated using a fully injection molding approach reported in [60]. The height of the fabricated HMNs is 500 µm.

2.3.4 Glass as the Structural Material

Glass micropipettes are commonly used as microelectrodes to record bioelectric signals of cells in the field of cellular physiology. [61, 62] Martanto et al. reported glass micropipettes with desired dimensions by using a conventional glass micropipette puller and a microelectrode beveler and subsequently used the fabricated micropipettes as HMNs for fluid delivery to skin. [63] The fabrication process of a single glass micropipette started with borosilicate glass tubing of 1.5 mm in outer diameter. A transverse zone of the glass tubing was heated by a surrounding filament, while both ends of the tubing were pulled away from each other longitudinally to increase the length of the tubing and to simultaneously reduce the diameter of the heated portion of the tubing to a desired dimension. The elongated and shrunk portion of the glass tubing was subsequently cut and rubbed against a fine abrasive surface at a particular angle to create the bevel tip for the final glass micropipette. The fabricated glass micropipette, as shown in Figure 18, has a bevel tip and a side-opened lumen of 60 μm in diameter. The maximum height of the glass micropipette is 1100 μm and can be reduced by retracting the micropipette into a custom micropipette holding device. Glass micropipettes with various geometries and dimensions similar to micromachined HMNs can be quickly fabricated by using this pulling-and-beveling technique; nevertheless, only one single micropipette can be created at a time since this technique is a serial process.

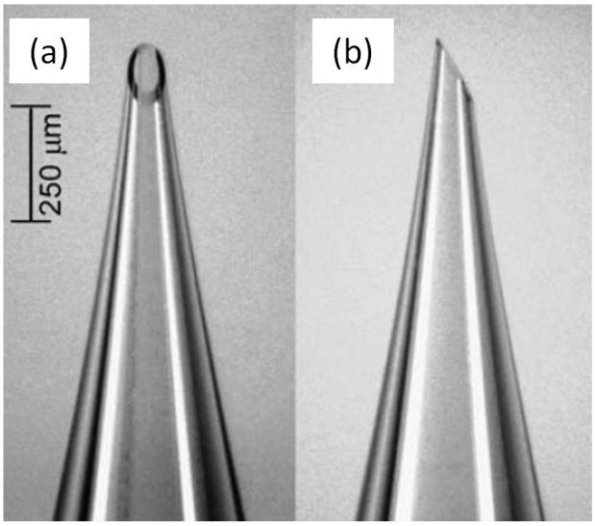

Figure 18. Optical micrographs of the fabricated glass micropipette reported in [63]. (a) Front view of the micropipette. (b) Side view of the micropipette.

2.4 Packaging of Microneedles

For clinical use, HNs should be packaged as a complete device. For instance, a single HN is attached to a syringe through a Luer-lock connector, and the sharp tip is protected by a needle shield. In addition, the HN and the syringe are packed together in a sealed bag as a complete device. The same packaging requirements also apply to MNs for clinical use. Nevertheless, only few MN packages were reported in the literature.

The packaging requirements are different for SMNs and HMNs. The SMN package is required to provide a protection for MN tips prior to insertion as well as to supply the driving force to perform the insertion of MNs into skin. Figure 19 shows two representative SMN packages reported in the literature. [3] Figure 19(a) shows a MicroCor^{TM} applicator from Corium International. This applicator is for single use. A MN patch is located under the top surface of the applicator, and the MN tips face downward in the figure. The MN patch is applied to the skin by pressing the top surface of the applicator with a finger. The finger then keeps pressing the patch against the skin

for several minutes to deliver the coated drug, followed by the removal of the applicator from the skin. Figure 19(b) shows the Macroflux® drug delivery system from Zosano Pharma. An applicator and an MN patch are shown in Figure 19(b)-i. The applicator with the MN patch attached underneath is pressed against the skin to apply the MN patch (Figure 19(b)-ii). The adhesive on the MN patch keeps the patch on the skin surface when the applicator is removed.

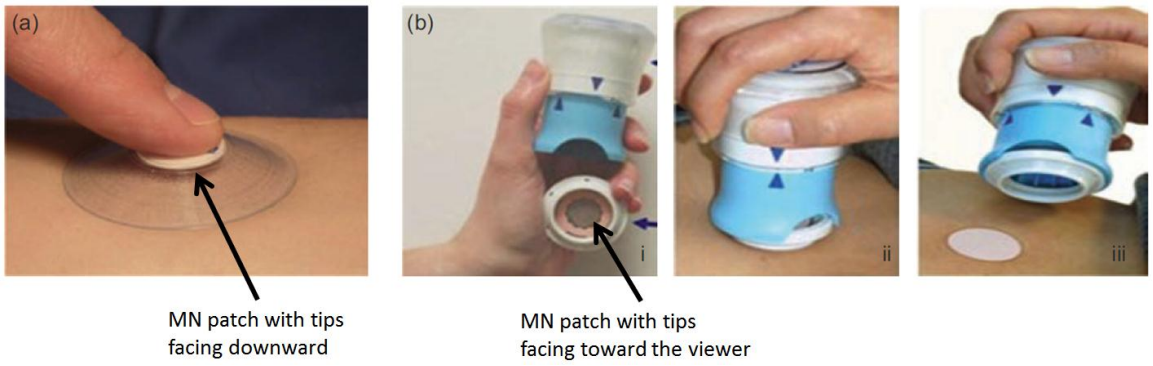

Figure 19. Two representative SMN packages. (a) MicroCor™ applicator from Corium International. (b) Macroflux® drug delivery system from Zosano Pharma. (i) An applicator and an MN patch. (ii) Press the applicator to apply the MN patch on the skin. (iii) The MN patch adheres to the skin while the applicator is removed from the skin. [3]

In addition to the protection and insertion force required for their SMN counterparts, HMN packages may require an integrated reservoir to store the drug and to provide another driving force to inject the drug from the reservoir to the skin. Figure 20, Figure 21, and Figure 22 present a brief summary of packaged HMN devices reported in the literature. Figure 20 shows a hollow microstructured transdermal system (hMTS) from 3M. [57, 64] The hMTS is a complete and packaged device, including an MN patch, adhesive for wearing the device on the upper arm or upper thigh, an actuator, an

application spring to provide the insertion force, a glass injection cartridge to store the drug, and a delivery spring to supply the injection force. A Soluvia™ prefillable microinjection system from BD is shown in Figure 21. [3, 44] The single needle shown in Figure 21(a) is a conventional 30-gauge HN, which protrudes 1.5 mm from the base as discussed in Subsection 2.3.2. The needle is protected by a needle shield and is attached to a custom glass syringe. This microinjection system was approved to be used with the first intradermal influenza vaccine in the European Union in 2009. [65] Figure 22 shows a MicronJet MN patch from NanoPass Technologies. [17, 66] The MN patch is mounted on the top surface of a custom Luer-lock connector, which can be attached to a standard syringe. A needle shield is provided with the MN patch.

The packaging of MNs plays an important role for MNs to be used in clinical application. The MicroCor™ applicator for SMNs is the simplest and smallest design among all presented packages in this section and can serve as a design platform for HMN packages. More design features have to be integrated into this design platform for HMN applications. Other packages discussed in this section have a larger applicator than the MicroCor™ one and / or involve the use of a syringe, resulting in a significant increase in device dimension. Therefore, a compact and fully-integrated HMN package design is desired for clinical use.

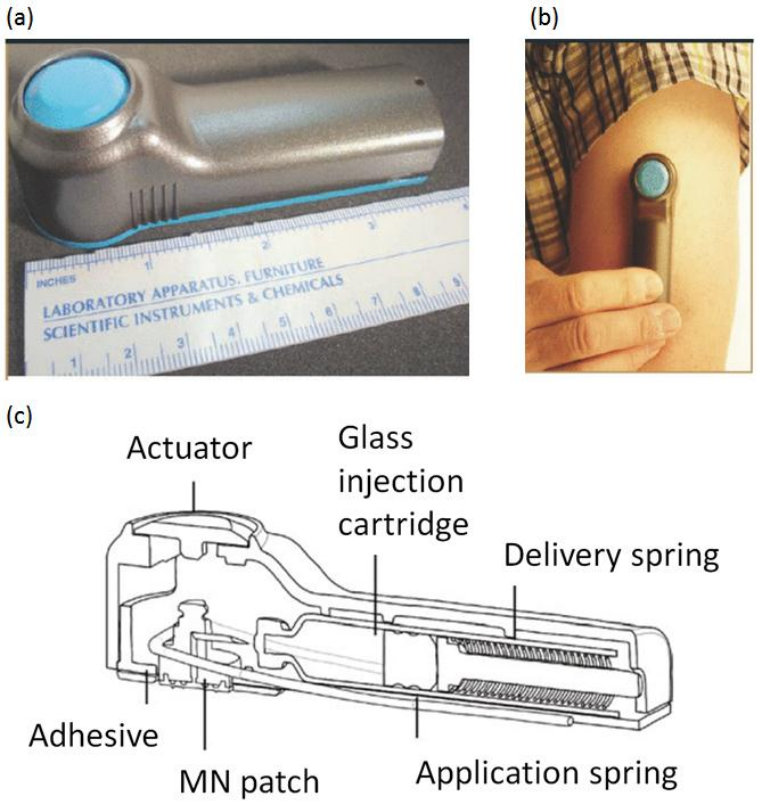

Figure 20. A hollow microstructured transdermal system (hMTS) from 3M. (a) A photograph of the hMTS. (b) A photograph showing the application of the hMTS on the skin. (c) A schematic depict of the cross section of the hMTS. [57, 64]

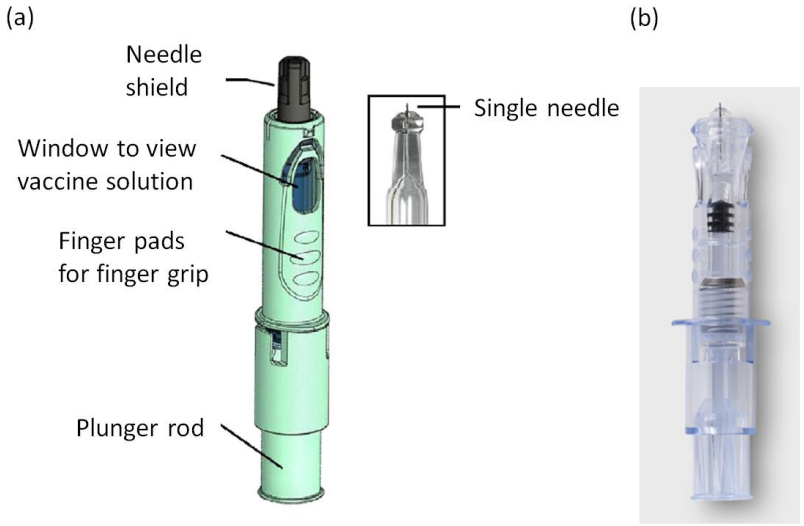

Figure 21. Soluvia™ prefillable microinjection system from BD. (a) A schematic depict of the Soluvia™ system. (b) A photograph of the Soluvia™ system. [3, 44]

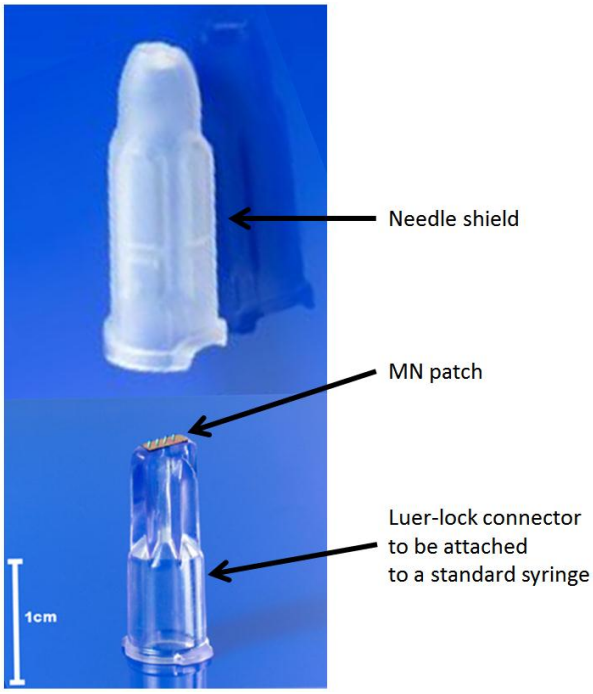

Figure 22. A photograph of the MicronJet MN patch from NanoPass Technologies. [17, 66]

2.5 SU-8, A Photosensitive Polymer

2.5.1 Introduction to SU-8

SU-8, a photosensitive polymer, is commonly used to create three-dimensional (3D) and high-aspect-ratio microstructures, e.g. MNs and micromolds. SU-8 consists of three components: epoxy resin, e.g., EPON SU-8 resin, solvent, and a photo-acid generator (PAG). [67] To create microstructures, a softbake step is performed to remove the solvent in the SU-8 following the spin coating or casting of SU-8 on a substrate. [68] Upon UV exposure, the PAG decomposes to form a strong acid, e.g., hexafluoroantimonic (HFA) acid. In the subsequent post-exposure bake (PEB) step, with

the HFA acid acting as a catalyst and the application of heat, the polymerization of the epoxy resin occurs. In the unexposed regions, the PAG does not decompose, and therefore without the HFA acid acting as a catalyst the polymerization of the epoxy resin does not occur, resulting in the unexposed SU-8 being removed by an SU-8 developer in the development step. To ensure the properties of SU-8 do not change in actual use, a hardbake step at 150-250 ℃ for 5-30 minutes can be added following the development step. [69] The UV exposure is typically performed using a mercury lamp for wavelengths of 365 nm (i-line) or 405 nm (h-line), since the optical absorption of SU-8 increases significantly for wavelengths below 350 nm. [67, 70] SU-8 microstructures with a height of 1.5 mm and an aspect ratio of 15 have been demonstrated. [71] The Young's modulus of SU-8 ranges from 4.0 GPa to 5.0 GPa, depending on the level of SU-8 cross-linking. [72]

2.5.2 Biocompatibility of SU-8

In this dissertation, SU-8 is used as the structural material for HMNs. For SU-8 to be used as a structural material of HMNs, the biocompatibility of SU-8 needs to be understood. ISO 10993 physicochemical and biocompatibility tests have been adopted by the Food and Drug Administration (FDA). [73, 74] Because of the complex nature of biocompatibility, it cannot be concluded yet that SU-8 meets all specifications necessary to meet the full ISO 10993 requirements for implants. [75] Nevertheless, a number of studies suggest that processed SU-8 is potentially a biocompatible material.

Kotzar evaluated the biocompatibility of SU-8 using a baseline battery of ISO 10993 tests. [73] The SU-8 measuring 55 μm in thickness was exposed to UV radiation with a dosage of 200 mJ/cm^2 with no hardbake. A cytotoxicity test (ISO 10993-5: Test

for Cytotoxicity - In Vitro Methods) using mouse fibroblast cells for 48 hours indicated a reactivity grade of 0.0, which was the same with the negative control and was less than Grade 2 (mild reactivity). An implantation test (ISO 10993-6: Test for Local Effect after Implantation) in the muscle tissue of rabbits showed differential irritant ranking scores of 1.0 and 2.3 from the negative controls after 1 and 12 weeks, respectively, indicating both results as non-irritant (smaller than a score of 3.0).

Nemani reported that an MTT (3-(4,5-dimethylthiazol-2-yl)-2,5-diphenyltetrazolium bromide) cell viability assay showed no cytotoxic effect from SU-8 leachates after 72 hours using rat glioma cells, and the hemolytic activity of SU-8 was comparable to those of three FDA approved implant materials, i.e., silicone elastomer, Buna-S synthetic rubber, and medical steel, after 24 hours. [76] In vivo histocompatibility study in mice for eight weeks showed a muted immune response to the subcutaneous SU-8 implants. The 200 μm thick SU-8 substrate was constructed using UV lithography with a UV dosage of 400 mJ/cm^2 and was hardbaked at 150 ℃ for 15 minutes. Similarly, Voskerician reported the in vivo inflammatory responses elicited by subcutaneous SU-8 implants in rats were not significantly different from the negative controls over up to 21 days. [77] Inflammatory responses were characterized using the total leukocyte concentration.

In addition to SU-8 material, an SU-8 based biomedical device was characterized for its biocompatibility by Cho. [78] SU-8 based neural microprobes measuring approximately 120 μm in width, 50 μm in height, and 500 μm in length with two embedded gold electrodes that were 12 μm in width and 8 μm in height were constructed using SU-8 microfabrication. The UV exposure dosage was 2750 mJ/cm^2 in total, and the

hardbake step was performed at 95 ℃ for eight hours. Fifty SU-8 microprobes were surgically implanted into transected rat sciatic nerves in 13 rats. Neural spike signals were successfully recorded using these implanted microprobes for four weeks. Postmortem examination of the nerve tissue surrounding the microprobes showed no evidence of infection or obvious tissue inflammation.

Various treatments of SU-8 have been demonstrated to further enhance the intrinsic biocompatibility performance of SU-8. Vernekar investigated several treatments to enhance the neuronal cytocompatibility of SU-8. [79] Layers of SU-8 100 μm and 300 μm in thickness were exposed to UV light with a dosage of 1000 mJ/cm^2 and 2000 mJ/cm^2, respectively, and no hardbake step was performed. The viability of rat neuronal cells in the cell culture after 7 or 21 days was used to assess the efficacy of various SU-8 treatments. Heat treatment of SU-8 at 150 ℃ under vacuum for three days increased the cell viability by more than 35 %. Subsequent ultrasonication in isopropanol for 15 minutes further increased the cell viability by 6.6 %. Heat treated and subsequently sonicated SU-8 samples were then either coated with 25 μm thick parylene C or treated with oxygen plasma for 150 seconds. The parylene C coating increased the cell viability by 17.6 % with a resultant cell viability that was 86.4 % and statistically indistinguishable from the control. The oxygen plasma treatment increased the cell viability by 10.4 %. Moreover, Tao reported that the covalent attachment of poly(ethylene glycol) (PEG) to the SU-8 surface can significantly lower the protein absorption and cell attachment on the SU-8 surface and therefore reduce biofouling. [80]

2.5.3 Alternative Materials to SU-8

Several materials, in addition to SU-8, may be considered as a potential candidate for the structural material of MNs in a UV lithography-based fabrication approach. For MN applications, biocompatibility and mechanical properties are of great importance in addition to the photodefinable nature of the material.

Restorative resins are commonly used for tooth cavity restoration. Resins consisting of diacrylate monomers and a photoinitiator can be polymerized using violet / blue light with wavelengths in the range of 400 nm to 500 nm. [81]

Foturan® from Schott Glass Corp. is a UV-sensitive glass with a Young's modulus of 78 GPa. [82] Microtubes with a side-terminated through hole were demonstrated using Foturan® as a structural material. [83] Nevertheless, the material cost and process complexity of Foturan® and other photosensitive glasses need to be taken into consideration for potential applications. [84]

PEG is a FDA-approved polymer. [85] With the addition of a photoinitiator, photodefinable PEG can be obtained. Kochhar reported successful patterning of PEG diacrylate (PEGDA) using UV lithography and 2-hydroxy-2-methyl-propiophenone (HMP) as a photoinitiator to construct 1200 μm tall conical SMNs. [86] Furthermore, insertion of PEGDA SMNs into porcine skin was demonstrated with no needle deformation following the insertion.

Polyimide has a Young's modulus of 8.8 GPa, and its biocompatibility, low cytotoxicity, and low hemolytic capacity have been shown in various studies. [75] Polyimides are available as photodefinable and non-photodefinable versions. Durimide®, a photodefinable polyimide from Fijifilm Electronic Materials Co., has been used to

construct a peripheral nerve interface device, and its biocompatibility has been suggested in in vitro and in vivo studies. [87]

PDMS is a widely used polymer in biomedical applications and has key characteristics of physiological indifference, excellent resistance to biodegradation and aging, and high biocompatibility. [75] Direct patterning of PDMS has been demonstrated with the addition of a UV-sensitive photoinitiator, benzophenone, and the photopatterned PDMS was suggested to be biocompatible following an additional extraction process to remove any unreacted photoinitiators. [88]

2.6 Manufacturing of Hollow Microneedles for Single-Use Devices

2.6.1 Desired Process Features for Manufacturing of Hollow Microneedles

To make the manufacturing of HMNs appropriate for single-use devices, several process features are required for HMN manufacturing. Batch processing allows for high throughput and is scalable for high-volume production. Conventional photolithography is inherently batch processing in nature and therefore is desirable for HMN manufacturing. Moreover, the fabrication method of interest needs to be capable of creating 3D structures for the construction of out-of-plane HMNs. In addition to creating 3D structures, definition of a high-aspect-ratio lumen that forms a microfluidic channel between the tip of the HMN and the back of the baseplate is of great importance in the design of the fabrication approach for HMN manufacturing. Furthermore, the cost of manufacturing needs to be taken into consideration. The manufacturing cost can be reduced with the use of potentially low-cost materials, e.g., polymers, for the structural material of the HMNs and the baseplate as well as by refraining from costly processing and facilities.

It is desired that the height of the HMNs be approximate 1.0 mm and HMNs are configured in an array for the following reasons. Because of skin deflection during insertion, it is suggested that only a top portion of MNs inserts into skin and is in contact with the underneath skin tissue. [63, 89] Martanto reported the insertion result of a single HMN with a height of 1080 μm using human cadaver skin as a substrate, and a cross-sectional image of the insertion site indicated a hole of 300-350 μm in depth was created following the insertion. [63] Chu reported insertion of 5 × 5 arrays of 900, 1200, and 1500 μm tall SMNs into excised porcine skin created holes of 300, 600, and 900 μm in depth, respectively. [89] Both insertion results suggested that the lower 600-800 μm portion of needle structures may not insert into skin and therefore may not be in contact with the underneath skin tissue. Furthermore, Sandby-Moller examined the epidermis thickness in more than 70 human subjects and reported average thicknesses of epidermis up to 100 μm, varying between individuals, body sites, and genders. [90] Therefore, to target the dendritic cell-rich dermis layer, MNs of 700-900 μm in height or taller may be required. Nevertheless, the pain perceived by human subjects during insertion of MNs increases with the height of the MNs as reported by Gill et al. using visual analog scale pain scores and stainless steel SMNs measuring 480-1450 μm in height. [91] Consequently, HMNs of approximate 1.0 mm in height are desired.

To deliver aqueous substances into skin, an array of multiple HMNs potentially has two advantages over a single HMN with the same dimension. A parallel combination of fluid resistances of multiple needle lumens yields a lower overall fluid resistance than the one of a single lumen. An array of multiple HMNs provides a larger fluid uptake area in the skin and therefore may increase the delivery rate.

2.6.2 Overview of Current Fabrication Approaches for Hollow Microneedles

Fabrication of HMNs involves a more elaborate process than that of SMNs because of the construction of the lumen. Several microfabrication approaches have been reported to successfully construct the lumen of HMNs. Table 1 is a summary table of the fabrication approaches of HMNs discussed in Section 2.3.

Table 1. Summary Table of the Fabrication Approaches of Hollow Microneedles. Fabrication approaches of hollow microneedles are categorized by the structural materials listed in the leftmost column. For each structural material, corresponding fabrication approaches for the microneedle shaft, lumen, and baseplate are listed in the three central columns with remarks listed in the rightmost column.

HMN structure material		Fabrication of MN shaft	Fabrication of MN lumen	Fabrication of base plate	Remark
Silicon		[1] Anisotropic wet etching [2] Isotropic dry etching [3] Saw dicing	DRIE	Unprocessed silicon as a base plate	(1) DRIE requires a high-cost equipment (2) Saw dicing is a serial process
Nickel		Electroplating onto a pre-constructed mold			Nickel is a known allergen to some sensitive individuals
Polymer	SU-8	Conventional UV lithography			(1) Combined with micromolding technique (2) <500 μm tall
		Conventional UV lithography + RIE	Laser drilling	Conventional UV lithography	Laser drilling is a serial process
	Polymethyl methacrylate (PMMA)	Deep X-ray lithography (DXRL)		Two additional micromolding steps	DXRL requires a synchrotron radiation source
	Ormocer®	Local polymerization within a small focal volume of a titanium:sapphire laser			Local laser polymerization is a serial process
	Clay / Polyimide	Solvent evaporation on a pre-constructed mold	Micromolding	Same with MN shaft	(1) <500 μm tall (2) Top-terminated lumen
	Polycarbonate (PC)	Injection molding	Laser drilling	Same with MN shaft	Laser drilling is a serial process
	polyoxymethylene (POM)	Injection molding			(1) 500 μm tall (2) Rounded tip
Glass		Conventional glass micropipette puller + microelectrode beveler		No base plate	Micropipette pulling is a serial process

Silicon-based MEMS techniques are widely used to fabricate HMNs with a submicron tip. The lumen of these HMNs is often constructed using a deep-reactive-ion-etching (DRIE) technique. To form the shape of HMNs, several fabrication approaches, including anisotropic wet etching [35], isotropic dry etching [36, 37], a combination of

isotropic and anisotropic dry etching [38], as well as saw dicing [39], have been reported. Electroplating of nickel onto a pre-constructed MN mold is commonly used to fabricate nickel MNs. Nevertheless, nickel is a known allergen material and the most common cause of contact allergy. [92] Laser micromachining is commonly employed to create three-dimensional (3D) structures. HMN structures have been obtained using the laser micromachining technique to locally polymerize Ormocer® within the small focal volume of the laser [54], to remove the lumen material from a pre-constructed SMN fabricated using UV lithography and RIE [51] or injection molding [59]. Glass micropipette pulling is another serial processing used to create HMNs. Deep X-ray lithography (DXRL) is utilized to construct polymethyl methacrylate (PMMA) HMNs with two exposure steps. [53] Nevertheless, to extend the lumen inside HMNs through the baseplate of the HMN array, two additional micromolding steps are required. In these approaches, relatively expensive equipment, facilities with limited availability, serial processes, or a known allergen material were involved as shown in Table 1. Solvent evaporation and a full injection molding process are potentially batch manufacturable processes. Nevertheless, no taller-than-500-μm HMNs have been demonstrated with these two fabrication approaches.

Conventional photolithography combined with a micromolding technique has been reported to simplify the fabrication process of HMNs. Using UV lithography into micromolds allows complex 3D structures to be defined with both the mask pattern in the lithography process and the topography of the micromold. With a pre-constructed reusable mold defining the tip of HMNs, the shaft and lumen of the needles as well as a baseplate are all fabricated using a UV-sensitive polymer. This conventional UV

lithography technique, widely used in the microelectronics industry [93], is batch-compatible and potentially scalable to high volumes. With this fabrication approach, HMNs with a height of 400-600 μm have been demonstrated. [45, 46, 94]

To meet the required process features for HMN manufacturing discussed in Subsection 2.6.1, a polymer-based fabrication process using UV lithography into micromolds needs to be developed to achieve 1 mm tall HMN arrays. Moreover, this integrative fabrication process may utilize potentially low-cost polymer materials, e.g., SU-8 for the HMN structure and PDMS as the micromolding material. UV lithography and micromolding methods are expected to have low mass production costs. [2] The flexibility of PDMS as a molding material is expected to facilitate the demolding processing.

2.7 Chapter Conclusion

In 1976, the concept of using micron-sized needles to deliver drug into skin was first introduced. Because of the lack of competent microfabrication technology, no demonstration of microneedles was reported until late 1990s. Since the year 2000, a variety of microneedles for drug delivery into skin have been presented. To make the manufacturing of hollow microneedles appropriate for single-use devices, several process features are desired. These process features include batch processing for high throughput and scalability for high-volume production, capability of creating complex hollow three-dimensional structures, and potential for low cost manufacturing. Nevertheless, most current hollow microneedle fabrication approaches involve serial processing, a known allergen material, or high-cost facilities or equipments. Therefore, a new fabrication approach using UV lithography, a conventional batch process, with polymers as

structural and micromolding materials is proposed to achieve high-throughput manufacturing and manageable fabrication cost. In Chapter 3, the concept and development of the new fabrication process for hollow microneedles as well as the characterization of fabricated needles are discussed.

CHAPTER 3

PYRAMIDAL-TIP HOLLOW MICRONEEDLE ARRAY

3.1 Introduction

Drug delivery through micromachined needles is of great interest to transport therapeutic agents, virus-like-particles, and other molecules into the body through the skin with minimal invasiveness and pain. Figure 23 shows schematic illustrations of an HMN system as well as the drug delivery into skin through the HMN system. Figure 23(a) shows a schematic depiction of an HMN system, consisting of an HMN array of four needles and a drug reservoir on the back of the HMN array. Following the successful insertion of HMNs into skin, force is applied to the back of the drug reservoir, driving the drug in the reservoir through the lumens of HMNs and into the skin, as shown in Figure 23(b).

In this chapter, a polymer-based fabrication process using UV lithography into micromolds and a fabricated HMN array with a baseplate are discussed. As discussed in Section 2.6, the fabrication approach of UV lithography into micromolds was developed because it allows construction of complex 3D structures using a widely used batch process and it utilizes potentially low-cost polymer materials.

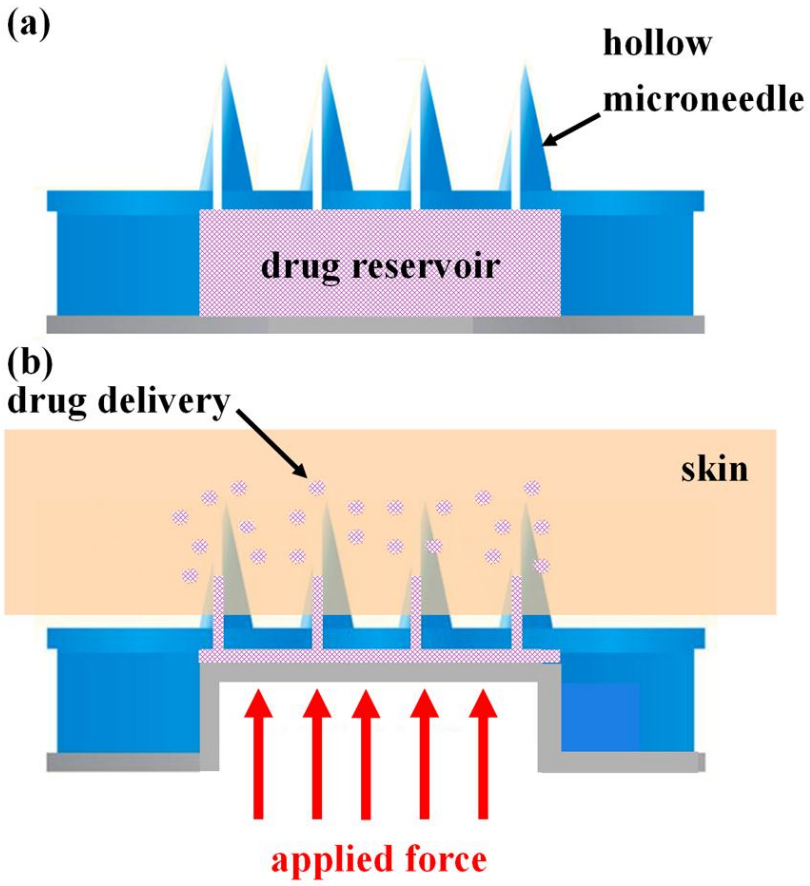

Figure 23. (a) A schematic depiction of a hollow microneedle system, consisting of a hollow microneedle array and a drug reservoir. (b) An illustration of administration of drug delivery using the hollow microneedle system.

Figure 24 shows schematic depictions of the desirable HMN structures discussed in this chapter. This HMN has three major components: a top pyramidal tip, a square shaft, and a baseplate. The lumen of the HMN has two openings: one is on the pyramidal slope, and the other is located on the bottom side of the baseplate. The pyramidal tip needs to be sharp to allow insertion of MNs into skin, and the lumen should be clog-free for subsequent fluid injection into skin. Formation of the lumen may present the most process difficulty, since it depends on complete development of the structural photoresist and minimal unintended UV radiation into the lumen discussed in the following section.

The schematic depictions were drawn using a computer-aided design (CAD) tool (SolidWorks, Dassault Systemes, Velizy, France). A 1 mm × 1 mm square pattern was extruded by 200 μm to draw a baseplate. On the top surface of the baseplate, a 400 μm × 400 μm square pattern was sketched and extruded by 570 μm to outline an MN shaft. The top surface of the MN shaft was extruded inward by 35°, instead of 0°, to draw a pyramidal tip of 285 μm in height, followed by a circular extruded cut of 80 μm in diameter through the MN and the baseplate as shown in Figure 24. The fabrication and mechanical characterization of the HMN of interest as well as its insertion performance into excised animal skin are discussed in this chapter.

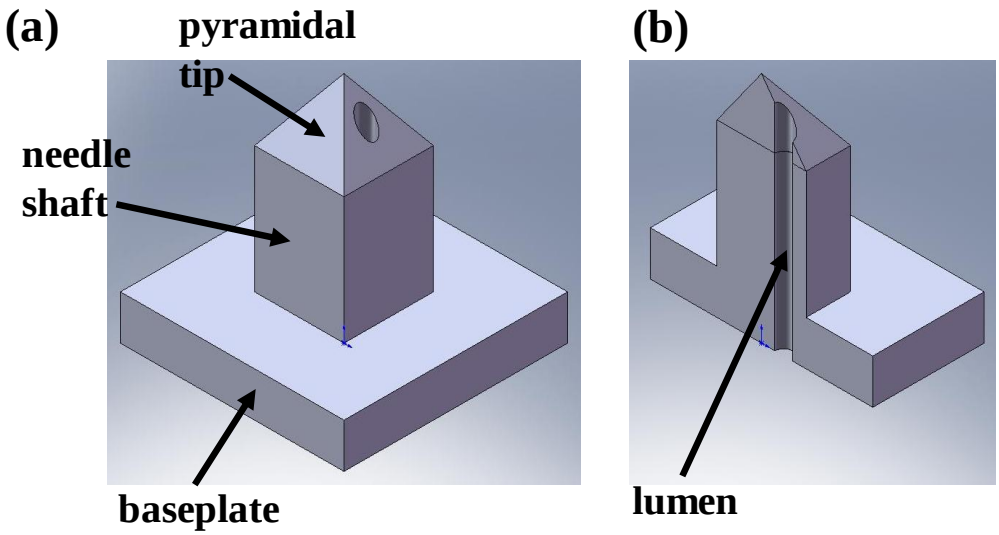

Figure 24. (a) A depiction showing the desirable hollow microneedle structure with a baseplate. (b) A cross-sectional view of the hollow microneedle structure, showing that the lumen has two openings connecting the back of the baseplate to the top of the pyramidal slope.

3.2 Microneedle Design

The parameters of the HMN design shown in Figure 24 need to be determined prior to the microfabrication. These design parameters include the height of the needle, the width of the needle shaft, the lumen diameter, and the angles of the slopes in the pyramidal tip. The height of the needle is chosen to be approximately 1 mm according to the rationale discussed in Subsection 2.6.1.

To determine the MN width, the associated insertion pain was first taken into consideration. Fruhstorfer studied the pain associated with insertion of lancets of 300 μm, 400 μm, and 800 μm in diameter and of 900 μm in length using a numeric rating scale (NRS) and reported no significant difference in pain score among these three lancet diameters. [95] Moreover, Gill reported comparable pain scores for the insertion pain of MNs measuring 160 μm, 245 μm, or 465 μm in width and 700 μm in length using a visual analog scale (VAS). [91] Therefore, these two studies suggest that for the MN width ranging from 160 μm to 800 μm, the MN width may not substantially affect the insertion pain. Diabetes is one of the potential applications of HMN drug delivery. [96] The original pen needles from BD for insulin injection are 29-gauge HNs [97], and the outer diameter of 29-gauge HNs is approximately 340 μm [98]. A MN width of 340 μm was therefore considered. Furthermore, Park reported that the fracture force of MNs increased significantly with the MN width. [26, 99] Therefore, the width of the HMNs was chosen as 400 μm.

The fluid resistance of a lumen is inversely proportional to the lumen radius to the fourth power according to the Poiseuille equation discussed in Subsection 4.4.4, and hence a large lumen diameter is desired to reduce the fluid resistance of the lumen. A

schematic illustration of the top view of the HMN is shown in Figure 25. The width of the needle is 400 μm, and the circle in the upper portion of the needle represents the needle lumen, terminating on one of the four slopes of the pyramidal tip. The circle in Figure 25 denotes the circle with the largest lumen diameter. A simple trigonometric calculation based on the needle width of 400 μm indicates that the lumen radius, r, is approximately 83 μm. Nevertheless, with the needle design shown in Figure 25, the thickness of the needle wall at Point A is zero, resulting in no SU-8 formation at Point A and possible fluid leakage from the needle during the fluid injection. Therefore, a 20 μm clearance between the lumen and the upper edge of the needle is chosen to provide sufficient mechanical strength of the SU-8 needle wall at Point A during MN insertion and to avert the potential fluid leakage. The 20 μm clearance reduces the lumen radius from 83 μm to 63 μm, and therefore a lumen radius of 60 μm is chosen, leading to a lumen diameter of 120 μm for the HMN design.

The angle of the four slopes in the pyramid tip of the HMN is chosen as 35° to reduce the internal reflection of the incident UV radiation at the SU-8 / PDMS interface, discussed in Subsection 3.3.2. Therefore, the four key design parameters of the HMN design shown in Figure 24, including the height of the needle, the width of the needle shaft, the lumen diameter, and the angle of the slopes in the pyramidal tip, are all determined.

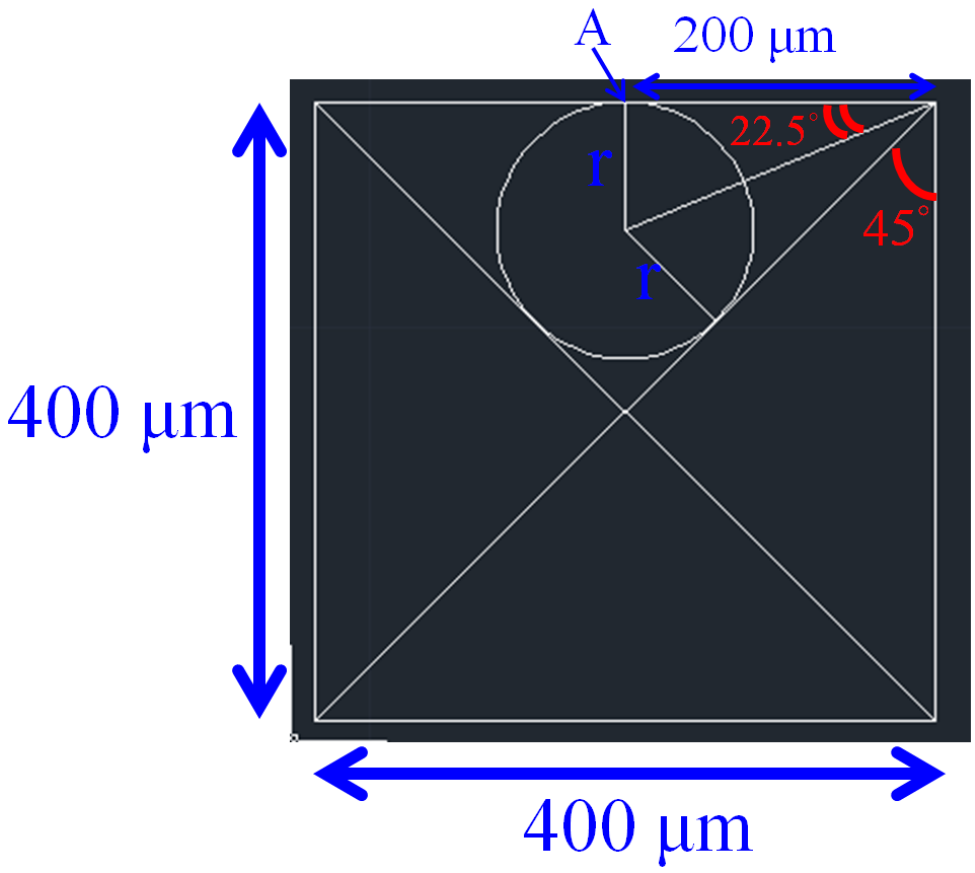

Figure 25. A schematic illustration of the top view of the HMN shown in Figure 24. The width of the needle is 400 µm. The circle in the upper portion of the needle represents the lumen of the needle.

3.3 Microfabrication Process Development

Advantages of using UV lithography into micromolds to make the manufacturing of HMNs appropriate for single-use devices are discussed in Section 2.6. To realize this fabrication approach, several key issues need to be addressed. To construct 1 mm tall MNs, the photosensitive structural material, i.e., the photoresist, used in UV lithography needs to be sufficiently transparent to UV radiation up to 1 mm in thickness. Microneedles are structures of high aspect ratios. Hence, the photoresist shall be capable of being patterned for high-aspect-ratio structures. SU-8, as discussed in Subsection 2.5.1,

has been demonstrated to meet these requirements.

The needle lumen may raise additional fabrication difficulty. In the development step of UV lithography, to fully develop the lumen of unexposed SU-8 requires fresh SU-8 developer to move through the developed portion of the lumen and to solvate any unexposed SU-8 in the lumen. Moreover, unintended SU-8 crosslinking in the lumen is possible and can be caused by various factors, which are discussed in detail in Subsection 3.3.2 and Subsection 3.4.4. Therefore, to ensure the formation of the needle lumen in 1 mm tall MNs, each step in UV lithography, including baking, exposure, and development steps, and the design of the micromold must be investigated.

Using UV lithography into micromolds may involve photomask alignment with the micromolds through 1 mm thick SU-8. Given that the depth of focus of the alignment microscopes in typical mask aligners ranges from 300 μm to 400 μm [100, 101], particular care needs to be taken to align the photomask with the micromolds through 1 mm thick photoresist.

A schematic process flow for the fabrication of SU-8 HMNs using UV lithography into PDMS micromolds is shown in Figure 26. In this process flow, SU-8 is cast onto a pre-constructed PDMS mold (Figure 26(a) and Figure 26(b)), followed by the softbake of SU-8. The subsequent two UV-exposure steps with different dosages and separate masks define the HMN structure and a baseplate, as shown in Figure 26(c) and Figure 26(d), respectively. The entire structure of the SU-8 master is demolded from the PDMS mold, followed by the development of SU-8 (Figure 26(e)) to create the SU-8 HMN with a baseplate (Figure 26(f)).

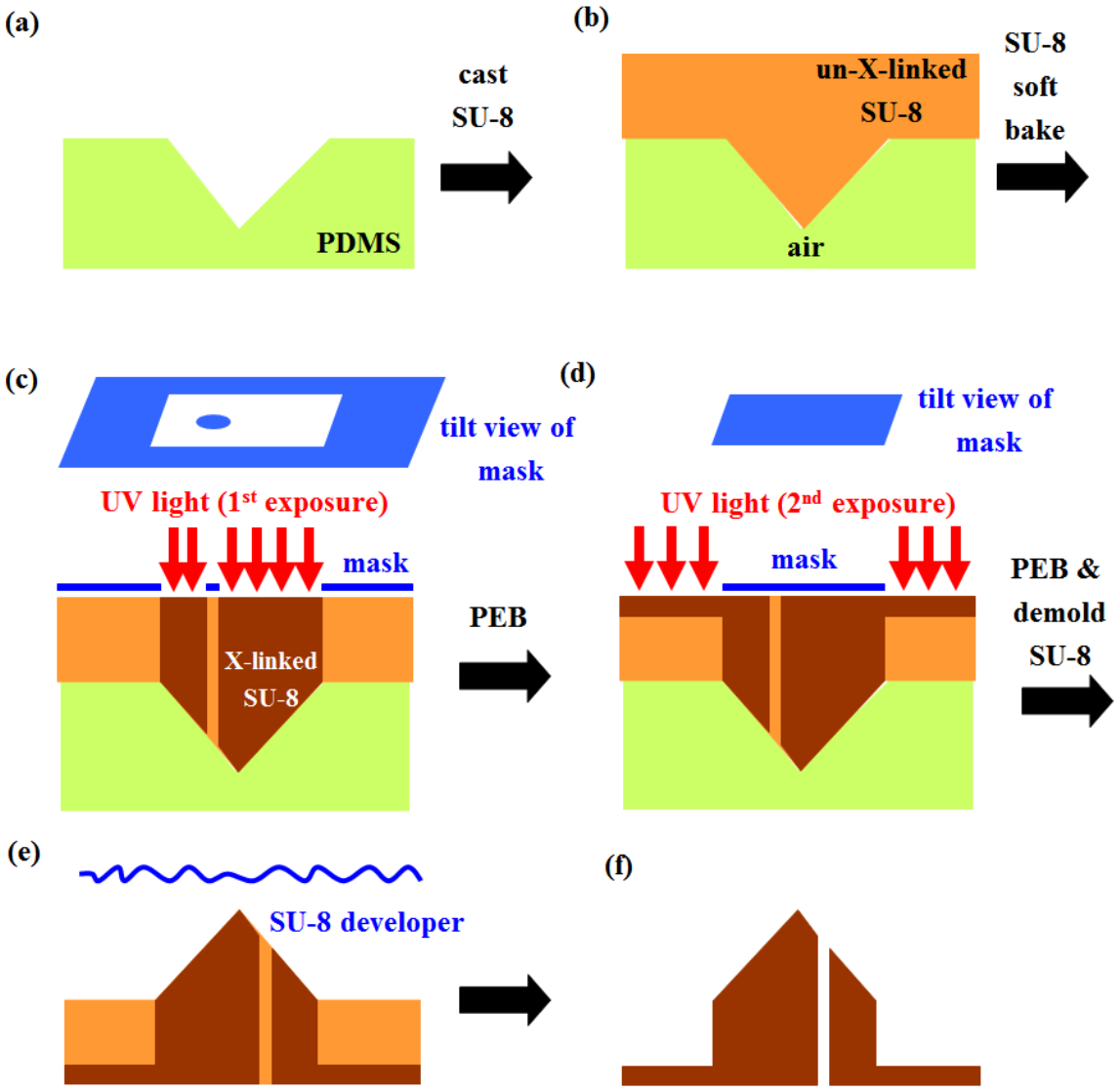

Figure 26. Fabrication process flow for the hollow SU-8 microneedle array.

With advantages of using UV lithography into micromolds discussed in Section 2.6, this process flow nevertheless may involve several reasonable fabrication concerns that need to be addressed. To create tall SU-8 structures with a single coating or casting, SU-8 with higher viscosity is needed [69]. Encapsulation of micromolds with SU-8 of high viscosity may result in air bubbles at the bottom of the micromolds. Moreover,

reflection of the UV radiation at the SU-8 / PDMS interface during the first exposure may cross-link the SU-8 in the lumen, leading to a clogged lumen. Therefore, the reflection of the UV radiation at the SU-8 / PDMS interface needs to be analyzed. SU-8 is softbaked at an elevated temperature, therefore thermal expansion of the polymeric mold in the SU-8 softbake process needs to be investigated to ensure proper alignment between the photomask and the mold in subsequent exposure steps. These three issues as well as other fabrication concerns are addressed in this section.

3.3.1 Elimination of Trapped Bubbles by Back-Side Vacuuming

With SU-8 preheated at 60 ℃ and the PDMS mold treated using oxygen plasma for better encapsulation of the micro-trenches, a significant number of air bubbles were still observed at the bottom of the PDMS trenches following the casting of SU-8 onto the PDMS mold, as shown in Figure 27(a).

To eliminate these air bubbles, the SU-8/PDMS sample was placed at the center of a rubber plate where there is an opening connected to a vacuum pump. Because of the gas permeability of PDMS [102], the air trapped at the bottom of the PDMS trenches was pulled through the PDMS mold and subsequently removed by the vacuum pump, as shown in Figure 26(b). An optical micrograph of the top side of the SU-8/PDMS sample following a three-hour backside vacuuming (BSV) process is shown in Figure 27(b), and no air bubble is observed at the bottom of the PDMS trenches under an optical microscope.

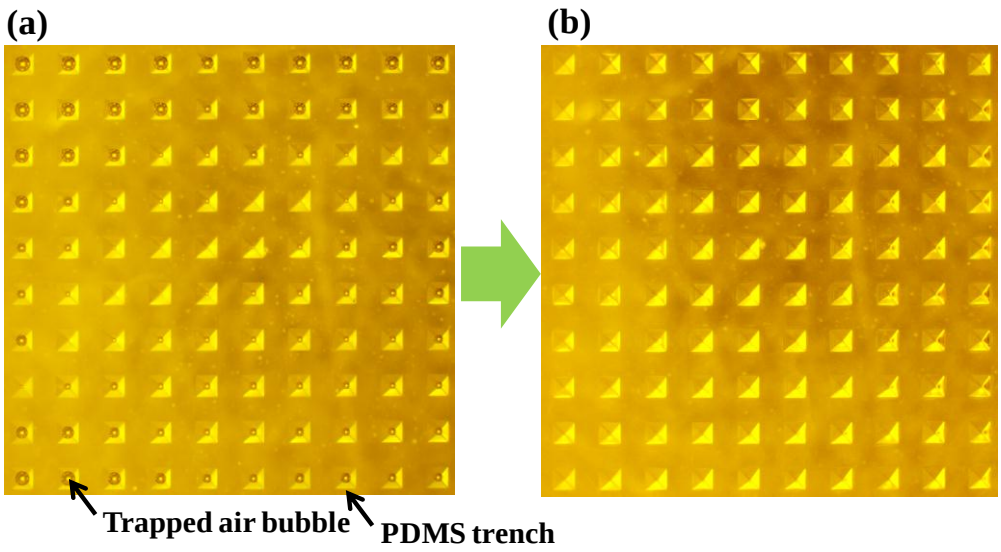

Figure 27. Optical micrographs of the top view of the SU-8/PDMS sample in Figure 26(b) before (a) and after (b) the backside vacuuming process. (a) More than 50 air bubbles of various dimensions trapped at the bottom of the PDMS trenches. (b) Elimination of the trapped air bubbles.

3.3.2 Internal Reflection at the Interface

In addition to the intended exposure shown in Figure 26(c), undesirable exposure may occur because of the reflection of UV light at the SU-8/PDMS interface shown in Figure 28(a). This reflected light is a result of the mismatch in the refractive indices of SU-8 and PDMS. This exposure of SU-8 may lead to undesired crosslinking in the lumen, inhibiting flow through the lumen.

To estimate the intensity of the reflected UV light from the SU-8/PDMS interface with different incident angles, the law of reflection, Snell's law of refraction, and Fresnel's equations were used. [103] Figure 28(a) shows a schematic illustration of different UV rays at the SU-8 / PDMS interface and their corresponding angles to the normal of the interface. Given that the refractive indices of SU-8 and PDMS are 1.59 and 1.41 [104, 105], respectively, the transmission angle (φ) can be expressed as a function of

the incident angle (θ) using Snell's law. The reflection coefficient (R), defined as the ratio of the intensity of the reflected UV light to that of the incident UV light, can be determined using Fresnel's equations:

$$R = \frac{R_{TM} + R_{TE}}{2} \quad \text{.....(1)}$$

where

$$R_{TM} = \frac{\tan^2(\theta - \varphi)}{\tan^2(\theta + \varphi)}$$

and

$$R_{TE} = \frac{\sin^2(\theta - \varphi)}{\sin^2(\theta + \varphi)}.$$

Figure 28(b) shows the calculated reflection coefficient (R) plotted as a function of the incident angle (θ) and the inclined angle of the PDMS trench (α). As shown in Figure 28(b), the reflection coefficient (R) first increases slightly with the incident angle (θ) for θ less than 50° and increases significantly with θ for θ larger than 50°. To minimize this substantial increase of R with θ for θ larger than 50°, an approximate trend line of the linear relation of R and θ is drawn for θ larger than 50° and is shown as the red dashed line in Figure 28(b). The trend line intercepts the θ axis, where R equals zero, at θ of approximate 55°, corresponding an inclined angle of the PDMS trench (α) of 35°. Therefore, the inclined angle of the PDMS trench is chosen to be 35° to minimize the substantial increase of R with θ.

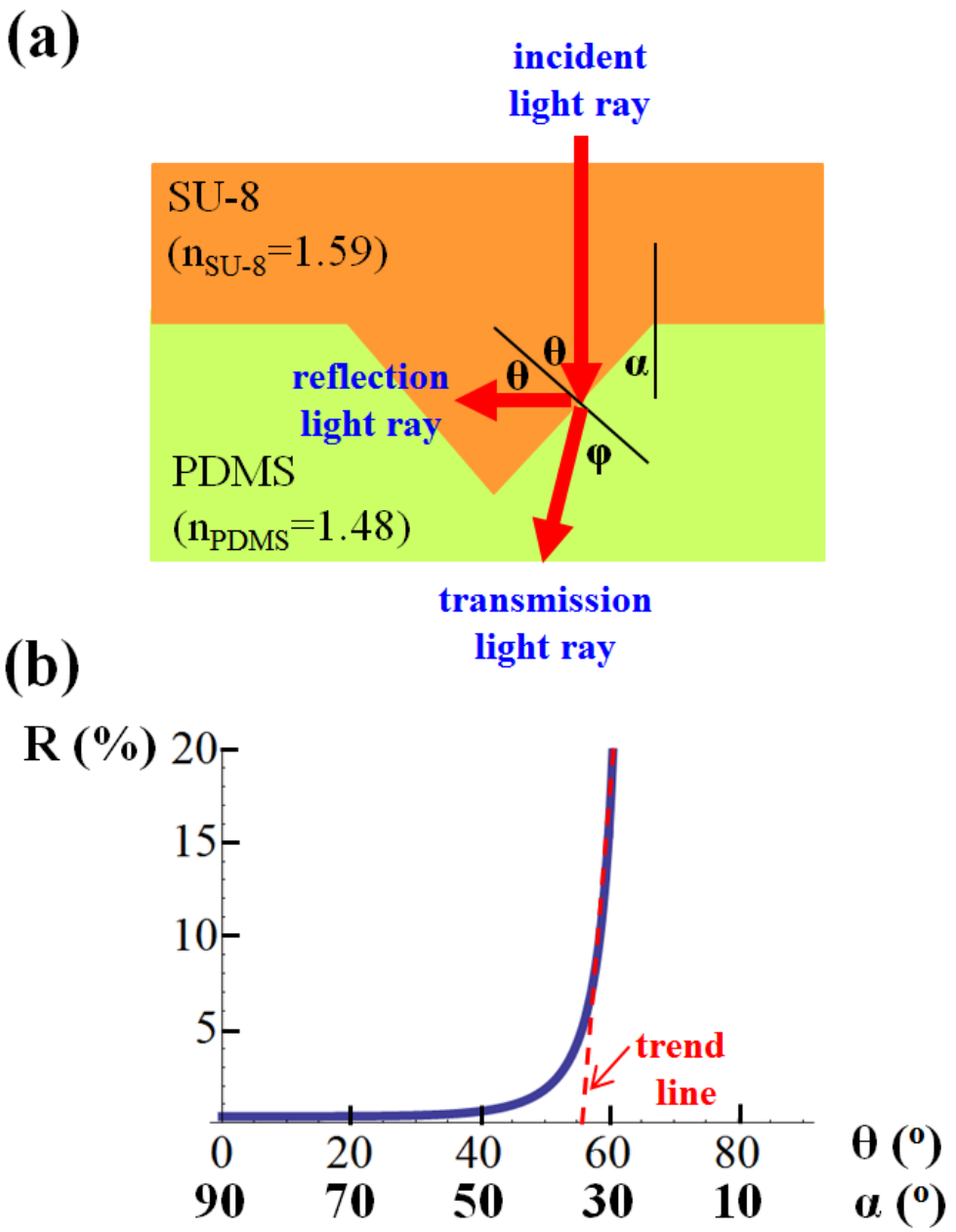

Figure 28. (a) A schematic illustration of different UV rays at the SU-8/PDMS interface and their corresponding angles to the normal of the interface. (b) A chart of the reflection coefficient (R) as a function of the incident angle (θ) and the inclined angle of the PDMS trench (α). An approximate trend line of the substantial increase of R with θ for θ larger than 50° is shown as a red dashed line.

A chart of R as a function of θ and α for the R range of 0 % to 100 % is shown in Figure 29. As θ increases to close to 62.5°, i.e., α decreases to close to 27.5 °, R increases to approximately 100%. When the intensity of the reflected UV light is approximately equal to that of the incident UV light, the reflected UV light may lead to undesired SU-8 crosslinking in the lumen as the incident UV light leads to the intended SU-8 crosslinking that forms the needle structure. Hence, it is required for α to be larger than 27.5° to ensure the formation of the lumen in the pyramidal tip. Given that the base of the pyramidal tip, i.e., the width of the needle, is 400 μm and the lower limit of α is 27.5°, a simple trigonometric calculation suggests that the maximum of the height of the pyramidal tip is 384 μm for well-defined lithographic formation of the lumen in the pyramidal tip.

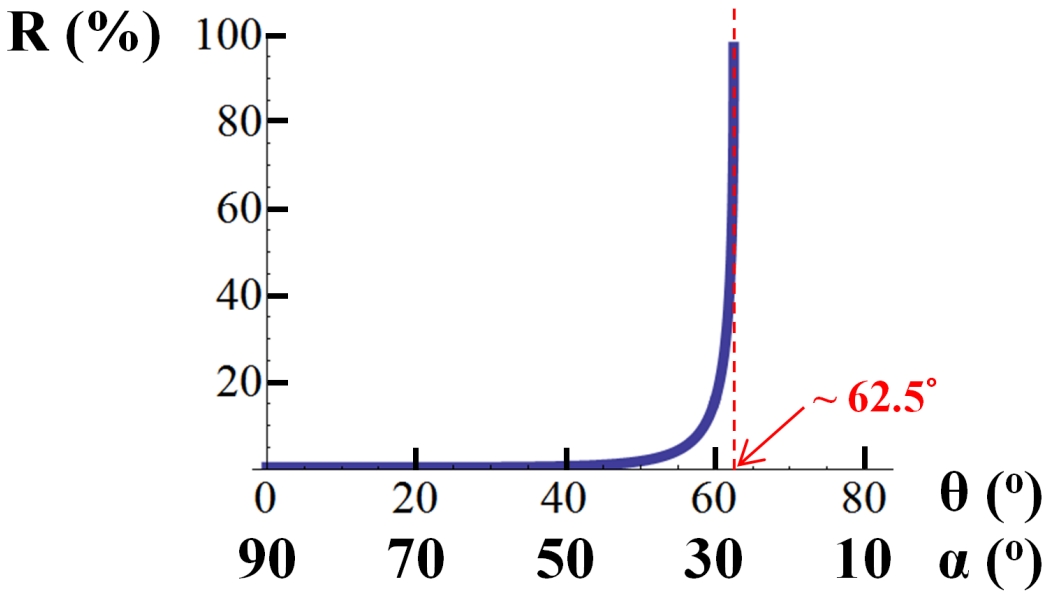

Figure 29. A chart of the reflection coefficient (R) as a function of the incident angle (θ) and the inclined angle of the PDMS trench (α) for the R range of 0 % to 100%. As θ increases close to 62.5°, R increases to approximate 100%.

3.3.3 Compensation for the Thermal Expansion of a Polymer Mold with Photomask Design

In the SU-8 softbake process, the elevated temperature on the hotplate caused the solid PDMS mold to expand while the SU-8 in liquid state was being stretched horizontally along the PDMS mold. Figure 30(a) shows a schematic depiction of the top view of the SU-8/PDMS sample with a 10×10 array of PDMS trenches. Schematic depictions of the cross-sectional view of one side of the SU-8/PDMS sample prior to and after the softbake process are shown in Figure 30(b) and Figure 30c, respectively.

Since the location of the needle shaft is defined by the mask pattern on the photomask and that of the needle tip is determined by the PDMS trench in the first UV exposure step as shown in Figure 26(c), to construct a well-defined MN structure the alignment between the mask pattern and the PDMS trench is of importance. Therefore, with the dimension of the PDMS mold increased in the softbake process, the first UV exposure with a set of mask patterns designed based on the mold dimension prior to the softbake process resulted in a shift between the needle shaft and tip as shown in Figure 30(d). The shift is a maximum for outmost needles in the needle array.

To eliminate this undesirable shift in the MN structure, the thermal expansion of the PDMS mold in the softbake process was taken into consideration during the design process of the photomask. With a newly-designed mask pattern whose dimension was designed to compensate for the thermal expansion of the PDMS mold, the location of the mask pattern is aligned with the PDMS trenches, resulting in a well-defined needle structure, as shown in Figure 30(e). As shown in Figure 30(d) and Figure 30(e), the desired formation of the needle structure relies on the good lateral alignment between the

photo mask and the PDMS trenches. The patterns are insensitive to thermal mismatch in the vertical direction, since the incident UV light shines along the vertical direction.

To design the new photomask to compensate the thermal expansion of the PDMS mold in the softbake process, this expansion was estimated with the equation of linear thermal expansion [106],

$$\frac{\Delta L}{L_0} = \alpha_L \Delta T \quad \text{.....(2)}$$

where L_0 is initial length, ΔT is the temperature change of the object, ΔL is the change in the length of the object, and α_L is the coefficient of linear thermal expansion. With an α_L of 3.1×10^{-4} $(℃)^{-1}$ for PDMS [107], ΔT of 95 ℃ for the temperature increase from the room temperature of 25 ℃ to the softbake temperature of 115 ℃, and L_0 of 3800 μm for the distance from the center to the rightmost or leftmost point of the ten PDMS trenches, which is half of d_1 shown in Figure 30(b), the thermal expansion for the rightmost or leftmost trench was estimated to be 106 μm. The photomask pattern was thus adjusted throughout the entire array to compensate the thermal expansion of the PDMS mold.

This compensation scheme is solely based on the thermal expansion of the PDMS substrate, as opposed to considering the detailed thermal expansion characteristics of the SU-8/PDMS composite. Such detailed compensation could be achieved, e.g., by considering the cooling of the SU-8/PDMS composite after the softbake between the softbake temperature of 115 ℃ and the glass transition temperature (Tg) of uncrosslinked SU-8 (50 ℃ [108]). In the cooling step, the temperature of the SU-8 decreases faster than

that of the PDMS mold, because (1) the thermal conductivity of SU-8 is higher than that of PDMS, i.e., 0.30 W/mK for SU-8 and 0.17 W/mK for PDMS [69, 109], and (2) the top surface of the SU-8 is in contact with room-temperature ambient air while the bottom surface of the PDMS mold is in contact with the hotplate with a slowly decreasing temperature from the softbake temperature of 115 ℃. When the temperature of the SU-8 reduces below its glass-transition temperature of 50 ℃ for SU-8 prior to the PEB process, the SU-8 solidifies and prevents the PDMS mold from further shrinkage even though the temperature of the PDMS mold continues to decrease to room temperature. Therefore, such effect during the cooling of the SU-8/PDMS composite reduces the dimension of the PDMS trench array, i.e., d_2 in Figure 30(e), and may lead to additional alignment error.

Fabricated MNs with different photomasks used in the first UV exposure step are shown in Figure 31 for comparison. Figure 31(a) and Figure 31(b) show optical micrographs of the leftmost and rightmost two MNs of the sample in Figure 30(d) fabricated with a non-compensation photomask, respectively. In Figure 31(a), a shift of the needle tip from the needle shaft was observed to be 81 μm toward the left in the leftmost needle. In Figure 31(b), the shift of the needle tip was 123 μm toward the right in the rightmost needle. The observation of the outward shift of the needle tips indicated an expansion of the PDMS mold, by which the needle tips were defined. Furthermore, this observation suggested the expansion of the PDMS mold was 102 μm for leftmost and rightmost needles and there was a 21 μm misalignment between the PDMS mold and the photomask. The observed 102 μm shift of the needle tip was close to the theoretical calculation of 106 μm. The 21 μm mis-alignment can be considered as the PDMS mold shifting 21 μm toward the right or the photomask shifting 21 μm toward the left.

Figure 31(c) and Figure 31(d) show optical micrographs of the leftmost and rightmost two needles of the sample, respectively, fabricated with a compensation photomask that compensates only for the thermal expansion of the PDMS substrate. The shifts between the needle tip and shaft were significantly reduced in both leftmost and rightmost needles. Therefore, with the newly-designed photomask, the thermal expansion of the PDMS mold in the softbake process can be effectively compensated to construct well-defined MN structures, and the observed shifts (~30 μm) may be a result of the discussed shrinkage effect during the cooling of the SU-8 / PDMS composite. An illustration of the SU-8 / PDMS sample exposed with a compensation mask in the first UV exposure step with the shrinkage of the SU-8 / PDMS composite during the cooling taken into consideration is shown in Figure 32. The observed shifts in Figure 31(c) and (d) are denoted as Δd_{23} in Figure 32.

The effect of the observed shifts in an array on large area manufacturing of multiple arrays is analyzed in the following discussion. The shrinkage effect during the cooling of the SU-8 / PDMS composite yields the observed shifts of 30 μm over the distance, L_0, of 3.8 mm from the center point of the ten PDMS trenches. Assume the large area manufacturing of multiple arrays is performed on an eight-inch wafer with a radius of four inches, i.e., 101.6 mm. Therefore, the shrinkage effect is expected to yield a shift of 802 μm over the wafer radius of 101.6 mm. The approximately 800 μm shift for MN arrays located adjacent to the wafer edge leads to failures in the formation of MN tips.

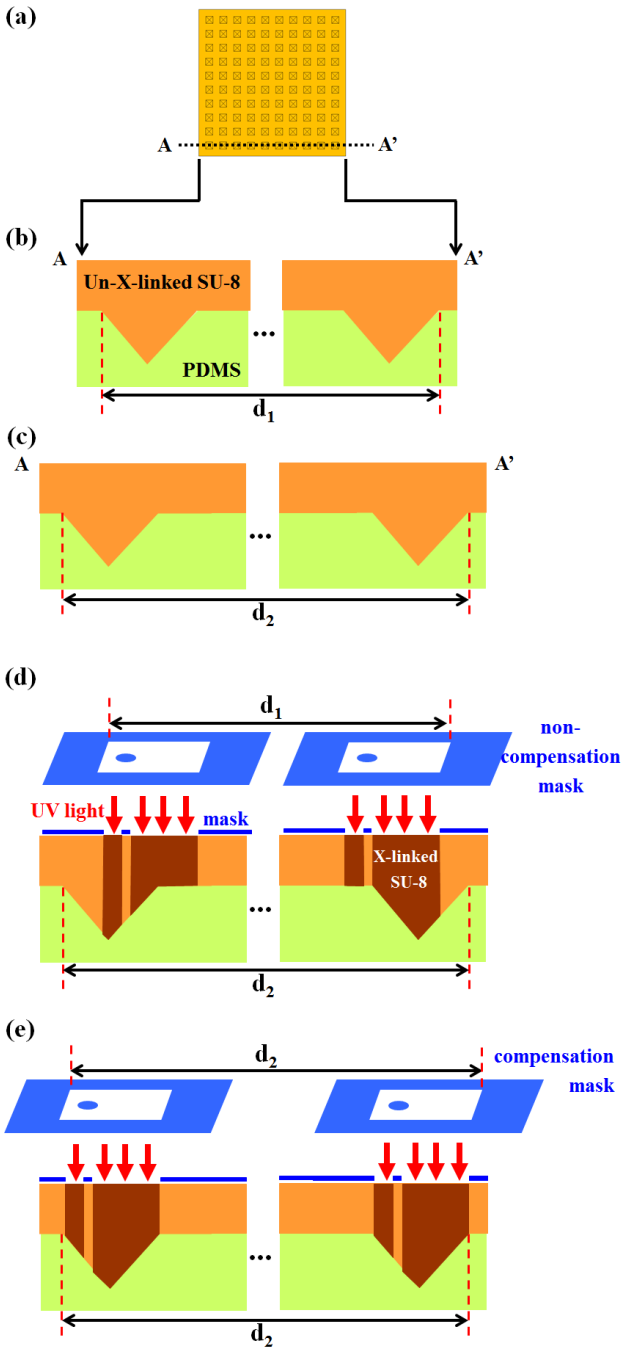

Figure 30. Schematic illustration of the thermal expansion of the PDMS mold. (a) A schematic depiction of the top view of the SU-8/PDMS sample. The PDMS trenches in a 10×10 array are visible through the SU-8. (b) A schematic depiction of the cross-sectional view of one side (A-A' in (a)) of the SU-8/PDMS sample prior to the softbake process. The ten PDMS trenches on one side of the SU-8/PDMS sample are represented by the leftmost and rightmost ones. (c) A depiction of the sample after the softbake process, showing the thermal expansion of the PDMS mold. (d) An illustration of the SU-8/PDMS sample exposed with a non-compensation photomask in the first UV exposure process. (e) An illustration of the sample exposed with a compensation mask in the first UV exposure process.

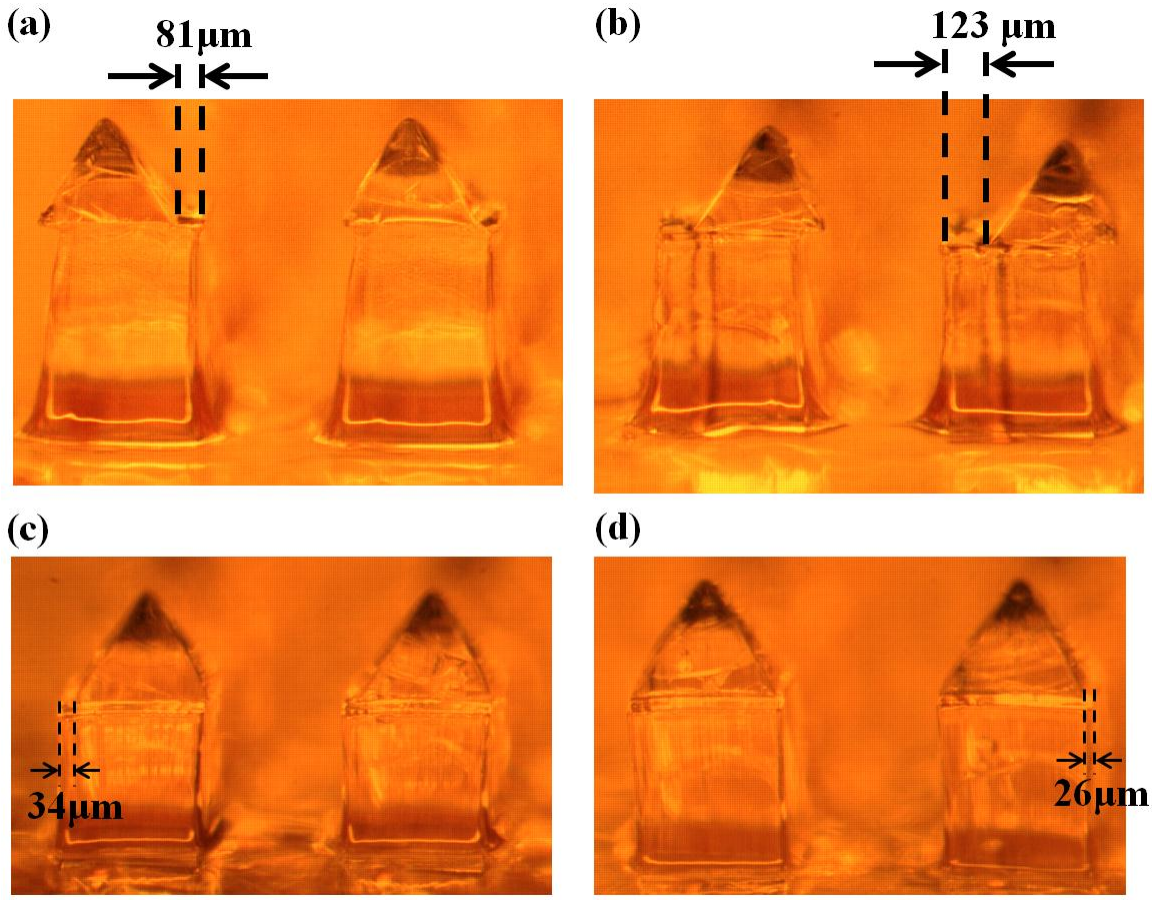

Figure 31. (a) and (b) Optical micrographs of the leftmost and rightmost two microneedles of the sample fabricated with a non-compensation photomask, respectively. The shift between the needle tip and shaft is 81 µm for the leftmost needle. The shift between the needle tip and shaft is 123 µm for the rightmost needle. (c) and (d) Optical micrographs of the leftmost and rightmost two needles of the sample fabricated with a compensation photomask, respectively. The shifts between the needle tip and shaft were significantly reduced.

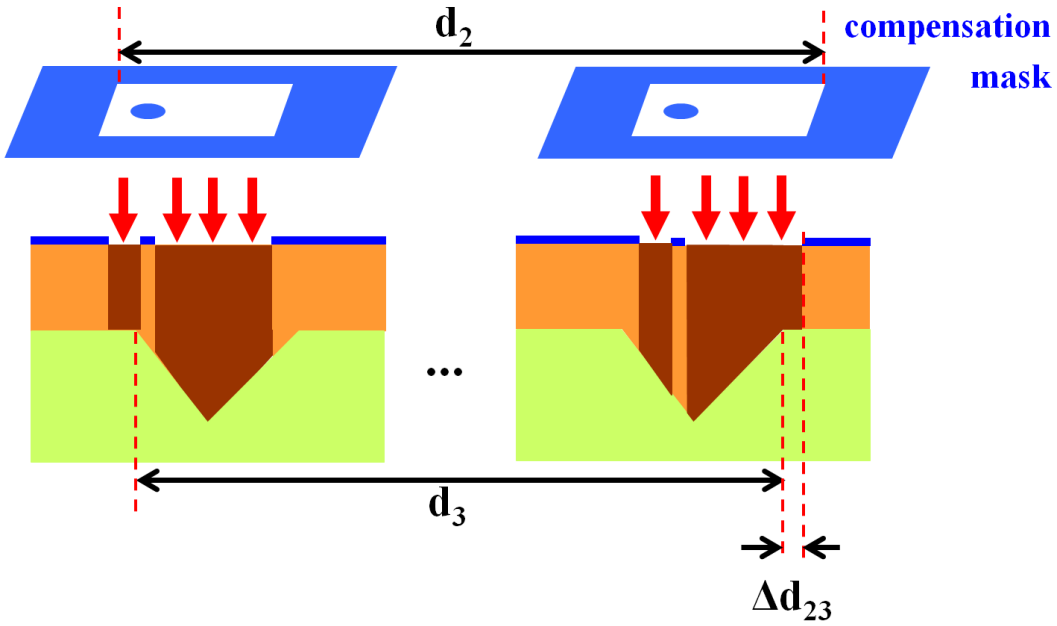

Figure 32. An illustration of the SU-8 / PDMS sample exposed with a compensation mask in the first UV exposure process with the shrinkage effect of the SU-8 / PDMS sample during the cooling taken into consideration. Δd_{23} is approximately 30 µm as shown in Figure 31(c) and (d).

To further reduce the shift between the needle tip and shaft, an analytical model of the temperature dynamics of the SU-8 / PDMS composite during the cooling step needs to be developed and applied to the design of the photomask. Such a detailed compensation scheme may become more important when considering large area manufacturing of multiple arrays. For batch manufacturing of multiple arrays, the temperature control in the softbake process may become a critical process parameter, since the L_0 in Equation 2 increases with the number of arrays and a small change in ΔT may result in a large variation in ΔL for arrays located adjacent to wafer edges. In addition to analytical systematic compensation for multiple arrays, experiment-based individual compensation for each array on an eight-inch photomask may be performed for batch manufacturing of multiple arrays.

3.3.4 Two PEB Steps for A Dual-Exposure Process

The alignment between the photomask and the perimeter of the PDMS trench during the two exposure processes (Figure 26(c) and Figure 26(d)) presents a technical difficulty, since the alignment is performed between two objects with a vertical distance of 800 μm, which is the thickness of the SU-8.

To prevent this alignment difficulty during the second exposure process (Figure 26(d)), a PEB step was performed following the first UV exposure step. With the addition of this PEB step the boundary between exposed and unexposed SU-8 became visible under the optical microscope of the aligner. Figure 33 shows an optical micrograph of the top view of the SU-8/PDMS sample following this PEB step. The perimeter of the exposed SU-8 needle shaft, which is a boundary between exposed and unexposed SU-8, is visible as shown in Figure 33 and serves as an alignment mark during the subsequent alignment for the second UV exposure. The alignment difficulty was significantly reduced for the second exposure process, since the alignment of the photomask was performed to the alignment mark on the top surface of the SU-8, instead of to the perimeter of the PDMS trench at the bottom of the SU-8 layer.

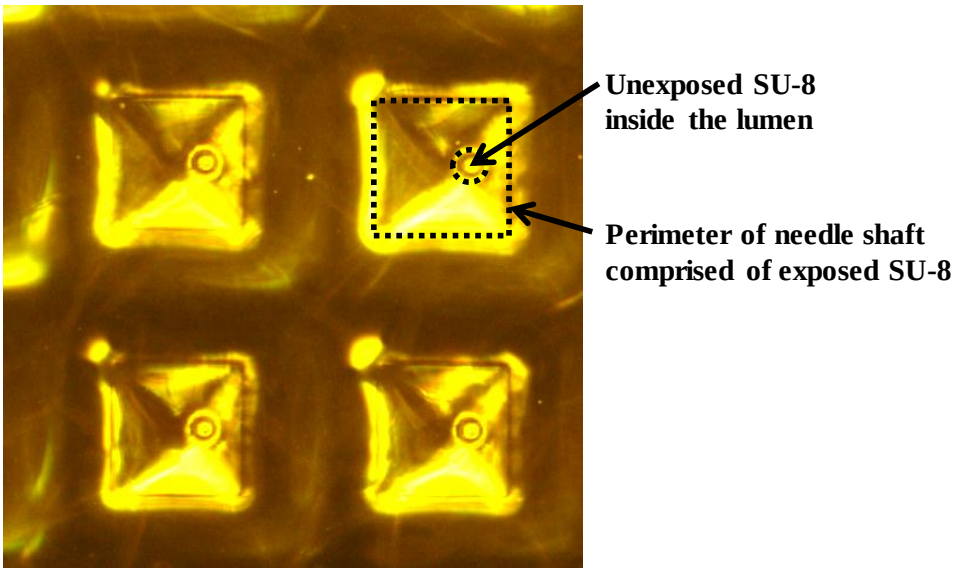

Figure 33. An optical micrograph of the top view of the SU-8/PDMS sample in Figure 26(c) following the first post-exposure-bake step. Four needles in an array of two-by-two are shown. A clear image of the perimeter of the exposed SU-8 because of the first PEB step on the top surface of the SU-8 is visible and serves as an alignment mark in the subsequent alignment for the second exposure process.

Moreover, since the second UV lithography process (Figure 26(d)) is to define the baseplate that is located on the top of the SU-8, the function of the PEB step following the second UV exposure is to provide thermal energy to the top of the SU-8. Compared to a hotplate where the thermal energy is supplied to the bottom of the SU-8/PDMS sample, in an oven the thermal energy is provided to the top surface of the SU-8 where the top surface is in direct contact with the heated air. Therefore, the second PEB step was performed in an oven to define the baseplate on the top of the SU-8.

In addition to the alignment difficulty caused by aligning two objects with a vertical distance of 800 μm, the alignment difficulty in the first UV exposure, shown in Figure 26(c), is higher than the one in the second UV exposure, shown in in Figure 26(d) because of insufficient illumination on the PDMS trench from the optical microscope because of the narrow openings on the photomask. Since the illumination is stronger on

the top surface of the SU-8 than on the PDMS mold located at the bottom of the SU-8, this increased alignment difficulty can be alleviated if the alignment of the photomask is performed to the top surface of the SU-8, instead of to the PDMS mold. To obtain a new alignment mark on the top surface of the SU-8 for the alignment in Figure 26(c), the UV exposure and PEB steps in Figure 26(d) can be performed prior to the similar steps in Figure 26(c). Because of the UV exposure and PEB steps in Figure 26(d), the boundary between the defined baseplate and the undefined MN shaft becomes clear, and this boundary can serve as an alignment mark, which is on the top surface of the SU-8 instead of the bottom of the SU-8, for the alignment in Figure 26(c).

3.3.5 Increased UV Dosage for Thick SU-8 Processing

The Beer-Lambert law states that the intensity of light decreases exponentially as the light travels through a medium [110], and as a result the energy dosage decreases exponentially as the light travels into the medium. Therefore, to cross-link the bottom portion of the SU-8, a sufficient, and usually high, UV dosage is required at the top surface of the SU-8 in thick SU-8 processing. To determine the required UV dosage for 1 mm tall SU-8 microstructures, a study of the SU-8 data sheet from its manufacturer, MicroChem Corp., as well as the literature on thick SU-8 fabrication was conducted.

In the SU-8 data sheet [69], exposure with 365 nm wavelength (i-line) radiation is recommended. A chart of suggested exposure dosages as a function of SU-8 thicknesses up to 200 μm is shown in Figure 34 with data points obtained in the SU-8 data sheet. The trend line is generated using the Microsoft Excel 2010 software with an exponential regression model. Extrapolation of these data points to an SU-8 thickness of 1000 μm indicates the suggested exposure dosage is 9000 mJ/cm^2 for 1 mm thick SU-8. In Figure

35, a chart with the same data points and a different trend line generated instead using a linear regression model is shown. Extrapolation with a linear-model trend line suggests an exposure dosage of 1050 mJ/cm^2 for 1 mm thick SU-8, as shown in Figure 35. Therefore, extrapolation with trend lines generated using different regression models indicates significantly different UV dosage for 1 mm thick SU-8.

In the literature, Despont et al. reported construction of 1200 μm tall SU-8 microstructures using an exposure dosage of 2000 mJ/cm^2 with 400 nm wavelength radiation and a linear increase of the required exposure dosage with respect to the SU-8 thicknesses ranging from 20 μm to 1200 μm. [111, 112] Therefore, to construct 1000 μm tall SU-8 MNs with a baseplate, a UV dosage of ~2000 mJ/cm^2 with 365 nm wavelength radiation was first evaluated.

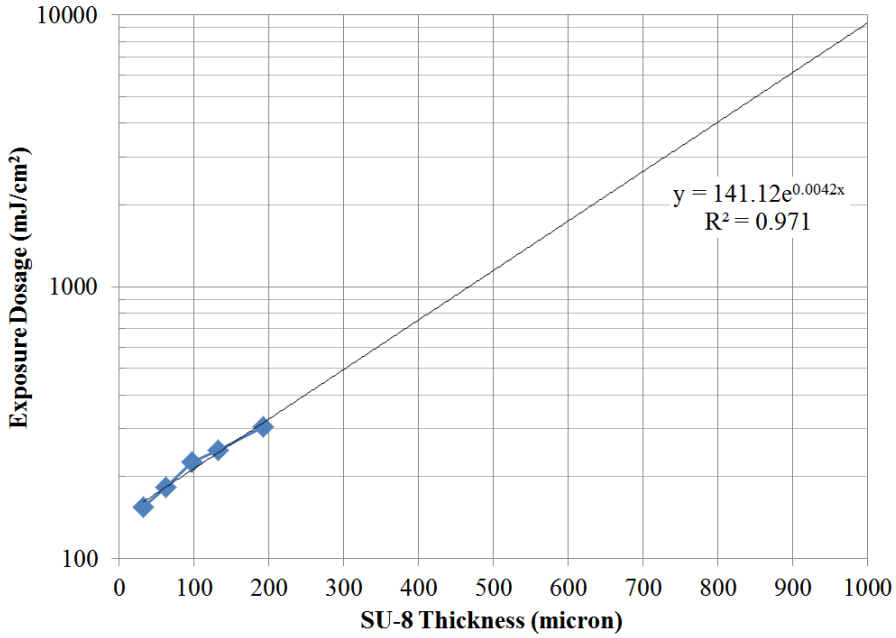

Figure 34. A chart of suggested exposure dosages as a function of SU-8 thicknesses with data points obtained in the SU-8 data sheet from its manufacturer, MicroChem Corp. [69] The trend line is generated using the Microsoft Excel 2010 software with an exponential regression model.

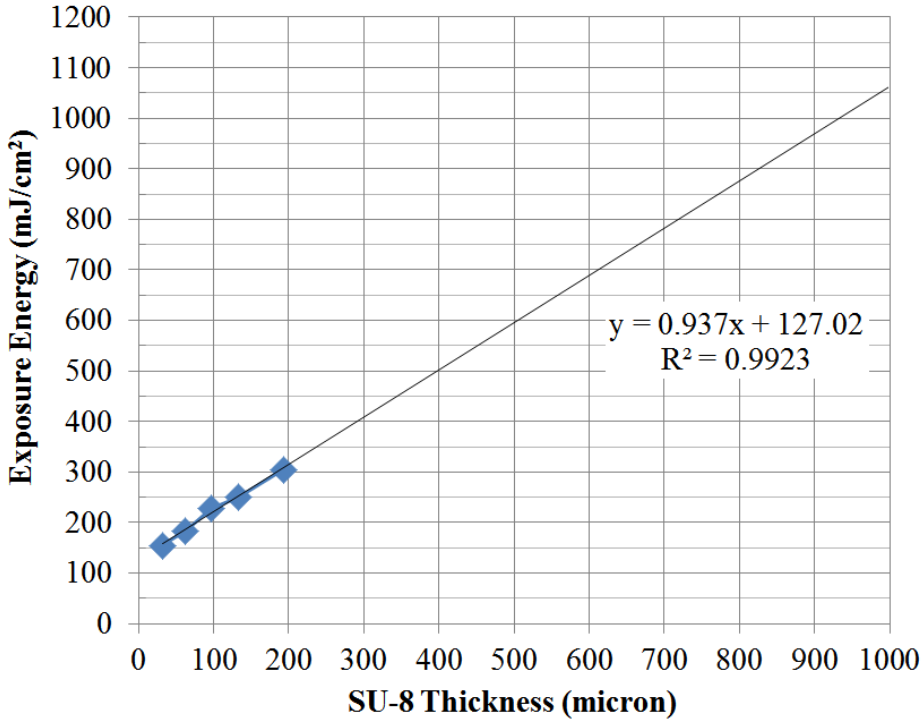

Figure 35. A chart of suggested exposure dosages as a function of SU-8 thicknesses with the same data points in Figure 34. A linear regression model is used to generate the trend line.

Figure 36 shows two optical micrographs of the side view of three MNs fabricated with different UV dosages in the first exposure shown in Figure 26(c). The three MNs shown in Figure 36(a) and Figure 36(b) were fabricated with a UV dosage of 2250 mJ/cm^2 and 3000 mJ/cm^2 in the first exposure, respectively. In Figure 36(a), the MN tips are not defined because of an insufficient UV dosage at the MN tips. With the UV dosage at the top surface of the SU-8 increased from 2250 mJ/cm^2 to 3000 mJ/cm^2, the UV dosage at the MN tips, which locate at the bottom of the SU-8, increases proportionally, resulting in well-defined MN tips, as shown in Figure 36(b). Therefore, the UV dosage in the first exposure was set as 3000 mJ/cm^2 to define the shaft and tip of MNs. A similar observation that a higher UV dosage in the exposure results in thicker

well-defined SU-8 is reported in [113].

The UV dosage of 3000 mJ/cm^2 is significantly higher than the one reported by Despont et al. This may be due to the difference in the absorption coefficient of SU-8 at different wavelengths. The absorption coefficient of SU-8 for 365 and 405 nm wavelength radiation is 0.0031 and 0.0005 $(\mu m)^{-1}$, respectively. [70] A higher absorption coefficient for the 365 nm wavelength radiation leads to a lower UV intensity at the bottom of the thick SU-8, and therefore a higher exposure dosage may be required.

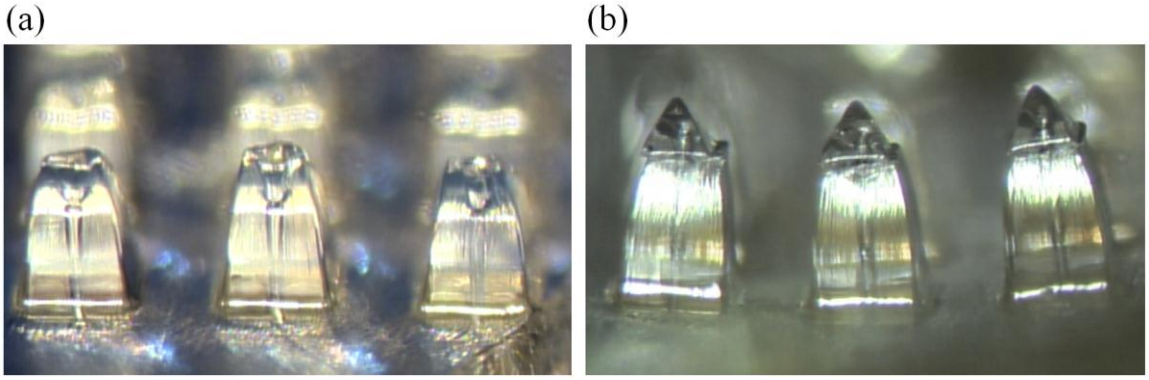

Figure 36. Optical micrographs of the side view of three MNs fabricated with a UV dosage of (a) 2250 mJ/cm^2 and (b) 3000 mJ/cm^2 in the first UV expose shown in Figure 26(c).

3.3.6 Guard Ring Design

Following the SU-8 development shown in Figure 26(e), MN array samples were stored in the cleanroom for further characterization. After overnight storage, it was observed that two opposite edges of the baseplate bent upward and the baseplate curved inward in the middle, as shown in Figure 37. The concave surface of the baseplate may be attributed to a non-uniform degree of SU-8 cross-linking across the baseplate. In the second UV exposure step shown in Figure 26(d), the UV light illuminates the top surface of the SU-8, and, according to the Beer-Lambert law [110], as the light travels into the

SU-8 its intensity decreases. With a reduced UV dosage in the second exposure, the degree of SU-8 cross-linking may decrease as the light travels into the SU-8. A lower degree of SU-8 cross-linking at the bottom portion of the baseplate shown in Figure 26(d) may result in more SU-8 dissolving or more water absorption in the development step [114]. Because of less cross-linked SU-8 or more water evaporation in the subsequent overnight storage, the SU-8 matrix in the bottom portion of the baseplate (Figure 26(d)) collapses or shrinks, and therefore the baseplate curves inward in the middle as shown in Figure 37.

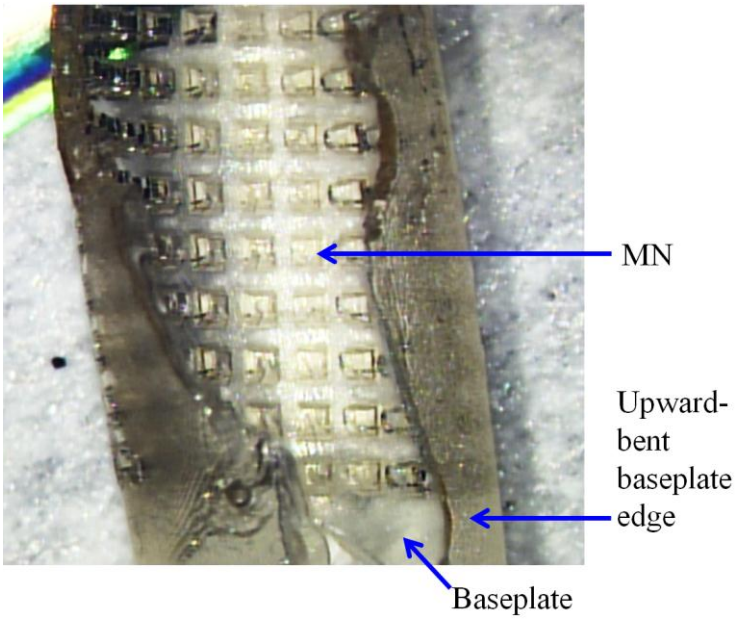

Figure 37. Optical micrograph of the top view of an MN array with a baseplate following the SU-8 development and overnight storage. The right and left edges of the baseplate bent upward.

To prevent the bending of the baseplate, a guard ring on four edges of an MN sample is introduced. Figure 38(a) shows an optical image of an MN sample with a guard ring that locates on the four edges of the sample. The guard ring is defined with a

modified photomask in the first UV exposure step, as shown in Figure 38(b). Following the second UV exposure step and the development step, the final SU-8 structure with a guard ring is depicted in Figure 38(c). As opposed to the baseplate, the guard ring is comprised of highly cross-linked SU-8 (similar to the MNs themselves) and therefore does not deform in subsequent processing and handling, preventing the baseplate from bending. Furthermore, in the subsequent packaging steps, the guard rings can be removed from the MN array samples. For insertion characterization of the MN arrays, such as the one discussed in Subsection 4.4.1, the guard ring was removed from the sample using a razor blade prior to the characterization.

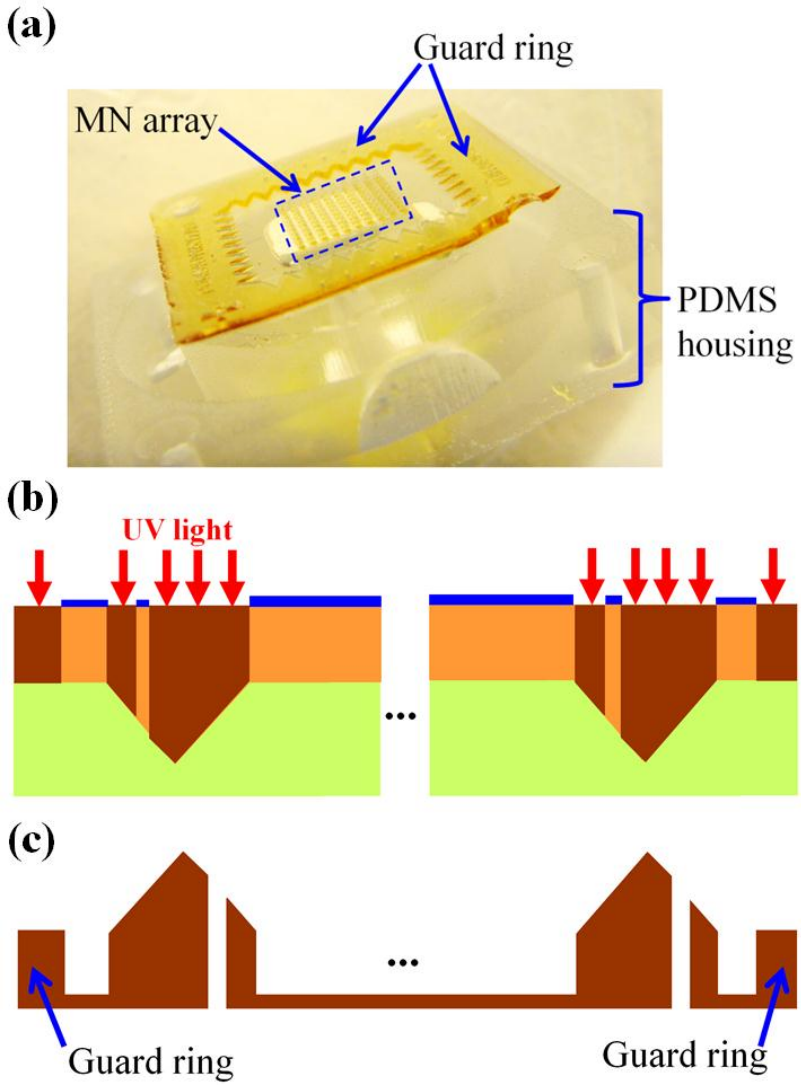

Figure 38. (a) An optical image of an MN array, a baseplate, and a guard ring locating on the four edges of the MN sample. The PDMS housing is for the microfluidic channel test discussed in Subsection 3.4.3. (b) A schematic illustration of the definition of a guard ring in the first UV exposure step shown in Figure 26(c). (c) A depiction of the MN array, baseplate, and guard ring following the development step.

3.4 Microneedle Fabrication

With several fabrication issues associated with UV lithography and the micromolding technique successfully addressed, the fabrication approach using UV lithography into micromolds was utilized to create HMNs with a baseplate.

3.4.1 Fabrication Process of HMNs

The fabrication process of the HMN array consists of two steps. The first step is the construction of an intermediate PDMS mold with pyramidal trenches on the top surface, which define the profile of the MN tip. To construct the intermediate PDMS mold, an inclined UV lithography technique [115, 116] was used to create pyramidal trenches on the top surface of an SU-8 sample. Following the Cr/Au coating of the SU-8 sample, PDMS (Sylgard 184, Dow Corning, Midland, MI) was cast onto the SU-8 sample and cured at room temperature for two days to obtain a positive PDMS master. The positive PDMS master was subsequently coated with Cr/Au, followed by casting of another PDMS onto this master to create a negative PDMS mold. The intermediate PDMS mold was obtained by demolding the negative PDMS mold from the positive PDMS master. Detailed description of the construction of the intermediate PDMS mold was reported in [117, 118]. Moreover, micromolding techniques using PDMS have been reported to replicate nanoscale features (< 0.1 μm). [119]

The second step is the fabrication of the hollow SU-8 MN on the constructed intermediate PDMS mold and is shown in Figure 26. SU-8 2025 (MicroChem Corp., Newton, MA) was first preheated at 60℃ on a hotplate for 30 minutes to improve its encapsulation of the micro-trenches by reducing its viscosity. Oxygen plasma with a RF power of 300 W was used to treat the top surface of the intermediate PDMS mold for 20 minutes, yielding a more hydrophilic surface for better encapsulation of the micro-trenches (Figure 26(a)). The SU-8 was cast by weight to obtain a thickness of 800 μm on the PDMS mold. To remove the bubbles trapped in the PDMS trenches with the integrity of the top surface of the SU-8 intact, a BSV process as shown in Figure 26(b) was

performed for 3 hours. The SU-8/PDMS sample was subsequently softbaked on a level hotplate at 115 ℃ for 24 hours. UV (365 nm i-line) lithography was utilized to define the HMN structure. Two direct UV exposure steps with separate photomasks to define the HMN and the baseplate are shown in Figure 26(c) and Figure 26(d), respectively. In the first exposure (Figure 26(c)), the pyramidal tip and shaft of the HMN were defined using a chromium mask, consisting of a 400×400 μm^2 clear square region for the shaft and a dark circular pattern of 120 μm in diameter for the lumen. The UV dosage was 3000 mJ/cm^2. The first PEB step was subsequently performed with a hotplate at 115 ℃ for 30 minutes. The second exposure with a separate mask and a reduced dosage of 350 mJ/cm^2 defined the baseplate for the HMN array (Figure 26(d)), followed by the second PEB step in an oven at 115 ℃ for 15 minutes to accommodate a certain thickness (100-200 μm) of the baseplate.

Following the demolding of the SU-8 master from the intermediate PDMS mold, the development of the SU-8 master was performed in propylene glycol methyl ether acetate (PGMEA) developer for 6 hours in a static bath and additional 2 hours in an ultrasonic bath (Figure 26(e)). This additional 2-hour development was to remove the unexposed SU-8 in the needle lumens. Following development, the SU-8 sample was rinsed with isopropyl alcohol (IPA) solution and blown dry with a nitrogen gun. After drying, the sample was inspected under an optical microscope. No physical damage to the cross-linked SU-8 was observed after development. Swelling of the SU-8 occurred to a small degree immediately after the development [114], and was reversed after overnight storage in the cleanroom. A completed SU-8 HMN with a baseplate is shown in Figure 26(f).

To enhance the mechanical strength of the SU-8 HMNs, a flood UV exposure step and a hardbake process were performed to fully cross-link and polymerize the SU-8. [120, 121] The UV dosage in the flood exposure is 10 J/cm^2, which is determined based on the extrapolation of suggested UV dosages to 1 mm thick SU-8 using an exponential regression model, as discussed in Subsection 3.3.5. The hardbake process was carried out on a hotplate at 135 ℃ for 30 minutes. Furthermore, the flood exposure may not eliminate the need for the guard ring design discussed in Subsection 3.3.6, since the SU-8 baseplate starts to curl up notably to bare eyes within a few minutes after being removed from the developer. The guard ring design prevents the bending of the SU-8 baseplate and allows the SU-8 sample to dry over time for subsequent processing.

3.4.2 Fabrication Results

A fabricated HMN array is shown in Figure 39. A scanning-electron-microscope (SEM) image of the bird's-eye view of the fabricated needle array is shown in Figure 39(a). The fabricated HMNs are in a 10×10 array at the center of a baseplate chip with a dimension of 25.4 mm × 25.4 mm. Figure 39(b) shows an optical micrograph of an HMN with a baseplate. The height of the HMN is 825 μm, including a 255-μm tall pyramidal tip and a 570-um tall shaft. The base width of the needle is 400 μm. An SEM image of the needle tip with a lumen opening is shown in Figure 39(c). Figure 39(d) shows an SEM image of the tip of an MN in the array. The tip diameter measured using SEM ranges from 15 to 25 μm across the array. The HMN array shown in Figure 39 was fabricated with a non-compensation photomask, and an HMN array fabricated with a compensation photomask is shown and discussed in Subsection 3.3.3.

Examination of the PDMS molds (Figure 26(a)) under an optical microscope

suggests that the four sidewalls of the PDMS trenches converge at a rounded area, instead of an infinitely-small point. Figure 40 shows an optical micrograph of the top view of four PDMS trenches, and the diameter of rounded areas is approximately 25 μm. The rounded geometry at the bottom of the PDMS trenches may result in the finite tip sharpness observed in Figure 39(d). RIE with O_2 and CHF_3 gases has been reported to sharpen tapered SU-8 towers with a top circular mesa of a diameter of ~15 μm, and following the RIE process a tip with a tip diameter of ~5 μm was observed. [51]

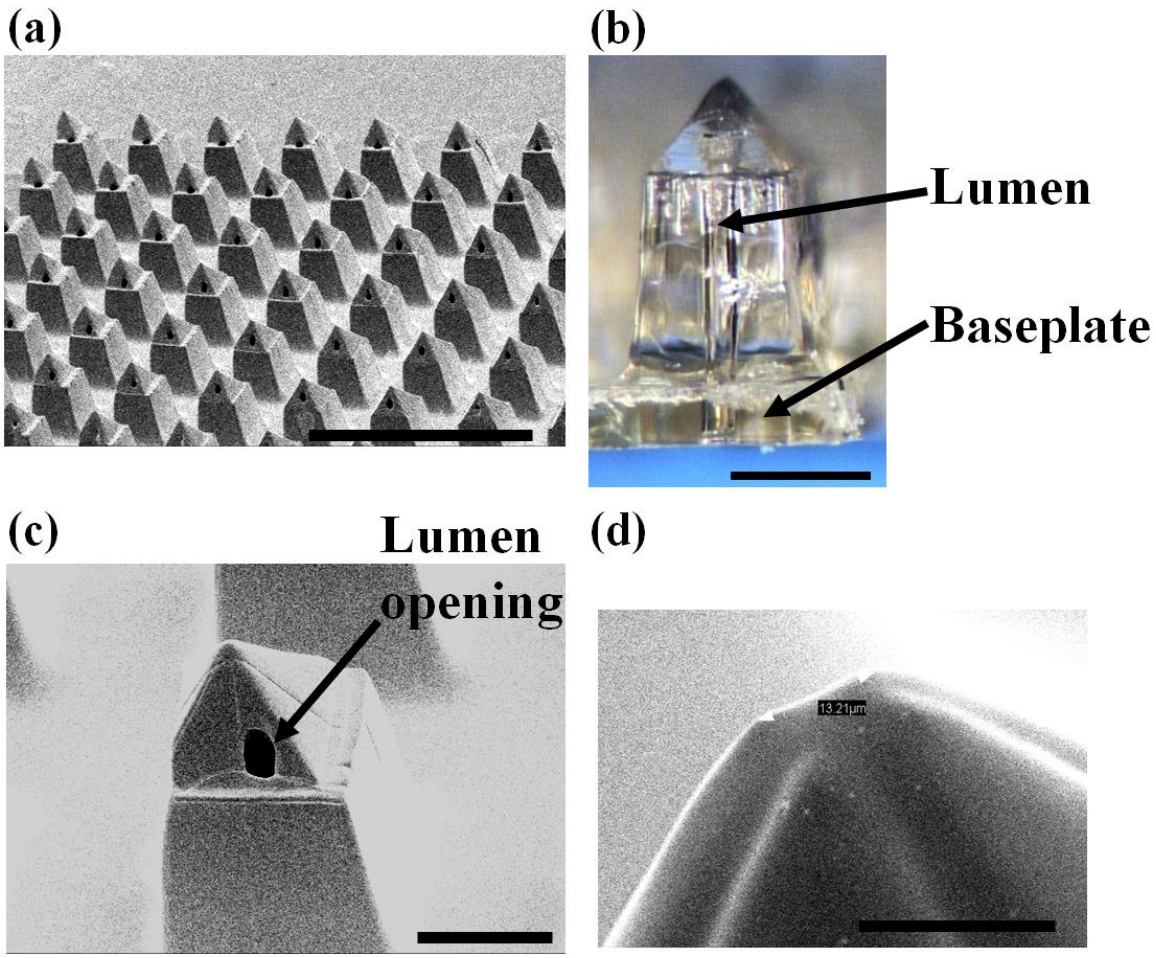

Figure 39. (a) An SEM image of bird's-eye view of fabricated microneedle array coated by 15 nm Cr/150 nm Au for SEM imaging. (b) An optical micrograph showing a fabricated hollow microneedle with a baseplate. (c) An SEM image revealing the pyramidal tip with a lumen opening and upper shaft. (d) An SEM image of the tip of an MN for the measurement of tip sharpness. The tip sharpness of this MN is 13 µm. The scale bar is 2 mm, 400 µm, 250 µm, and 20 µm in (a), (b), (c), and (d), respectively.

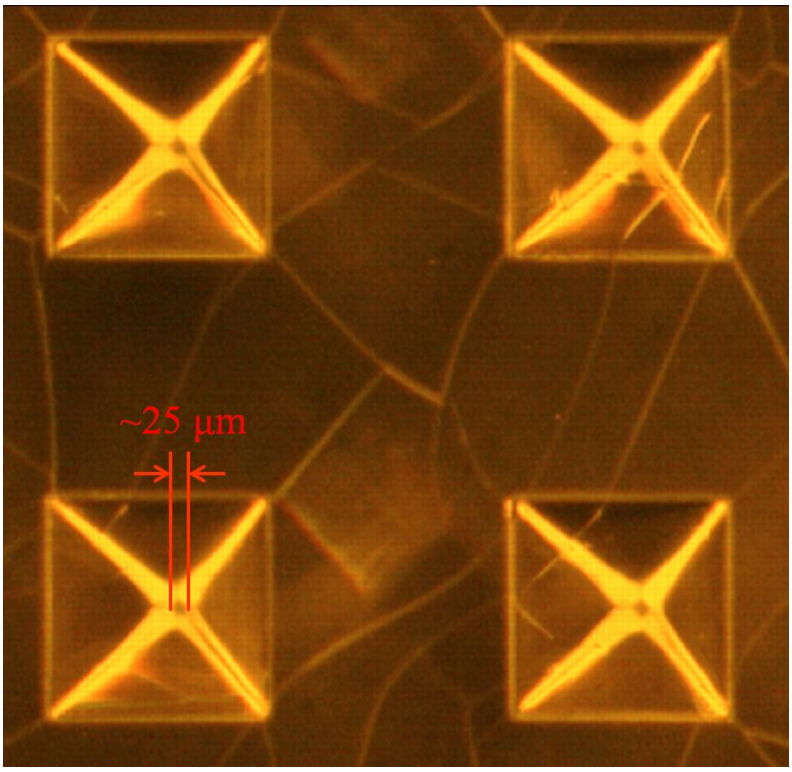

Figure 40. Optical micrograph of the top view of four PDMS trenches. Each pyramidal trench is approximately 400 µm by 400 µm. A rounded area with a diameter of ~25 µm was observed at the bottom of PDMS trenches.

3.4.3 Microfluidic Channel Test

To characterize the microfluidic lumens of the fabricated HMN array, a custom fluidic test setup was used. Figure 41 shows an optical image of the custom fluidic test setup. The test setup consists of a syringe pump system with a dye filled syringe (food coloring with deionized water) and polymer tubing attaching the syringe to the packaged MN array. The testing package consists of a housing with a reservoir, which was attached to the MN array using a layer of PDMS. To examine the development and formation of the HMN lumens, the dye in the syringe was driven by a syringe pump to the backside of the baseplate of a 10×10 needle array and subsequently through any open HMN lumens.

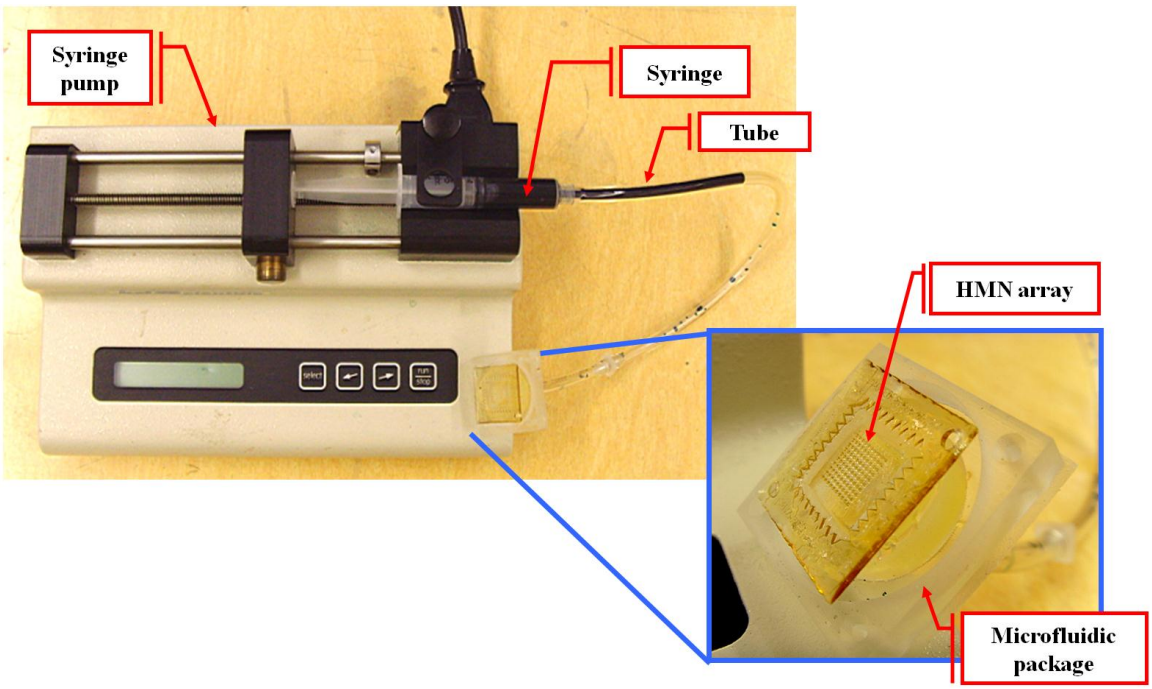

Figure 41. Optical image of the custom fluidic test setup, consisting of a syringe pump, a dye-filled syringe, polymer tubing, a microfluidic package, and an MN sample.

Microfluidic characterization was performed both in tap water and in air. The ejection of the blue dye from the HMN array was observed while the array was either submersed in water or suspended in air as shown in Figure 42(a) and Figure 42(b), respectively. Inspection of the needle tips and the baseplate under an optical microscope during the microfluidic characterization confirmed no crack formation in the baseplate. This alleviates concern that baseplate cracking is the reason for the observed microfluidic flow.

The fluid pressure required to eject water through the needle array was measured with a manometer (Model 220, Netech, Farmingdale, NY) to be less than 655 N/m^2 (0.095 pound per square inch), which is the minimum resolution of the manometer. Since the dimension of the baseplate chip is 0.0256 × 0.0256 m (1.000 × 1.000 inch), the force

required to eject water through the needle array is less than 0.429 N (0.095 pound-force). For comparison, the maximum force produced by a human thumb is 105 N (23.6 pound-force) [122].

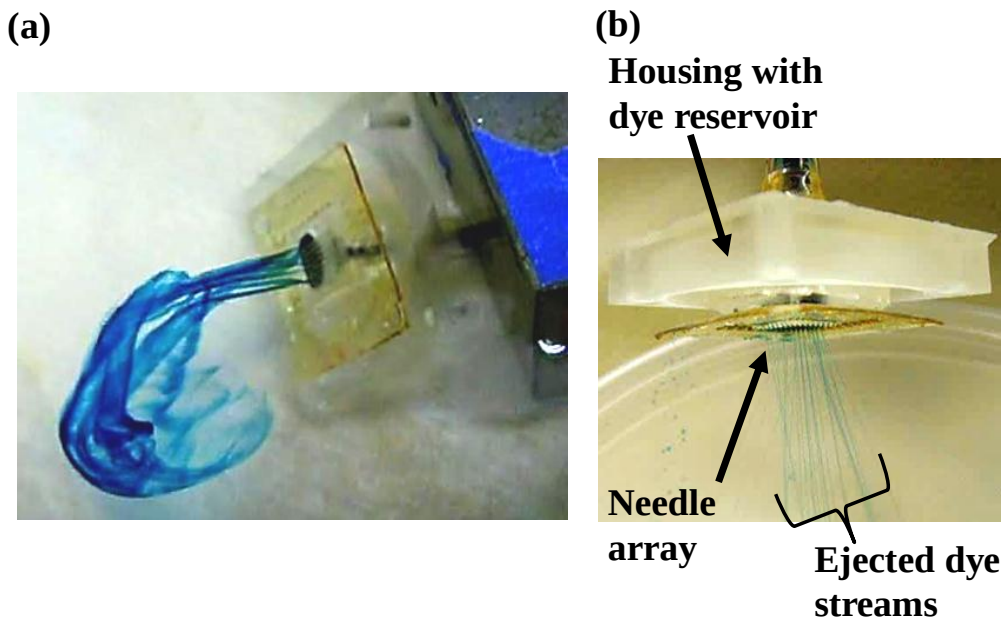

Figure 42. (a) An optical photograph showing the result of microfluidic characterization performed in tap water. Streams of blue dye are being ejected from a microneedle array. (b) An optical photograph illustrating that the blue dye is being emitted from the needle array, while the array is suspended in air with microneedles facing down.

3.4.4 Formation of the Lumens

Visual examination of the fluidic ejection from the array suspended in air indicated that ~20 well-defined lumens were formed as shown in Figure 42(b). The other 80 lumens were occluded by an un-intended SU-8 film near the baseplate opening of the lumen. Given the number of needles in a 10 × 10 needle array, 20 well-defined / open lumens correspond to an open lumen yield of 20 %.

Two other approaches may be performed to determine the number of open lumens in an HMN array. The HMN array can be coated with an opaque metallic film, e.g., 150 nm thick gold on top of 15 nm thick chromium, using a sputterer. The needle array is then placed under a microscope with backside illumination. Inspection of the lumen of each needle under microscope through backside illumination can determine the openness of each lumen, and therefore the number of open lumens in an HMN array can be estimated. Moreover, an HMN array can be attached to a dye reservoir, housing, and a tubing system, as shown in Figure 42(b). The needle array is manually inserted into oil-based modeling clay, and the dye is injected from the dye reservoir into the clay. Following the removal of the needle array from the clay, the clay is inspected under microscope to examine each hole created by insertion of each needle. Whether there is dye inside a hole indicates whether the corresponding lumen is open, and therefore the number of open lumens in an HMN array can be determined. Nevertheless, the latter approach is not feasible when the modeling clay is substituted by agarose gel, since it is observed that the injected dye in agarose gel diffuses rapidly over a large area of agarose gel and therefore it is difficult to determine which lumen the injected dye diffuses from. Figure 43 shows a top view and a cross-sectional view of agarose gel following the insertion of a 10×10 needle array and red dye injection through the needle array. Through approximate 20 open lumens, which were determined in Figure 42(b), the injected dye rapidly stained the entire area of the 10×10 needle array in the agarose gel.

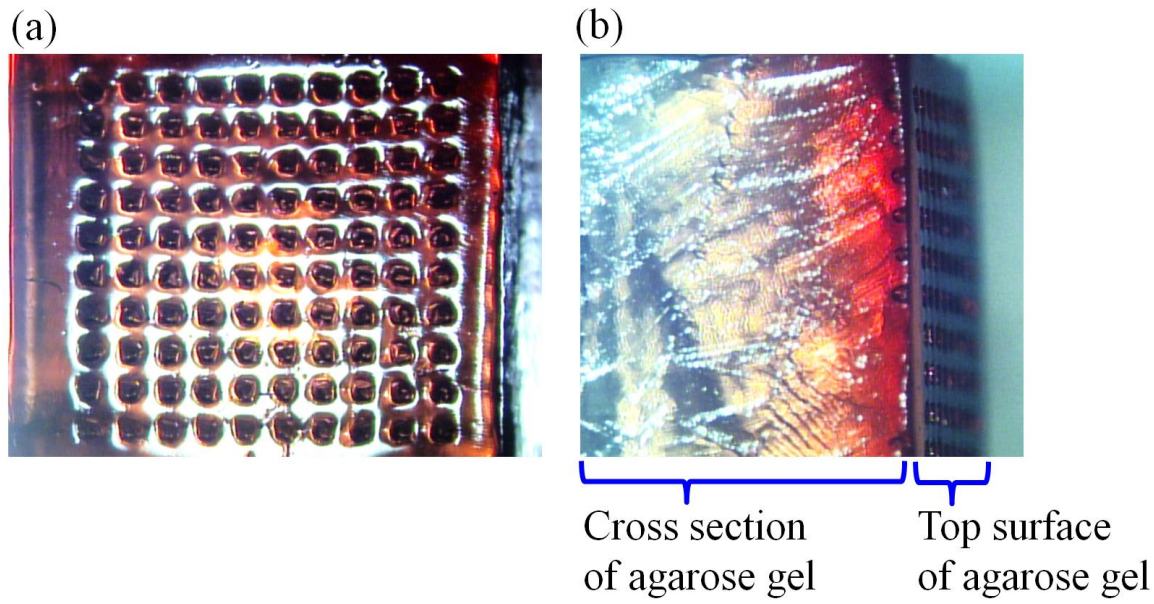

Figure 43. (a) An optical micrograph of the top view of the 10 × 10 needle array area on the agarose gel following insertion and red dye injection through a 10 × 10 needle array. (b) An optical micrograph of the cross-sectional view of the agarose gel.

Figure 44(a) shows a schematic illustration of the location of the un-intended SU-8 film, and Figure 44(b) shows an optical micrograph of the bird's-eye view of the cross section of an un-intended SU-8 film and the bottom part of a lumen. The depth of the observed un-intended SU-8 film into the lumen is approximately the same as the lumen diameter, as shown in Figure 44(b). Given that the lumen diameter is 120 μm, the observed un-intended SU-8 film is located approximately 120 μm from the lumen exit.

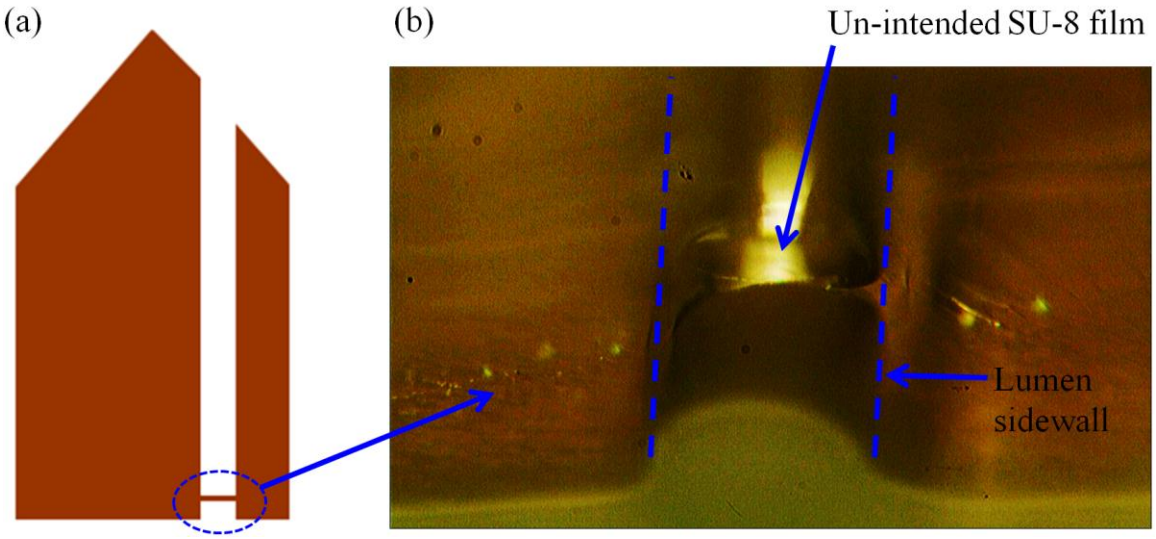

Figure 44. (a) A schematic illustration of the location of an un-intended SU-8 film near the baseplate opening of the lumen. (b) An optical micrograph of the bird's-eye view of the cross section of an un-intended SU-8 film and the bottom part of a lumen.

Yang reported a simulated SU-8 sidewall profile when UV radiation shines through a 20 μm wide slot on a photomask and exposes the 1 mm thick SU-8 underneath the photomask with no gap between the photomask and the SU-8, as shown in Figure 45. [70] Diffraction as UV radiation shines through the aperture on the photomask and the optical absorption of SU-8 were taken into consideration in the simulation of the SU-8 sidewall profile. Because of the symmetry of the sidewall profile, only the right half of the SU-8 region of interest is shown in Figure 45. The SU-8 on the left side of the dashed line represents cross-linked SU-8, and the SU-8 on the right side of the dashed line is un-cross-linked SU-8. At the depth of 0 μm, i.e., SU-8 top surface, the simulated SU-8 sidewall profile does not extend into the SU-8 underneath the opaque part of the photomask, i.e., the unexposed SU-8. As the depth increases, the SU-8 profile extends more into the unexposed SU-8. At a depth of approximately 120 μm, the SU-8 profile

extends the most into the unexposed SU-8. Moreover, a simulated chart of the light intensity distribution at the SU-8 surface as a function of the air gap between the photomask and the SU-8, presented in [70], suggests that as the air gap increases from 0 μm to 100 μm, the UV intensity in the unexposed SU-8 increases and the profile of the UV intensity extends more into the unexposed SU-8. Therefore, a combination of the effects of UV diffraction, optical absorption, and the air gap may result in cross-linked SU-8 extending more into the unexposed SU-8 at the depth of approximately 120 μm. A potential joint of the two extensions of cross-linked SU-8 from the two sides of the opaque part of the photomask may lead to a lumen occlusion, suggesting a possible cause of the observed un-intended SU-8 film shown in Figure 44(b).

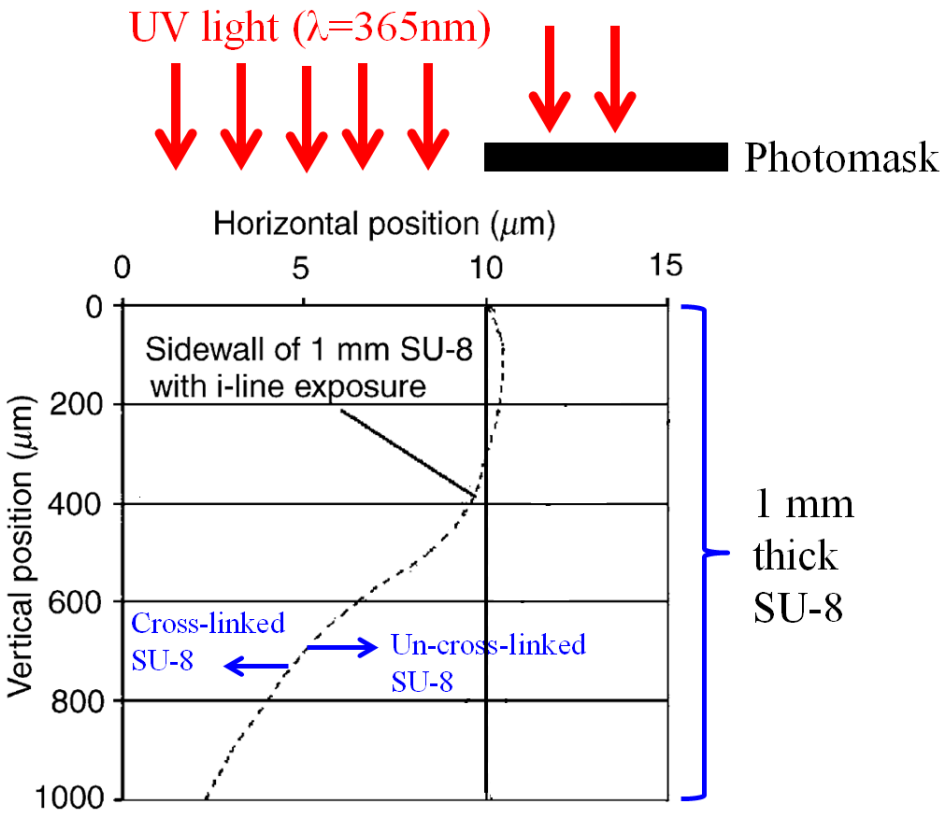

Figure 45. A simulated SU-8 sidewall profile when UV radiation exposes 1 mm thick SU-8 through a 20 μm wide slot on a photomask with no gap between the photomask and SU-8. Because of the symmetry of the sidewall profile, only the right half of the exposed region is shown. The SU-8 on the left side of the dashed line is cross-linked SU-8, and the SU-8 on the right side is un-cross-linked SU-8. [70]

To remove the SU-8 films, the backside of the baseplate was treated with RIE for 30 minutes. The RIE was performed with SF_6 gas (10 cm^3/min) and O_2 gas (100 cm^3/min). The RF power of the RIE is 200 watts, and the processing pressure is 400 mTorr. Figure 46(a) and Figure 46(b) show an optical micrograph of the side view of the bottom part of a lumen where an un-intended SU-8 film was located prior to and following the RIE treatment, respectively. Prior to the RIE treatment, an SU-8 film was observed inside the bottom part of the lumen, as shown in Figure 46(a). Following the RIE treatment, no SU-8 film was observed (Figure 46(b)).

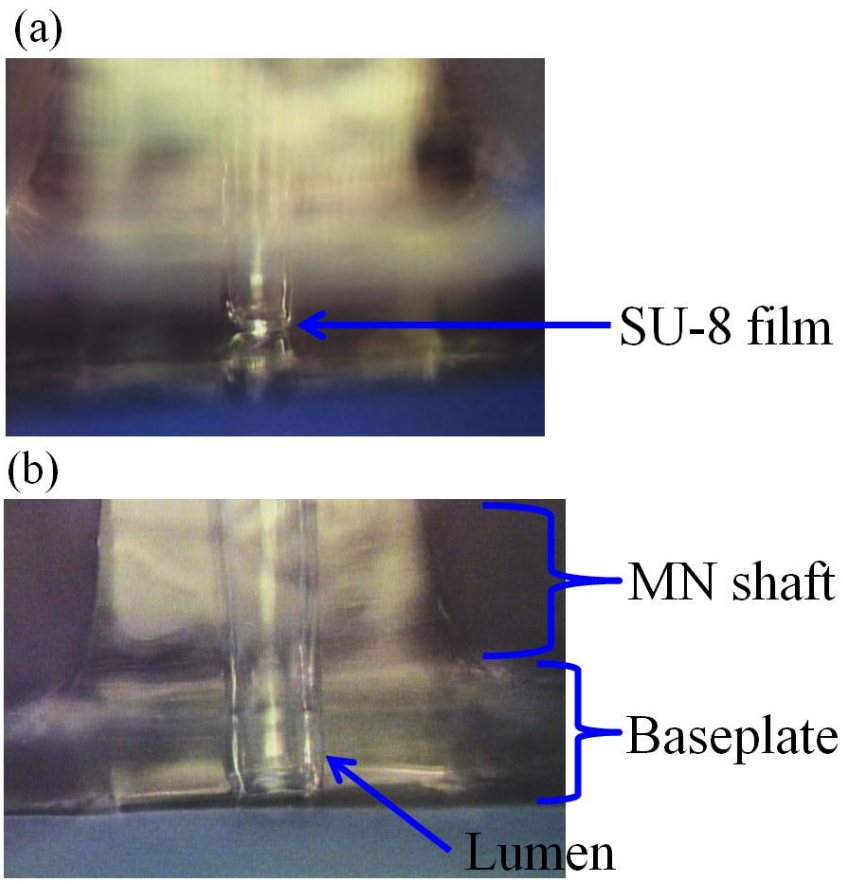

Figure 46. (a) An optical micrograph of the side view of an un-intended SU-8 film, a lumen, the bottom part of an MN shaft, and a baseplate prior to the SF_6 plasma treatment. The MN and the baseplate were not processed for imaging, and the focus of the image was set to the SU-8 film inside the lumen. (b) An optical micrograph of the same MN and baseplate following the SF_6 plasma treatment. No SU-8 film was observed inside the lumen.

In addition to the un-intended SU-8 films, some lumens were not well-defined in the pyramidal tips of the MNs. Figure 47 shows an optical micrograph of the bird's-eye view of two MNs in an MN array. The lumen of the MN on the right is well-defined in the MN shaft and in the pyramidal tip of the MN, where a lumen opening locates on one of the four slopes. In the MN on the left, the lumen is defined in the shaft and not defined in the pyramidal tip, resulting in a lumen occlusion inside the MN tip. With the SU-8

softbake temperature lowered from 115 ℃ to 95 ℃, it was confirmed with two MN samples that the number of lumen occlusions at the needle tip was significantly reduced in the MN arrays, suggesting that an excess thermal budget in the needle tip may result in local SU-8 polymerization without UV radiation and therefore inhibit SU-8 dissolving in the development step.

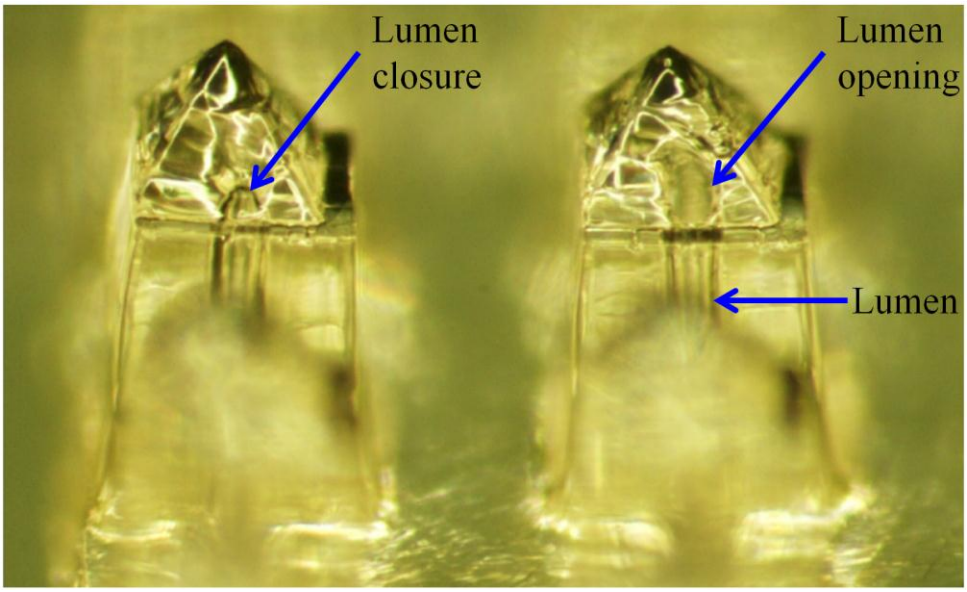

Figure 47. An optical micrograph of the bird's-eye view of two MNs in an MN array. The lumen of the MN on the right is well-defined with a lumen opening on a slope of the pyramidal tip of the MN. The lumen of the MN on the left occludes inside the pyramidal tip.

Compared to the MNs, presented in this chapter, with a lumen openness yield of ~20%, the MNs, discussed in Chapter. 4, with a different geometry and processing parameters exhibit a lumen openness yield of at least 85%. The major differences between these two MNs include (1) the lumen diameter was increased from 120 μm to 150 μm, and (2) the SU-8 softbake condition was changed from 115 ℃ for 24 hours to 85 ℃ for 16 hours.

3.5 Characterization of Microneedles

3.5.1 Performance Metrics of Microneedles

The primary functions of HNs are insertion into skin without fracture and subsequent fluid injection into skin. Therefore, following the construction of microneedles and the verification of open lumens, skin penetrability, mechanical fracture strength, and capability of fluid injection into skin were characterized using fabricated MNs and used as performance metrics for MNs. Skin penetrability of MNs was characterized using excised porcine skin as a substrate to determine the required driving force for MNs to insert into skin. Mechanical fracture strength of MNs was characterized by an automatic force-displacement test station using excised porcine skin and/or a rigid surface as a substrate to estimate the fracture force of MNs. Capability of fluid injection into skin was performed manually with a custom fluid injection system to gain an understanding of the fluid injection capability of MNs.

Insertion of MNs with a length up to 960 μm or a width up to 465 μm into the skin of human subjects has been reported to exhibit 30% or lower pain scores compared to a 26-gauge (26G) hypodermic needle (HN) on a visual analog scale (VAS). [91] Moreover, for infusion of saline up to 1.0 mL using MNs measuring up to 1,000 μm in length, 60% or lower pain scores have been reported in comparison to a 26G HN on the VAS. [123] Therefore, MNs of up to one millimeter in height have been shown to exhibit less pain than a 26G HN for insertion and infusion of fluid into skin.

3.5.2 Preparation of Individual Microneedles

Characterization of HMNs was performed on individual single needles for simplicity. All HMNs were flood exposed with UV light and hardbaked as described in

Subsection 3.4.1. After the hardbake process, 15 nm of chromium and 150 nm of gold were sputtered onto the surface of MNs and the baseplate to create a conductive path between the tip of the MN and the perimeter of the baseplate. An individual needle with surrounding baseplate was then cut out of the needle array with a razor blade and placed on the bottom surface of a flat-head steel machine screw. Silver paint (Pelco® Conductive Silver 187, Ted Pella Inc., Redding, CA) was dispensed to create a conductive path from a portion of the baseplate perimeter to the machine screw, completing the conductive path between the tip of the needle and the steel machine screw. This conductive path is required for the measurement of the insertion force, which is discussed in Subsection 3.5.4. The flat head of the machine screw was then affixed to the center of the plate of an aluminum SEM specimen mount for ease of handling. A copper wire was used to electrically connect the machine screw to the ohmmeter of a force-displacement apparatus for the measurement of the insertion force. Figure 48(a) shows an optical image of a custom single-MN insertion system, including an MN, a steel machine screw, and an SEM specimen mount as well as the silver paint and copper wire used for skin resistance measurement. Figure 48(b) shows an optical micrograph of the single MN with its surrounding baseplate and the machine screw as well as the silver paint that provides a conductive path between the top surface of the baseplate and the machine screw.

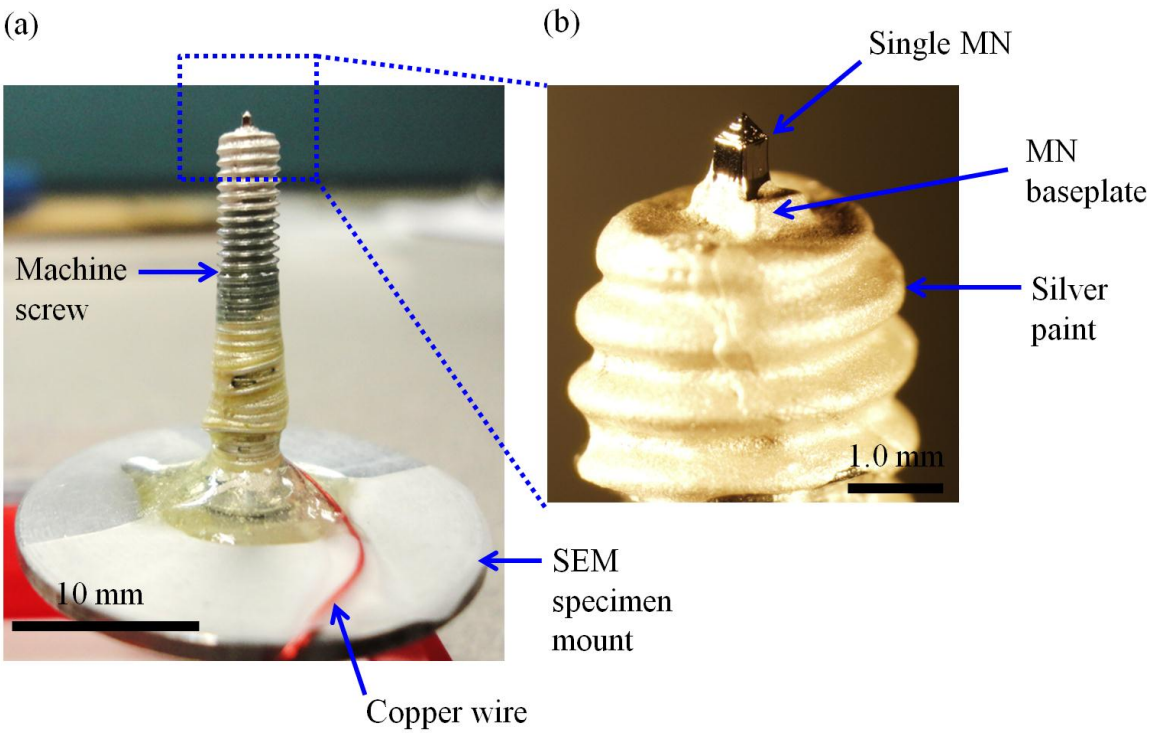

Figure 48. (a) An optical image of a custom single-MN insertion system, including an MN, a steal machine screw, and an SEM specimen mount. Silver paint and a copper wire are used to complete an electrical conduction path for skin resistance measurement. (b) An optical micrograph of the MN with its surrounding baseplate and the machine screw as well as the silver paint.

3.5.3 Mechanical Characterization of Microneedle

Microneedles are commonly inserted into skin in a way that the needle shaft is perpendicular to the surface of the skin. Therefore, the skin exerts axial compressive force on the MN. To understand the mechanical response of an MN under axial compressive stress, a uniaxial compressive test was performed with individual MNs.

A force-displacement test station (Model 921A, Tricor Systems Inc., Elgin, IL) was used to perform the uniaxial compressive test. In the test, the load cell of the test station drives an aluminum plate toward the MN and the surface of the plate is perpendicular to the shaft of the needle. The MN is held stationary. The load cell measures the force at the aluminum plate/needle interface and records the displacement

of the plate. A 100× microscope camera was used to record the video of the test. The aluminum plate was driven at a rate of 0.025 mm/sec for video recording. An optical image of the experimental setup of the uniaxial compressive test is shown in Figure 49. The load cell is housed inside the load cell system and therefore not visible in Figure 49. For better imaging of the 100× microscope camera, a black screen was placed behind the custom single-MN insertion system.

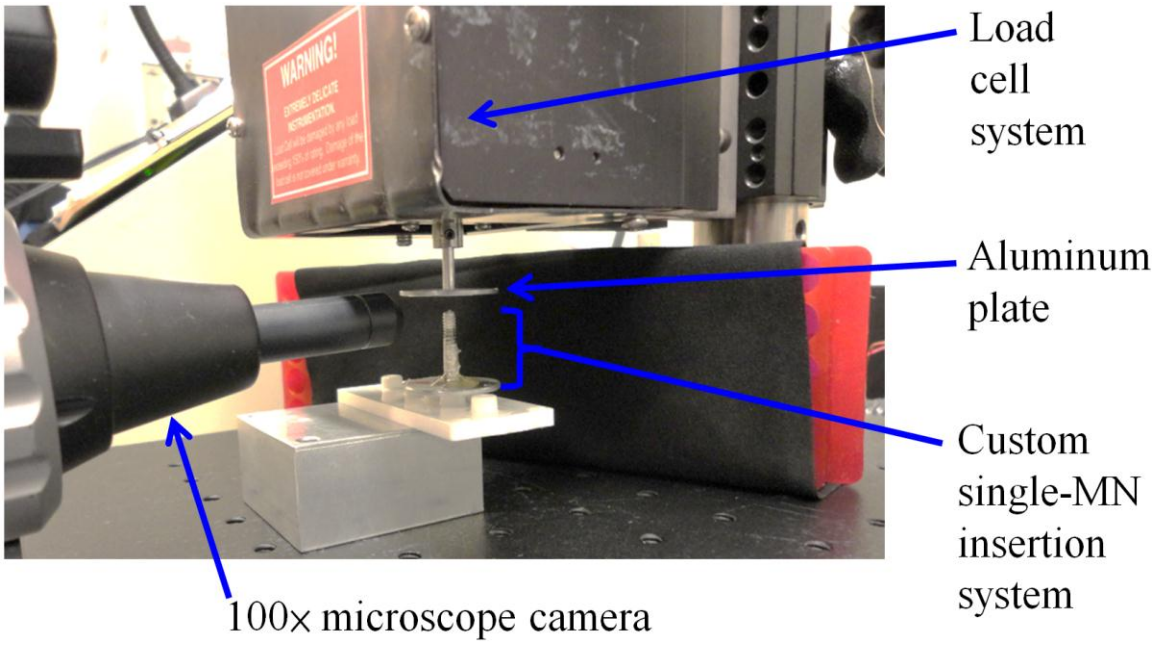

Figure 49. An optical image of the experimental setup of the uniaxial compressive test of a fabricated MN.

A representative force-displacement chart of the uniaxial compressive test for a single MN is shown in Figure 50. The displacement of zero represents the initial contact between the aluminum plate and the MN tip. In Figure 50, the force initially increases with the displacement and reaches the first peak at a displacement of 220 μm and decreases until reaching 250 μm displacement.

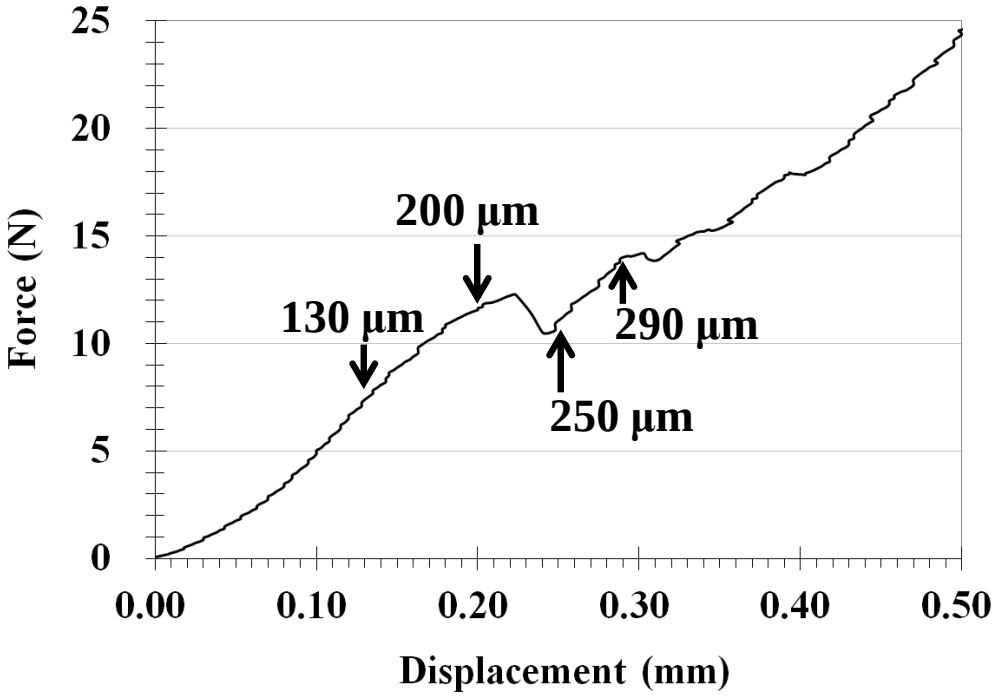

Figure 50. A representative force-displacement chart in the uniaxial compressive test of a microneedle. The zero displacement represents the initial contact between the needle tip and the aluminum plate. The reaction force initially increases with the displacement and reaches the first peak value at a displacement of 220 µm and decreases until reaching 250 µm displacement.

Four optical micrographs shown in Figure 51(a)-(d) were taken at a displacement of 130, 200, 250, and 290 µm, respectively, to assess the integrity of the needle. Figure 51(a) and Figure 51(d) were taken with an optical microscope after the test was stopped at a displacement of 130 and 290 µm, respectively. Figure 51(b) and Figure 51(c) were captured from the video clip taken with the 100X microscope camera during the test at a displacement of 200 and 250 µm, respectively.

Since Figure 51(a) was taken when the external force from the aluminum plate was removed, the deformed tip of the MN suggests that the tip underwent plastic deformation as the force initially increased with the displacement. No crack at the needle

tip was observed under an optical microscope at a displacement of 130 and 200 μm, as shown in Figure 51(a) and Figure 51(b), respectively.

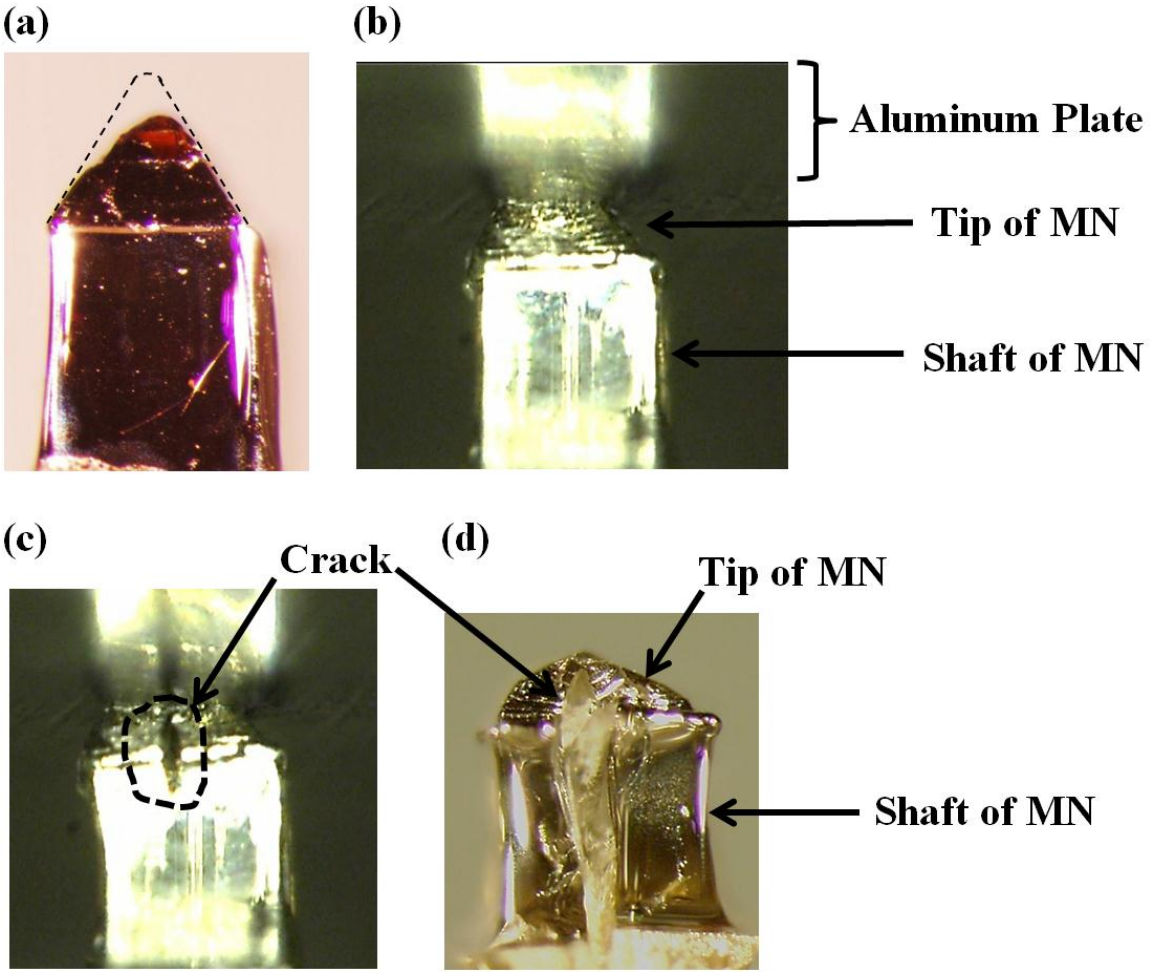

Figure 51. Optical micrographs showing the side view of a microneedle at the four indicated points of Figure 50 during the uniaxial compressive test. (a) An image of a needle taken after the test is stopped at a displacement of 130 μm. The dotted line represents the tip profile prior to the test. (b) An image of the aluminum plate and a needle captured from a video clip of the test. The displacement is 200 μm. (c) Another image captured from the same video clip. The displacement is 250 μm. A crack is observed at the needle tip. (d) An image of a needle taken after the test is stopped at a displacement of 290 μm. A large crack is observed and results in the splitting of the needle tip and shaft structures.

After the force reached the first peak at a displacement of 220 μm, a crack at the needle tip was observed in Figure 51(c) at a displacement of 250 μm, and Figure 51(d)

shows a larger crack along the needle tip and shaft structures, causing the splitting of the needle. Therefore, the observation in Figure 51 suggests that the cracking/fracture of the needle tip occurred between displacements of 200 and 250 μm. Since a decrease in force implies a failure in the structural integrity of the needle, the force at the first force peak is defined as the fracture force of the needle, at which the fracture of the needle tip occurs. The fracture force is 12.2 N in Figure 50.

Figure 52 shows a chart of the fracture force measured from five individual MNs in the uniaxial compressive test. The mean of the fracture force of these five MNs is 12.0 N with a standard deviation of 0.8 N.

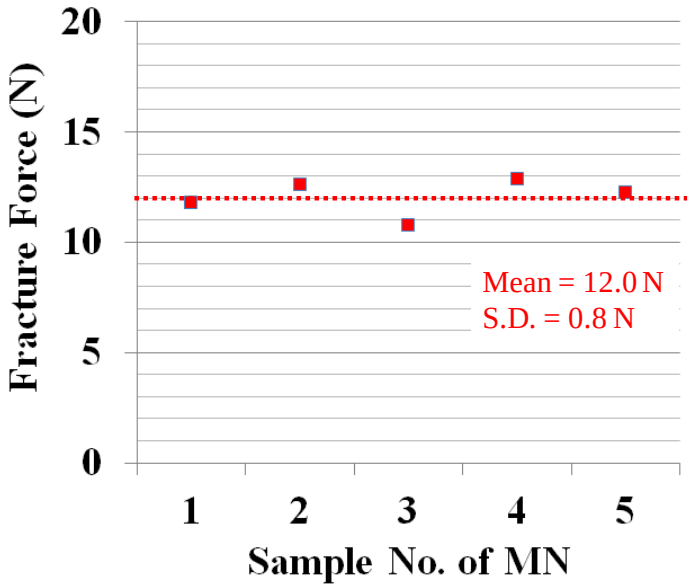

Figure 52. A chart showing the fracture force of five individual microneedles measured in the uniaxial compressive test. The mean value of the fracture force is 12.0 N with a standard deviation of 0.8 N.

Microscope observation of the five MNs in the uniaxial compressive test indicates that during the test a crack initially occurs at the needle tip and develops along the tip and

shaft structures of the needle, leading to a vertical splitting of the needle. The failure mode of this vertical splitting of a structure under a uniaxial compressive test is similar to a failure mode called “axial splitting.” [124] Axial splitting is a common failure mode for unconfined brittle materials under a uniaxial compressive test. The stress-strain curve of SU-8 indicates that SU-8 changes gradually from a ductile material to a brittle material in the thermal processing of SU-8 and hardbaked SU-8 is a brittle material. [108, 125] Ductile materials exhibit a significant amount of plastic deformation prior to fracture, however some brittle materials may show a certain amount of plastic deformation. [126]

The Griffith failure criterion states that for brittle materials under a uniaxial compressive test, the normal compressive stress when the fracture occurs is eight times the tensile strength of the material. [127] The tensile strength of SU-8 after a 30-minute hardbake reported in the literature is 42.1 MPa. [108] Therefore, based on the Griffith failure criterion and the tensile strength of SU-8, the theoretical value of the critical stress, i.e., the normal compressive stress when the fracture occurs, is calculated as 336.8 MPa.

The empirical value of the critical stress can be calculated from the force measurement and the displacement data in the uniaxial compressive test for the five individual MNs. Assuming that the angle of the needle tip is 70 ° as defined by the PDMS mold and that the contact area between the aluminum plate and the needle tip is square when the fracture of the tip occurs, the area of the contact region can be calculated from the displacement data in the test. Therefore, the empirical value of the critical stress can be obtained by dividing the force over the area of the contact region and is shown in Figure 53 for the five individual MNs in the test. The mean value of the empirical critical stress of these five needles is 290.7 MPa, and the standard deviation is 69.2 MPa.

One-sample Student's t-test [128] was employed to test the null hypothesis that the mean of the empirical critical stress of these five MNs is equal to the theoretical estimation, and the t-test was performed with the MINITAB software (Minitab Inc., State College, PA). With the calculated p-value greater than 0.05, it suggests that the mean of the empirical critical stress is not significantly different from the theoretical value.

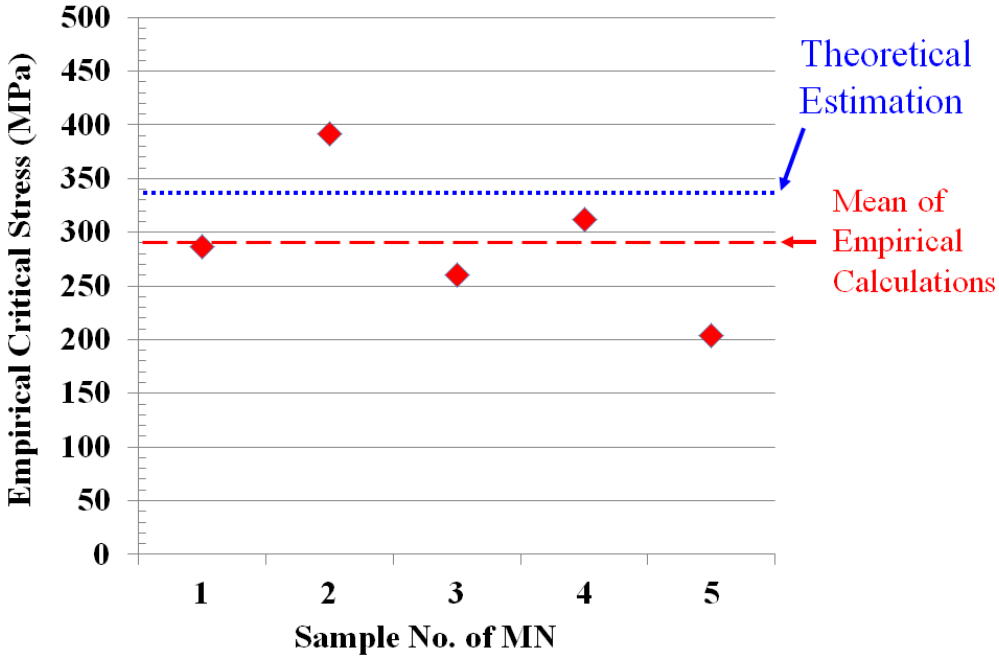

Figure 53. A chart of the empirical critical stress for the five individual microneedles in the uniaxial compressive test. The mean value of these five critical stresses is 290.7 MPa, and the standard deviation is 69.2 MPa. The theoretical estimation of the critical stress (336.8 MPa) is shown for comparison.

3.5.4 Biological Insertion Characterization of Microneedle

To characterize the insertion performance of the fabricated HMNs into skin as well as to understand the subsequent mechanical interaction between the MN and skin, three investigations were conducted using excised porcine skin. The required driving

force for a single MN to successfully insert into skin, i.e. insertion force, was first measured. Following the insertion into skin, the driving force that results in blunting the needle tip was estimated. Furthermore, the minimum driving force onto an MN causing tip fracture, i.e. fracture force, was assessed.

For practical applications, the relation between the insertion force and fracture force is of importance for assessing the insertion performance of MNs. [1] When the fracture force is larger than the insertion force, it indicates that the needle inserts successfully into skin without tip fracture. Nevertheless, if the fracture force is larger than the insertion force by a small amount, then applying force that is considerably higher than the insertion force may cause needle fracture, leaving needle fragments in the skin. Therefore, it is desired that the fracture force is significantly higher than the insertion force to reduce the possibility of needle fracture following successful insertion into skin and therefore to potentially enhance needle safety. To quantify this concept, an index, namely the margin of safety, is commonly used for MNs and is defined as the ratio of the fracture force to the insertion force. [1, 129, 130]

Preparation of Excised Porcine Skin

The skin penetrability of the fabricated MNs was evaluated with excised porcine skin. The excised porcine skin (Pel-Freez, Rogers, AR) was shaved using a razor and the subcutaneous fat on the back of the skin was subsequently removed with a scalpel. The prepared skin was affixed under mild tension to a wooden block using screws. Individual MNs were used to characterize the insertion performance of the needle into skin. Figure 54 shows an optical image of the top view of a piece of excised porcine skin affixed to a wooden block using screws.

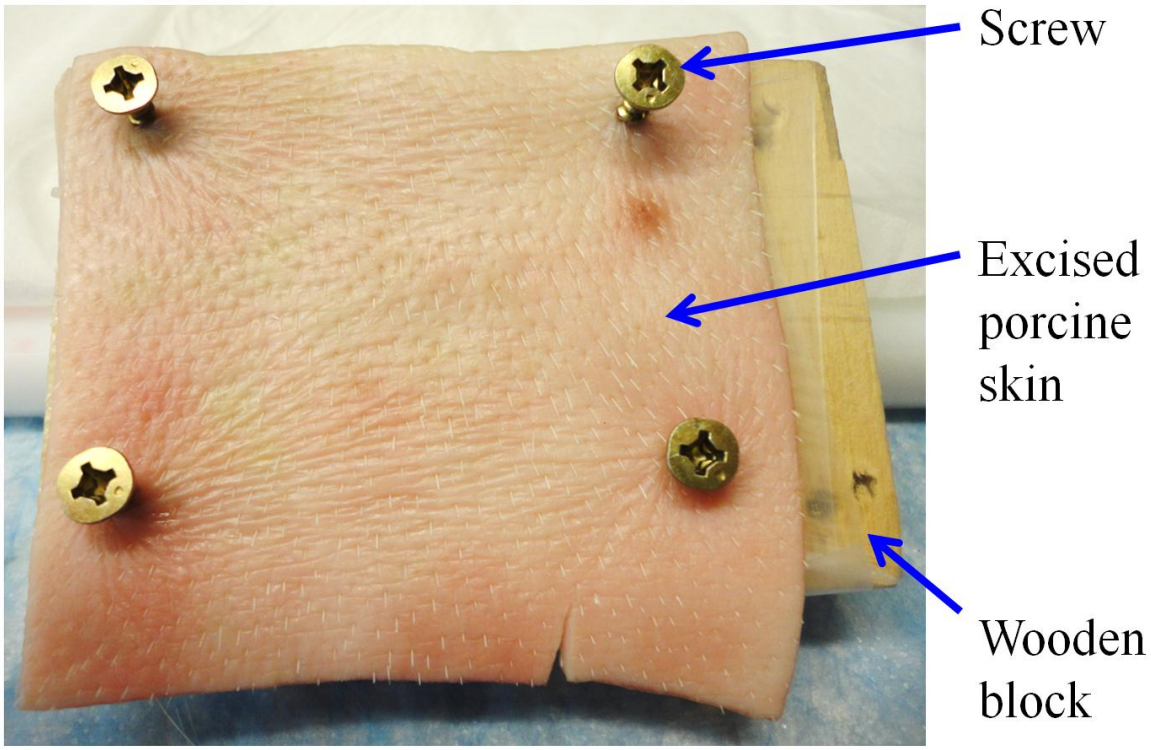

Figure 54. An optical image of the top view of a piece of excised porcine skin, which has been shaved. The skin was affixed to a wooden block using four screws.

Insertion Force Measurement of Single Microneedle

To measure the insertion force, the needle was pressed perpendicularly against the porcine skin at a rate of 1.0 mm/sec by the force-displacement test station described in Subsection 3.5.3, followed by separation of the needle from the skin.

During the process of pressing the needle against the porcine skin, the occurrence of the rupture of the SC, by which successful insertion is defined, can be detected by observing discontinuous changes in the skin resistance. [129] Figure 55 shows a schematic diagram of the measurement setup of the skin resistance as well as the

measurement of the reaction force and needle displacement. The skin resistance, as shown in Figure 55, consists of the resistances from the highly-resistive SC and the resistive VE, and therefore an abrupt decrease in the skin resistance can serve as an electrical indication of the rupture of the SC. The load cell of the test station presses the needle perpendicularly against the porcine skin and measures the reaction force from the needle. The force and displacement data are recorded by the computer of the test station, and simultaneously the ohmmeter measures the skin resistance and sends the data to the computer for recording. A representative chart of the skin resistance and the reaction force plotted as a function of the needle displacement is shown in Figure 56. The abrupt decrease of the skin resistance at a displacement of 535 μm indicates the rupture of the SC. Therefore, the corresponding force of 1.5 N at a displacement of 535 μm is taken as the insertion force.

In the measurement of the insertion force, seven individual MNs were tested, and each needle was inserted into porcine skin an average of two times, yielding 15 data points for the estimation of the insertion force. Figure 57 shows the measured insertion force plotted against the sample number of each MN. The mean of the measured insertion force is 2.4 N with a standard deviation of 1.2 N.

Following the separation of the needle from the skin, one drop of blue dye was dispensed onto the skin surface. The dye flowed through the MN-defined pathway in the SC and stained the VE underneath. Stain in the VE serves as a physical indication of successful insertion of the MN into skin. The skin surface was then wiped with alcohol swabs to remove the residual dye on the skin, followed by inspection of the skin under an optical microscope. An optical micrograph of the top view of an insertion site is shown in

Figure 58. The inner red dotted line marks the opening in the SC created by the successful insertion of the MN into the porcine skin. The outer black dashed line outlines the underneath VE region that is stained by the dye.

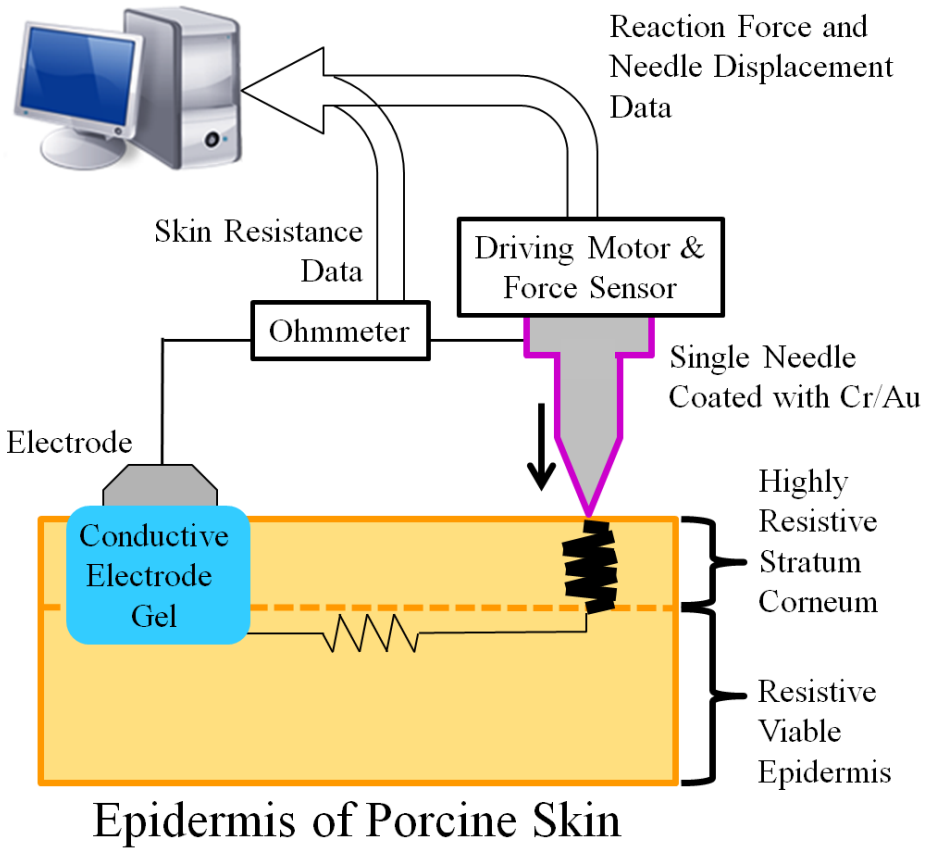

Figure 55. A schematic diagram of the measurement setup of the insertion force for a microneedle. The SU-8 needle and baseplate are coated with a chromium/gold layer to complete the electrical circuit for the resistance measurement of the skin, which includes the highly-resistive stratum corneum and the resistive viable epidermis. During the insertion test, the data of the skin resistance is recorded in the computer of the test station simultaneously with the data of reaction force and needle displacement.

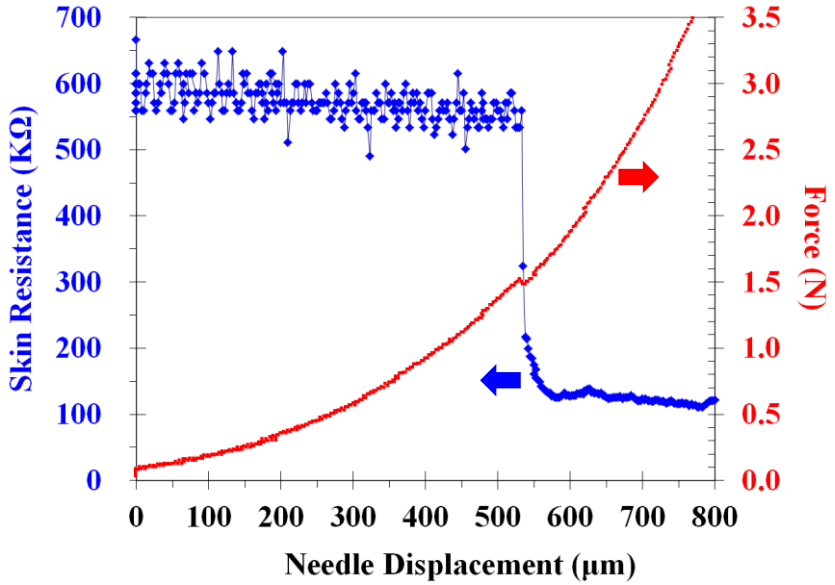

Figure 56. A representative chart of the skin resistance and the reaction force plotted as a function of the needle displacement. The insertion force is defined as the corresponding force of 1.5 N at a displacement of 535 μm where the abrupt decrease of the skin resistance serves as an electrical indication of the rupture of the stratum corneum.

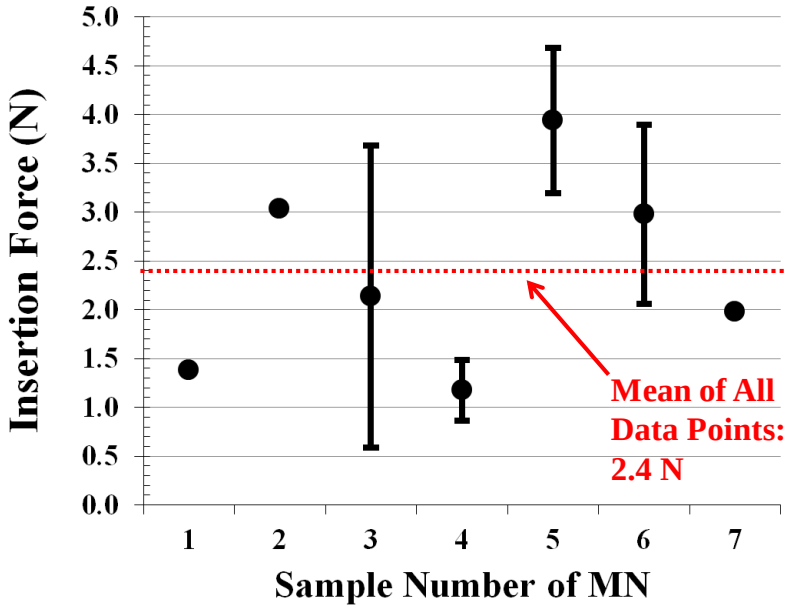

Figure 57. A chart of the measured insertion force plotted against the sample number of microneedles. Seven individual MNs are tested. Microneedles with the sample number 1, 2, and 7 are tested one time, and needles with the number 3, 4, 5, and 6 are tested multiple times up to four times. The circle for each MN represents the mean of the measured insertion force with the MN, and the upper and lower whiskers are the standard deviations. There are 15 insertion tests in total performed with these 7 needles, and the mean of these measured insertion force is 2.4 N with a standard deviation of 1.2 N.

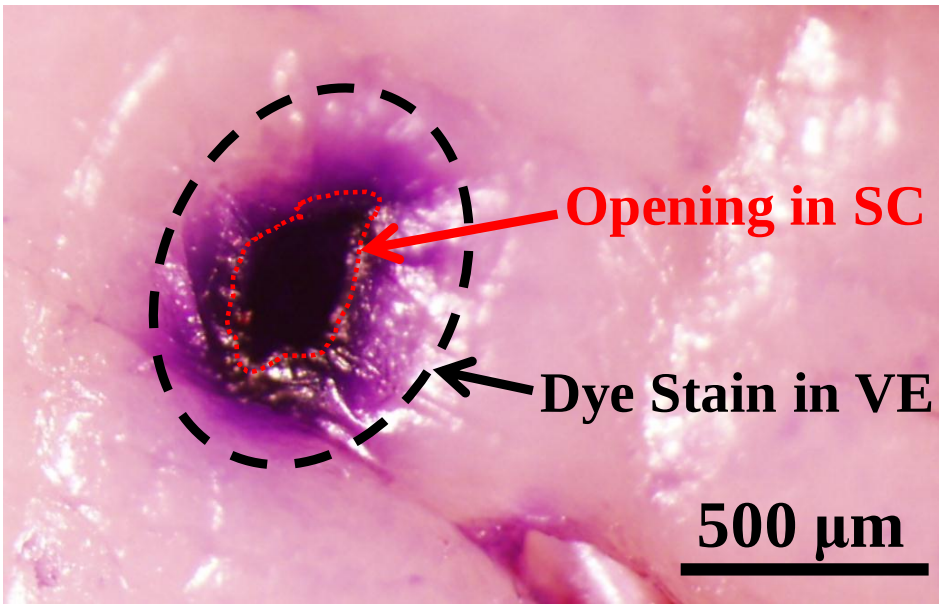

Figure 58. An optical micrograph of the top view of an insertion site on the porcine skin following the insertion of the microneedle and the dye staining. The opening in the stratum corneum (SC) is caused by the successful insertion of the needle, followed by the dye flowing through the opening and staining the viable epidermis (VE) underneath.

Tip-Blunting Force Estimation

Observations in Figure 51 discussed in Subsection 3.5.3 indicate that under external stress the tip of the MN deforms plastically prior to the tip fracture, suggesting that the needle tip deforms gradually and loses its initial sharpness when being pressed against the porcine skin and prior to the successful insertion into skin. This gradual deformation of the needle tip blunts the tip.

Therefore, it is of importance to evaluate the tip-blunting force, which is defined as the external force being applied to an MN that makes the MN tip so blunt that successful insertion into skin cannot be made with the same external force. It is desirable that the tip-blunting force of the needle is significantly larger than the insertion force so that the MN inserts successfully into skin prior to being blunt that prevents successful insertion.

To estimate the tip-blunting force, an MN was pressed perpendicularly against the porcine skin at a rate of 1.0 mm/sec by a force-displacement test station, Bose ElectroForce 3200 Test Instrument (Bose Co., Eden Prairie, MN), followed by separation of the needle from the skin. Figure 59 shows an optical image of the experiment setup for the estimation of the tip-blunting force of a single MN using a Bose ElectroForce 3200 Test Instrument. The MN was affixed to the bottom of the machine screw. The excised porcine skin was mounted to a wooden block placed on top of an aluminum block. The aluminum block was supported by the load cell of this test instrument. The maximum driving force was set to be 50 N for each test. The 50 N force was chosen such that this force is approximately one order of magnitude higher than the maximum measured insertion force from the 15 insertion tests in Figure 57, which is ~4.5N. A skin staining test was then performed to verify the successful insertion of the needle into skin.

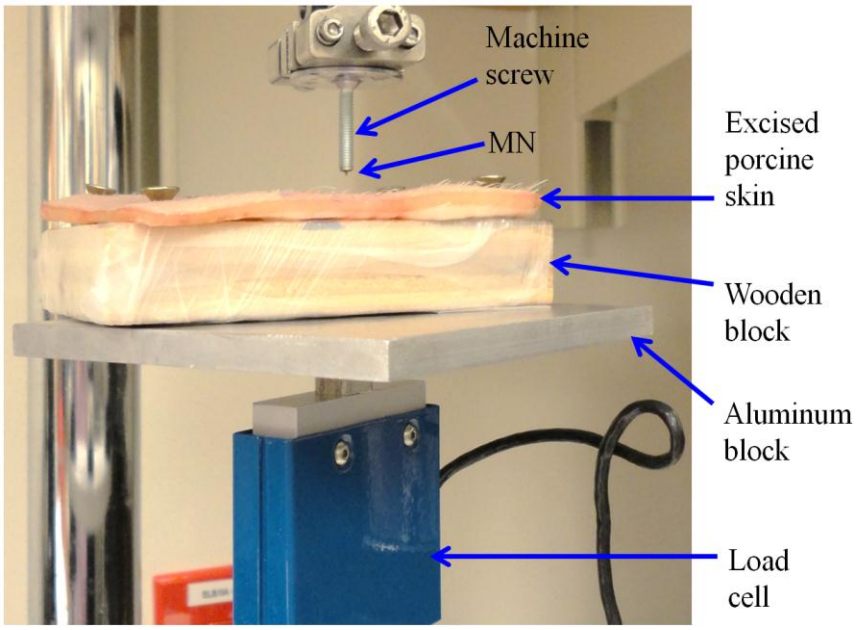

Figure 59. Optical image of the experiment setup for the tip-blunting force estimation of an MN using Bose ElectroForce 3200 Test Instrument.

Three individual MNs were tested, and each needle was pressed against the porcine skin with the maximum driving force of 50 N in the initial insertion test and the following three re-insertion tests. After all four insertion tests, each needle tip was examined under an optical microscope. The skin staining results for each insertion test are shown in Table 2. With the maximum force of 50 N being applied to an MN in the initial insertion test as well as the first and second re-insertion tests, each of the three tested MNs remained capable of inserting successfully into porcine skin in the third re-insertion test. In addition, no significant tip deformation or fracture was observed under an optical microscope for all three MNs after four insertion tests. These insertion tests indicate that for insertion into porcine skin the driving force that results in blunting the needle tip, i.e., the tip-blunting force, is larger than 50 N. Moreover, the 50 N force is one-order-of-magnitude higher than the maximum measured insertion force for porcine skin.

Table 2. Skin Staining Result in the Tip Blunting Force Test. Three individual needles are tested, and each needle is pressed against the porcine skin with the maximum force of 50 N in the initial insertion test and all three subsequent re-insertion tests. The check mark for the skin staining result represents successful insertion verified by the dye staining of the VE. Each microneedle tip is examined under an optical microscope after all four insertion tests, and no significant tip deformation or fracture is observed.

Sequence of Insertion Test \ Sample no. of MN	1	2	3
initial 50N insertion test	✓	✓	✓
first 50N re-insertion test	✓	✓	✓
second 50N re-insertion test	✓	✓	✓
third 50N re-insertion test	✓	✓	✓
remark	no significant tip deformation or fracture observed after all insertion tests		

Fracture Force Estimation

The intrinsic fracture of an MN against a rigid surface is discussed in Subsection 3.5.3. With potential applications of MNs for live animals and in clinic, the fracture force of the MN when being pressed against skin for insertion was characterized. Three individual needles were tested to estimate the fracture force against porcine skin using the apparatus described previously. Successful insertion of each needle into porcine skin was confirmed with the examination of the skin staining under an optical microscope following the insertion.

Minor plastic deformation of the needle tip was observed under an optical microscope following the test in two of the three MNs, and no significant deformation was observed in the third. Figure 60(a) and Figure 60(b) show optical micrographs of one of the two needles with minor plastic deformation prior to and following the fracture test, respectively. A comparison of the two micrographs shows that the tip of the needle was plastically deformed with a vertical distance of 16 μm. Plastic deformation with a vertical distance of 30 μm was observed at the needle tip of the other MN.

In all three needles, no fracture of the MN was observed under an optical microscope, indicating that the fracture force of the needle for insertion into porcine skin is in excess of 90 N. With the insertion force of 2.4 N shown in Figure 57, the margin of safety, defined as the ratio of the fracture force to the insertion force, is higher than 37. Moreover, the maximum force produced by a human thumb has been empirically determined and reported in the literature to be 105 N. [122]

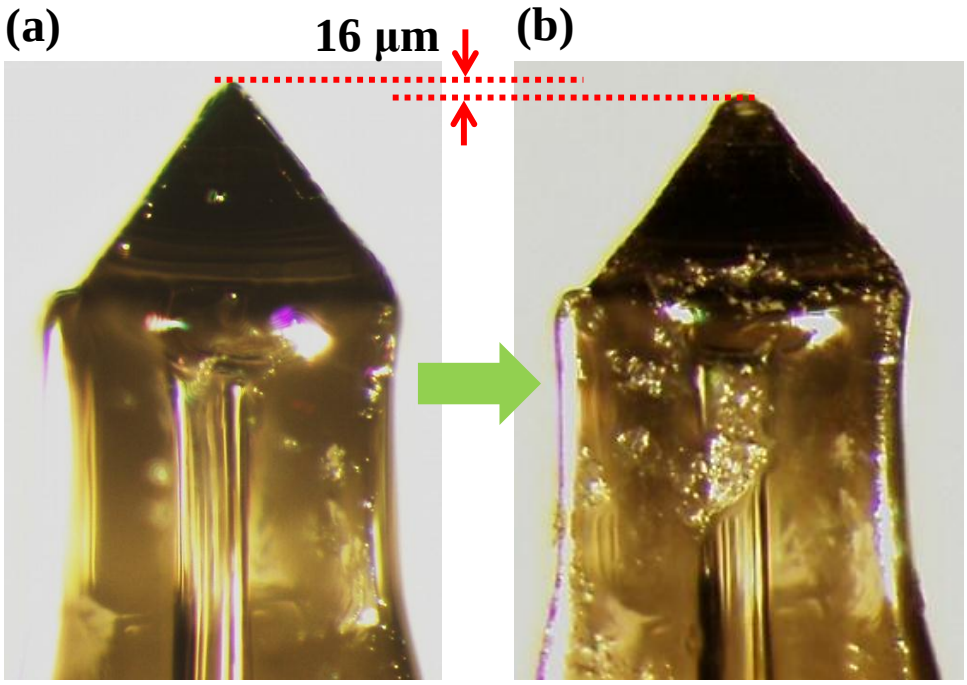

Figure 60. Optical micrographs of the side view of a microneedle (a) before and (b) after the fracture test with the maximum driving force of 90 N against porcine skin. Minor plastic deformation of the needle tip is observed following the test.

3.6 Chapter Conclusion

A polymer-based fabrication process using UV lithography into micromolds is proposed to construct a hollow microneedle array with a baseplate. Fabricated pyramidal-tip SU-8 microneedles are 825 µm in height and 400 µm in width with a lumen opening of 120 µm in diameter. The tip diameter across the 10 × 10 needle array ranges from 15 to 25 µm. Microfluidic characterization indicates 20% of the lumens are well-defined.

Using UV lithography into micromolds allows complex 3D structures to be defined with both the mask pattern in the lithography process and the topography of the micromold. With a pre-constructed PDMS mold defining the tip of the microneedle, the shaft and lumen of the needle as well as a baseplate are all constructed with SU-8 in a

dual exposure lithography process. This conventional UV lithography process is batch processing that is scalable for the manufacturing of microneedles. Moreover, UV lithography and micromolding methods are expected to have low mass production costs.

Mechanical characterization shows the pyramidal tip of the fabricated microneedles fractures against a rigid surface with a driving force of 12.0 ± 0.8 N. The insertion performance of microneedles is evaluated with excised porcine skin. The driving force required for successful insertion of a microneedle into skin is empirically determined to be 2.4 ± 1.2 N. With the driving force increased to 50 N, the needle remains capable of successful insertion into skin with the same force after the first insertion is obtained. Moreover, the application of the 90 N force on a single needle causes minor tip deformation with no fracture observed under an optical microscope.

In this chapter, HMNs measuring 825 μm in height and with a well-defined lumen of 120 μm in diameter are demonstrated using UV lithography into micromolds and SU-8 as a structural material, confirming the feasibility of such fabrication approach in creating tall and complex needle structures. However, the high insertion force of 2.4 N per needle may cause a significant concern when a large number of needles are required to insert into skin. For hypodermic needles, a change in tip geometry has been reported to lower their insertion force. [131] In Chapter 4, HMNs with improved tip geometry are presented and characterized.

CHAPTER 4

HYPODERMIC-NEEDLE-LIKE HOLLOW MICRONEEDLE ARRAY

4.1 Introduction

Hypodermic needles (HNs) are widely used to deliver a variety of biological molecules into the body through the skin. A sharp beveled tip and a large side opening are key characteristics of HNs, contributing to ease of insertion and efficient, nearly clog-free drug delivery into skin. The sharp tips of HNs are produced by a beveling process, reducing the required penetration force into skin as well as the pain perceived by patients during insertion [131, 132]. The needle lumens, which terminate on the side of the bevel, are expected to be less susceptible to tissue clogging during insertion and form a larger fluid up-take area in the skin [133-135]. Similarly, micromachined needles, or microneedles (MNs), with such side-terminated lumens exhibit superior fluid delivery performance over MNs with a top-terminated lumen [133]. Figure 61(a) shows an optical micrograph of the needle tip of a conventional 26-gauge (26G) hypodermic needle (HN), showing the sharp beveled tip and large side-terminated lumen opening.

As stated in Chapter 1, MNs have been reported to successfully transport biological molecules into the body with minimal invasiveness and pain, following the insertion of needles into the skin [136]. Biological molecules delivered through microneedles (MNs) into the skin have been shown to induce immune responses or biological effects that are comparable to those induced by an HN injection in animal and human studies [1, 15-17, 96]. Therefore, integration of the two key characteristics of HNs,

namely a sharp beveled tip and a large side opening, into the design of MNs can potentially lead to enhanced MN performance. An optical micrograph of the fabricated HNL MN, presented in this chapter, with a sharp beveled tip and a large side opening is shown in Figure 61(b).

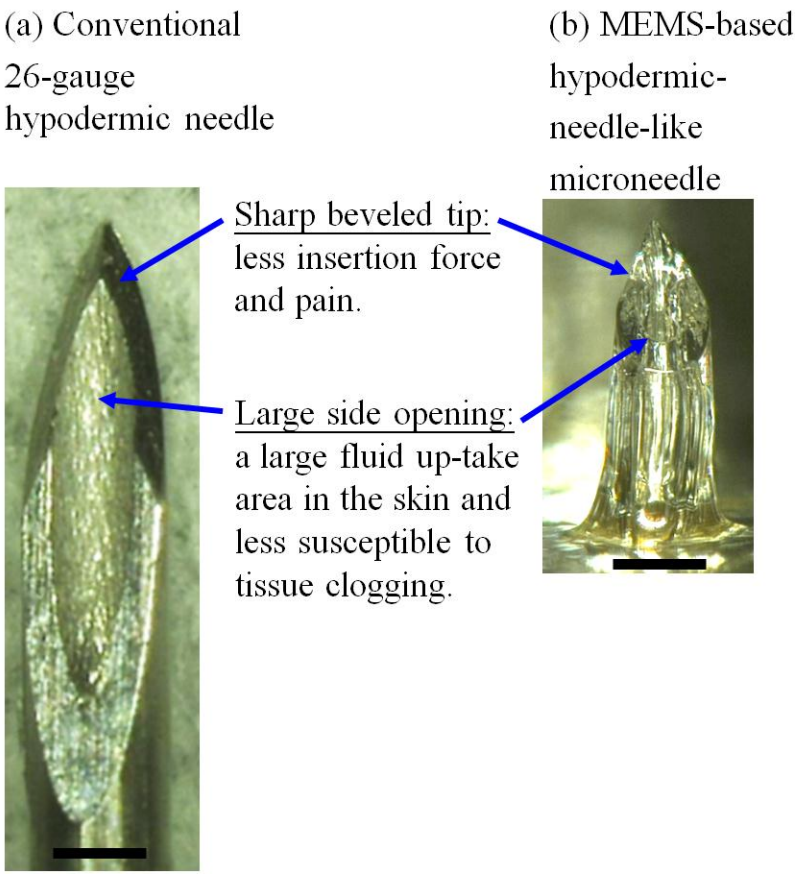

Figure 61. Optical image of (a) a conventional 26-gauge hypodermic needle and (b) an MEMS-based hypodermic-needle-like microneedle. The major characteristics of a conventional hypodermic needle, a sharp beveled tip and a large side opening, were mimicked in the MEMS-based hypodermic-needle-like microneedle. The scale bar in both (a) and (b) is 300 µm.

4.2 Microneedle Design

The fabrication concept for the combination of conventional UV lithography and a single-step micromolding technique to construct HNL MNs is shown in Figure 62. As shown in Figure 62(a), when light perpendicularly illuminates the photomask, a circular pattern on the mask is projected onto the slope of the mold, creating an elliptical shape on the slope. By changing the pattern on the mask, various projected shapes on the sloped sidewall of the mold can be obtained. With a negative photoresist (e.g., SU-8) filling the region between the mask and the mold, the beveled tip, lumen, and shaft of an HNL MN can be defined simultaneously with a single UV exposure, Figure 62(b). The angle of the slope of the mold defines the bevel angle of the MN tips and can be altered during the construction of the mold, and the sharpness of the tip can be defined lithographically. This combination of UV lithography and micromolding allows the geometry of the MN tip to be optimized three-dimensionally with two dimensions from the design of the mask pattern and one dimension from the slope angle of the mold.

The schematic illustrations were created using the CAD tool, SolidWorks, discussed in Section 3.1. To create the illustrations in Figure 62, a 5 mm × 1 mm rectangular pattern was sketched and extruded by 930 μm to outline the mold, followed by a chamfer intersecting with the top surface of the mold at an angle of 55° and at a distance of 400 μm from the lower left edge of the mold to create the slope of the mold. Aligned with the 5 mm × 1 mm rectangular pattern, another 5 mm × 1 mm rectangular pattern was drawn at a distance of 540 μm above the top surface of the mold to outline a photomask. Centered at a point that is 180 μm from the lower edge of the mask, two concentric circles of radii of 75 μm and 150 μm were sketched as the photomask design.

The area between the two concentric circles was extruded downward to the slope of the mold to create the depiction of exposed SU-8.

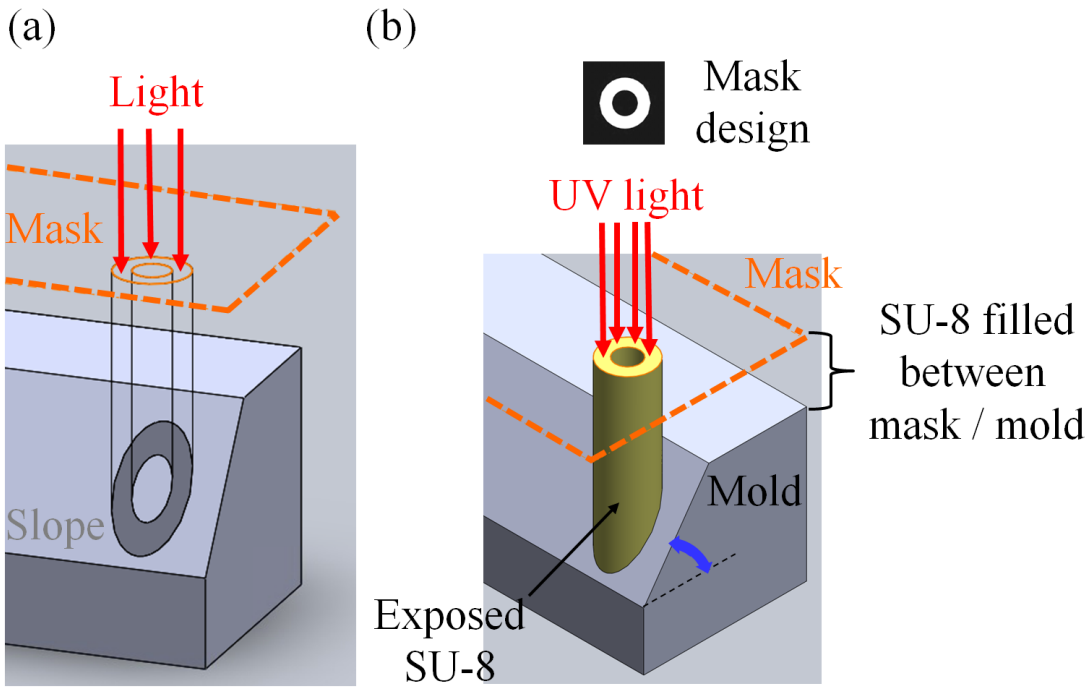

Figure 62. (a) Projection of a two-dimensional mask pattern onto a three-dimensional surface. (b) Illustration of the construction of a microneedle structure by a combination of UV exposure and the topography of a mold.

4.3 Microneedle Fabrication

4.3.1 Fabrication Process Flow

The fabrication process of the HNL MN array started with a pre-constructed, reusable polydimethylsiloxane (PDMS) mold. The construction of this PDMS (Sylgard 184, Dow Corning, Midland, MI, USA) mold involved the use of an inclined UV lithography process [137] to create an SU-8 master, followed by a two-step micromolding technique [118] to replicate this SU-8 master in PDMS as discussed in

Subsection 3.4.1. The ultimate PDMS mold comprised a 6×6 array of square recesses. Each recess measures approximately 500×500 μm with 900 μm spacing between recesses. The cross-section of each recess is a right-angled triangle, as shown in Figure 63(a), 715 μm in depth. Following the construction of the PDMS mold, the fabrication process flow of an SU-8 HNL MN on the constructed PDMS mold is shown in Figure 63. A quantity of SU-8 2025 (MicroChem Corp., Newton, MA, USA) was first preheated at 60 ℃ for 30 minutes on a hotplate in order to reduce its viscosity for better encapsulation of the micro-trenches in the PDMS mold. The top surface of the PDMS mold was treated using oxygen plasma for 20 minutes to increase its hydrophilicity prior to the SU-8 encapsulation, shown in Figure 63(a). Following the surface treatment of the PMDS mold, the preheated SU-8 was cast manually by weight onto the PDMS mold to obtain a thickness of 600-650 μm. To eliminate trapped air bubbles in the PDMS trenches during the casting process, a backside vacuuming (BSV) process was performed for one hour, as shown in Figure 63(b). In the BSV process, because of the gas permeability of PDMS [102], the air trapped at the bottom of the PDMS trenches was drawn through the PDMS mold and subsequently purged. The SU-8/PDMS sample was then placed on a hotplate at 85 ℃ for 16 hours to soft bake the SU-8.

To define an HNL MN array with a baseplate, a UV (365 nm, i-line) lithography process, consisting of two exposure steps with separate masks, was used. The beveled tip, lumen, and shaft of an HNL MN were defined simultaneously by the first exposure with a UV dosage of 1800 mJ/cm^2, as shown in Figure 63(c). A post-exposure-bake (PEB) step was then performed on a hotplate at 85 ℃ for 30 minutes. Prior to development, the baseplate of the HNL MN array was formed using a second exposure with a reduced UV

dosage of 300 mJ/cm^2 and a mask that blocked the needle lumens and shafts from the exposure, as shown in Figure 63(d). For faster heat transfer to the baseplate located on the top of the SU-8/PDMS sample, the second PEB process was carried out in an oven, instead of a hotplate, at 85 ℃ for 15 minutes.

The SU-8 structure was then demolded from the PDMS mold and held in a static propylene glycol methyl ether acetate (PGMEA) bath with both openings of the lumen in contact with the PGMEA (Microposit Thinner Type P, Rohm and Haas Electronic Materials, Marlborough, MA, USA) solution for six hours to develop the SU-8, as shown in Figure 63(e). Following the development, the sample was gently blown dry using a nitrogen gun. The developed HNL MN with a baseplate is shown in Figure 63(f). To complete the fabrication, both sides of the SU-8 MN array were UV-flood exposed with a UV dosage of 10 J/cm^2, followed by a hard bake of the SU-8 on a hotplate at 135 ℃ for 30 minutes.

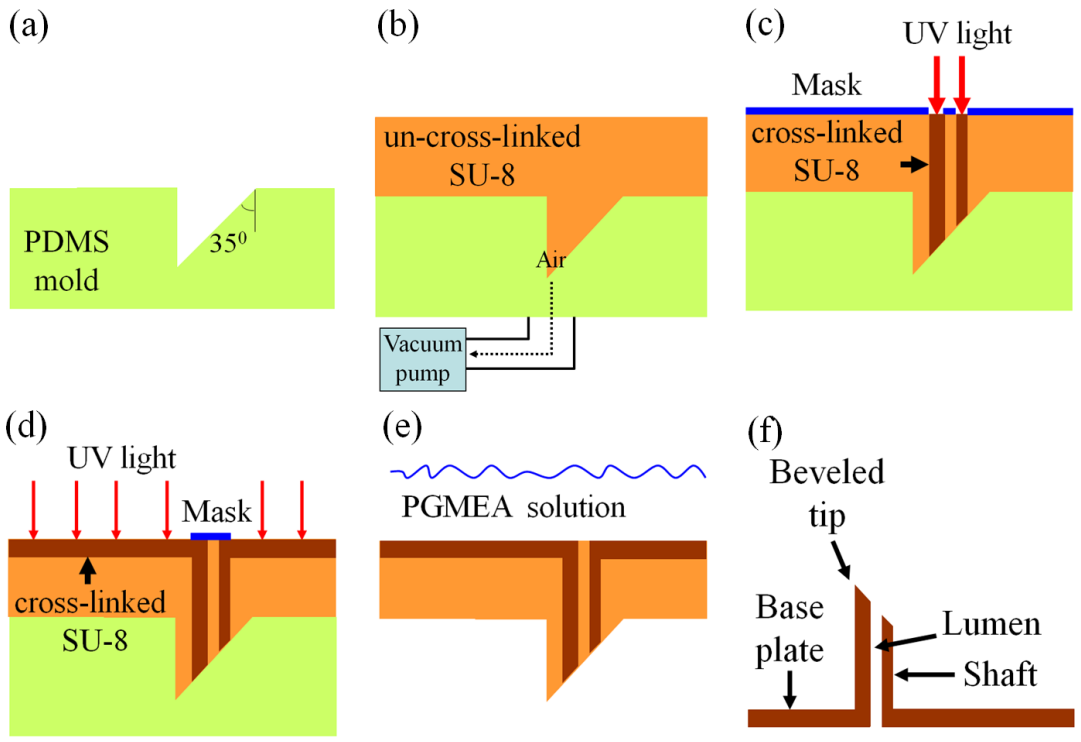

Figure 63. Fabrication process flow of the hypodermic-needle-like microneedle structures. The UV dosage in step (c) is 1800 mJ/cm^2, and that in step (d) is 350 mJ/cm^2.

4.3.2 Fabrication Process Development

In addition to the process improvements discussed in Section 3.2, two process parameters were optimized for HNL MN fabrication. As discussed in Subsection 3.4.4, the SU-8 softbake temperature is a critical factor in lumen formation inside micromold trenches. Therefore, the SU-8 softbake condition is optimized to ensure well defined lumens. Moreover, the duration of backside vacuuming is studied for shorter processing time.

SU-8 Softbake Condition

As discussed in Subsection 3.4.4, an excess thermal budget in the PDMS trench during the SU-8 softbake step may result in local SU-8 polymerization without UV radiation, leading to a failure in the patterning fidelity in UV lithography. Therefore, to obtain a well-defined MN tip in the first UV exposure (Figure 63(c)), the SU-8 softbake condition was optimized to lower the thermal budget in the PDMS trench. Figure 64 shows optical micrographs of the bird's-eye view of two MNs fabricated with different SU-8 softbake conditions. The SU-8 softbake condition is 95℃ for 24 hours and 85℃ for 16 hours for the MN in Figure 64(a) and Figure 64(b), respectively, and all other processing parameters are identical for these two MNs. In Figure 64(a), a significant amount of polymerized SU-8 around the needle tip is observed, and this polymerized SU-8 was in the PDMS trench and not exposed to the UV radiation in the first exposure. With a reduced thermal budget in the PDMS trench because of the SU-8 softbake temperature lowered from 95℃ to 85℃ and the time decreased from 24 hours to 16 hours, the tip of the MN shown in Figure 64(b) is well-defined with no excess polymerized SU-8 around the needle tip. The observation in Figure 64 confirms that an excess thermal budget in the softbake step of thick SU-8 processing results in local polymerization of SU-8 without UV radiation, and this loss of patterning fidelity in the UV lithography can be restored with the optimization of the SU-8 softbake condition.

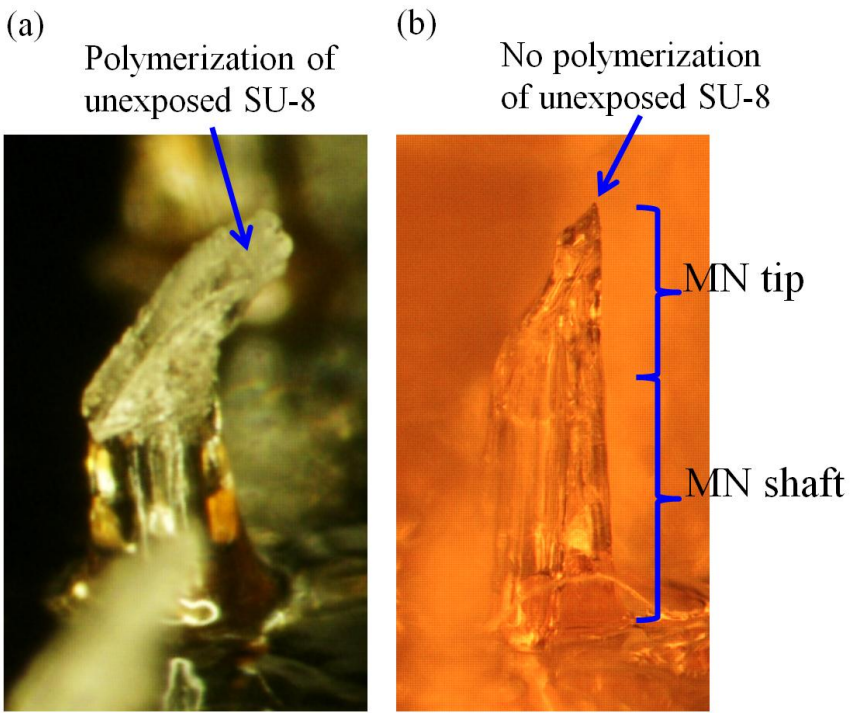

Figure 64. (a) An optical micrograph of the bird's-eye view of an MN in an MN array fabricated with the SU-8 softbake condition of 95 ℃ for 24 hours. Severe polymerization of unexposed SU-8 near the needle tip is observed. (b) An optical micrograph of an MN in an MN array fabricated with the SU-8 softbake condition of 85 ℃ for 16 hours. No excess SU-8 polymerization is observed at the needle tip.

Backside Vacuuming

The purpose of the BSV process followed the casting of SU-8 onto PDMS trenches is to draw the trapped air bubbles from the bottom of the PDMS trenches through the PDMS mold. The BSV process was performed for 3 hours during the construction of PT MNs. Initially the BSV process was performed for three hours for the construction of HNL MNs. Figure 65(a) and Figure 65(b) show optical micrographs of the top view of the SU-8/PDMS sample prior to and following a three-hour BSV process, respectively. In Figure 65(a) all 30 trapped air bubbles located along the bottom edge of the PDMS trenches since the bottom edge is the deepest edge. All 30 air bubbles were eliminated following the three-hour BSV process, as shown in. Figure 65(b).

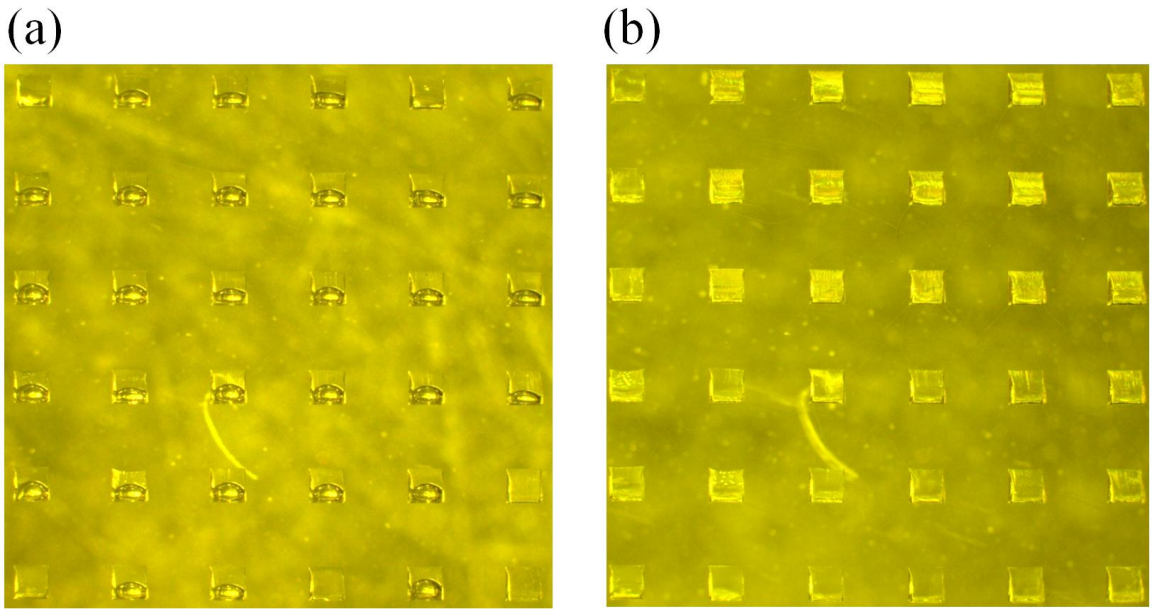

Figure 65. Optical micrographs of the top view of the SU-8/PDMS sample in Figure 63(b) before (a) and after (b) a three-hour backside vacuuming process. (a) Thirty air bubbles trapped at the bottom of the PDMS trenches in this 6×6 trench array. (b) Elimination of the trapped air bubbles.

To reduce the overall fabrication time of HNL MNs, the BSV process time was decreased from three hours to one hour. Optical micrographs of the top view of the SU-8/PDMS sample prior to and following the reduced one-hour BSV process are shown in Figure 66(a) and Figure 66(b), respectively. With the BSV process time reduced to one hour, no air bubble was observed under an optical microscope, as shown in Figure 66(b). In following processes of the SU-8/PDMS sample, e.g., softbake and lithography process steps, no air bubble was observed and the needle tips of the HNL MNs were well-defined. Therefore, the BSV process time was reduced to one hour for all subsequently fabricated samples.

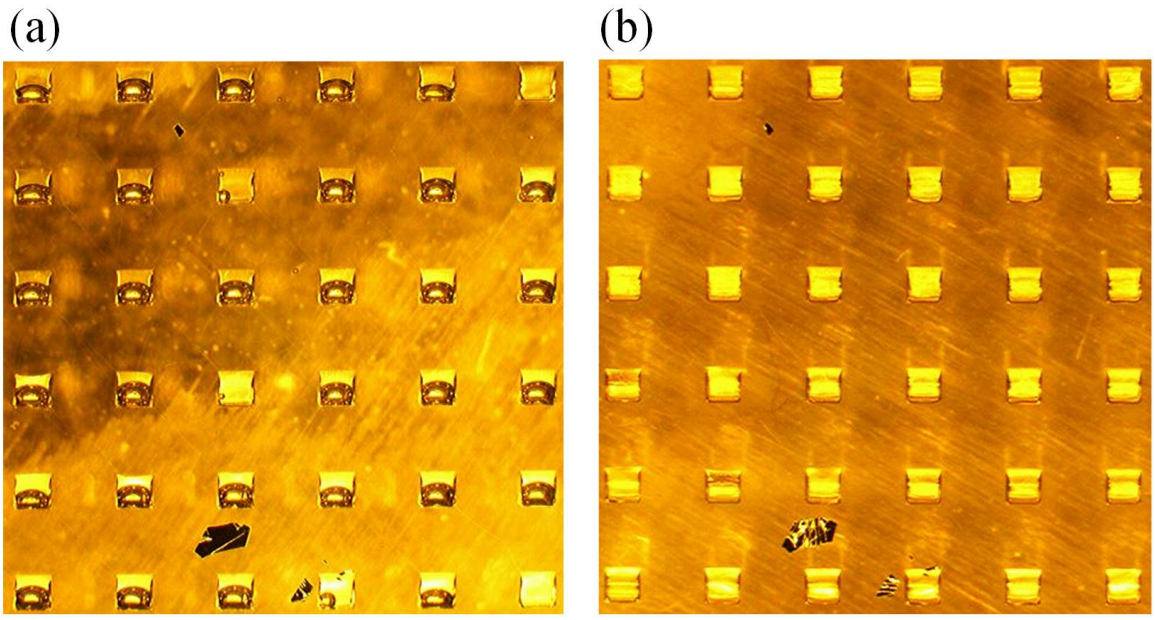

Figure 66. Optical micrographs of the top view of the SU-8/PDMS sample in Figure 63(b) before (a) and after (b) a reduced one-hour backside vacuuming process.

4.3.3 Fabrication Results

Three different mask designs, their resultant expected MN shapes as determined from projection CAD, and fabricated MNs, are shown in Figure 67. The bevel angle of the MN tips is 35 ° in all three CAD drawings. The fabricated HNL MN shown in Figure 67(c) is 980 μm tall with a 300 μm wide shaft. The distance between the lumen opening and the baseplate is 590 μm. The diameter of the lumen opening is 150 μm. The baseplate thickness is 310 μm. The mask design in Figure 67(c) was selected to construct HNL MNs for further characterization discussed in this chapter. Resultant CAD projections shown in Figure 67 were drawn using the SolidWorks tool. Mask designs were sketched on the top surface of the mold shown in Figure 62 with centers of the lumen located at a distance of 320 μm from the lower left edge of the mold and subsequently extruded to the plane of the mold slope to create the resultant projections.

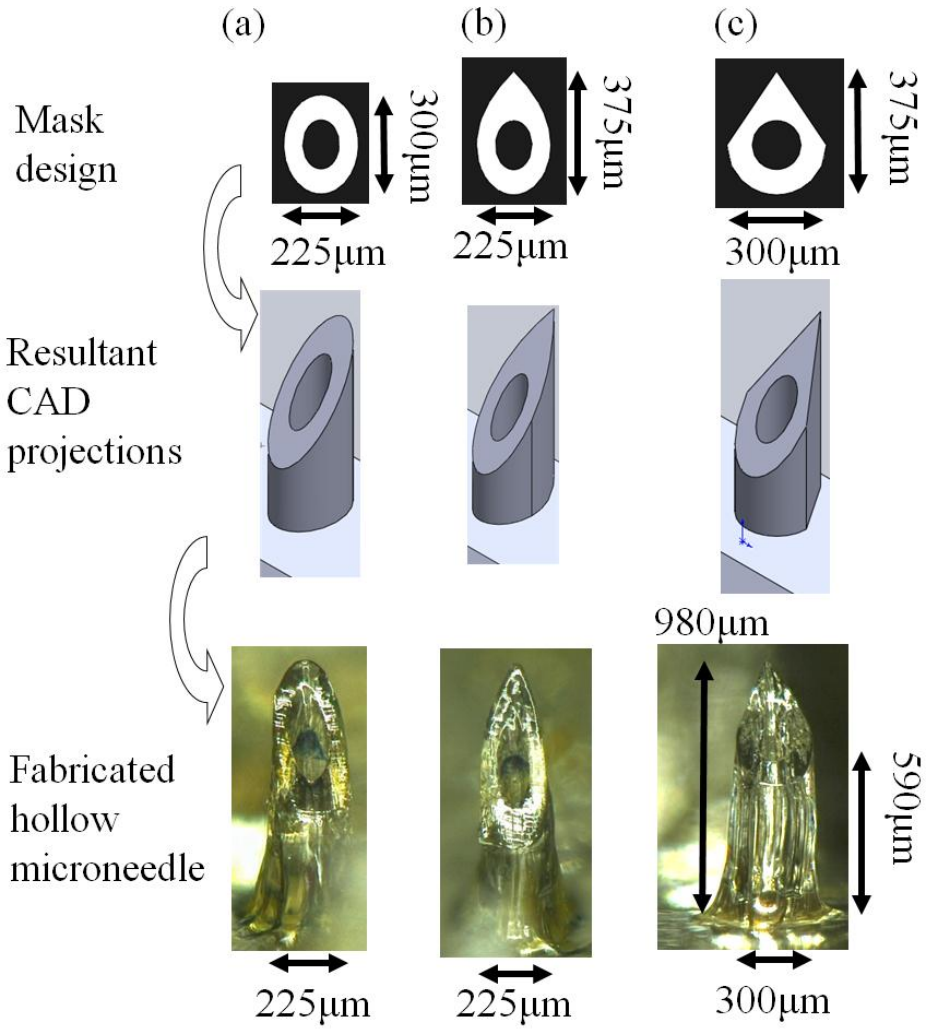

Figure 67. Three different mask designs, resultant CAD projections of three microneedle tips from each designs, and optical micrographs of corresponding fabricated hollow microneedles.

Figure 68 shows the optical micrograph of the fabricated HMN in Figure 67(c) with two red dashed rectangles to highlight the footing of the HMN. The term, footing is used to refer to the phenomenon that the bottom section of the MN shaft is wider than other sections, and in the bottom section the shaft is wider as it is closer to the baseplate.

This phenomenon is also observed in work performed by other researchers using SU-8 to construct tall HMNs with a baseplate (Figure 5 in [47]).

This footing phenomenon can be attributed to the diffusion of cross-linking catalyst across the boundary between unexposed and exposed SU-8 during the PEB step. As discussed in Section 2.5, SU-8 consists of three components: epoxy resin, solvent, and PAG [67]. Upon UV exposure, the PAG decomposes to form the HFA acid. In the subsequent PEB step, with the HFA acid acting as a catalyst and the application of heat, the polymerization of the epoxy resin occurs. [68] In the unexposed SU-8, the PAG does not decompose, and therefore without the HFA acid acting as a catalyst the polymerization of the epoxy resin do not occur. Nonetheless, at the interface of the exposed and unexposed SU-8, the HFA acid in the exposed SU-8 may diffuse into the unexposed SU-8 at elevated temperatures during the PEB step, leading to the polymerization of the epoxy resin in the unexposed SU-8. This diffusion of the HFA acid into the unexposed SU-8 is believed to cause the observed expansion of the exposed SU-8 in [138] and [139]. In Figure 68, during the PEB step, a combination of the outward diffusion of the HFA acid from the exposed MN shaft and the upward diffusion of the HFA acid from the baseplate may result in an increased concentration of the HFA acid at the junction of the MN shaft and the baseplate, leading to the observed footing.

To reduce the diffusion of the HFA acid, several process parameter optimizations have been proposed [139]. Lowering the temperature and reducing the time of thermal processing, e.g. the PEB process, can reduce the diffusion [140]. Moreover, optimization of SU-8 softbake process parameters to lower the solvent content in the SU-8 has been

reported to enhance the SU-8 pattern resolution by reducing the diffusion of the HFA acid [139].

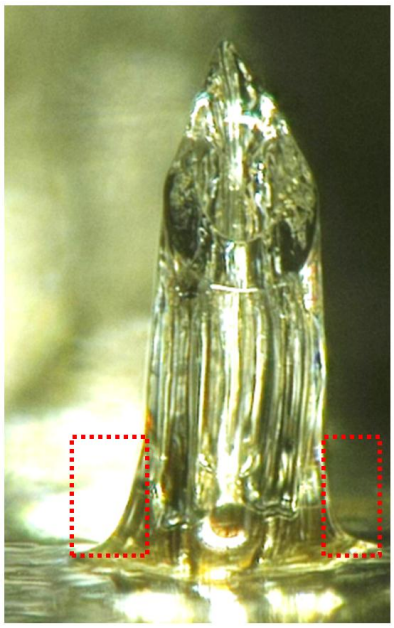

Figure 68. Optical micrograph of the fabricated HMN in Figure 67(c) with its 'footings' highlighted by two red dashed rectangles.

The tip sharpness of fabricated HNL MNs was characterized using a high-magnification (2500×) optical microscope (VHX-600 Digital Microscope, Keyence Corp., Osaka, Japan). Figure 69 shows optical micrographs of the needle tip of two HNL MNs fabricated using the mask design in Figure 67(c). The tip diameter of the needle tip shown in Figure 69(a) and Figure 69(b) is 29.98 μm and 27.58 μm, respectively, indicating that the tip diameter of fabricated HNL MNs is ~30 μm.

(a)

(b)

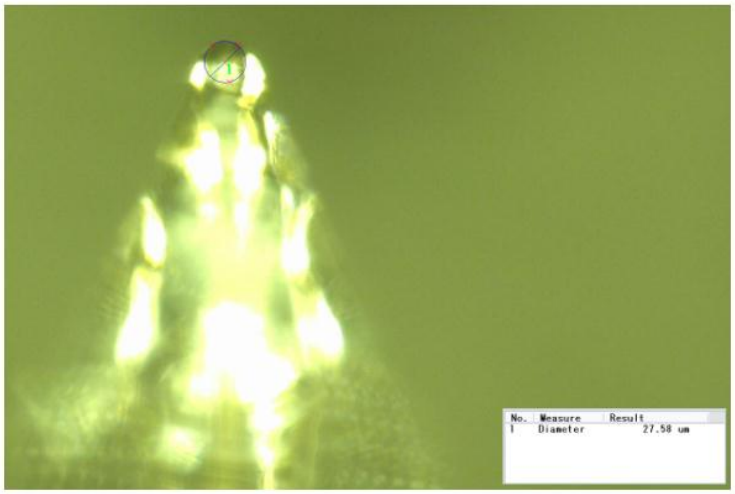

Figure 69. Optical micrographs of the front view of the needle tip of two HNL MNs. (a) The tip diameter of the needle tip is 28.98 μm. (b) The tip diameter of the needle is 27.58 μm.

Inspection of tip patterns of the photomask shown in Figure 67(c) using the same 2500× optical microscope indicated the tip diameter in the photomask is ~10 μm, as shown in Figure 70. In addition to the non-infinitely-small tip pattern in the photomask, the diffusion of the HFA acid during the PEB steps may further enlarge the tip diameter

of HNL MNs. In a previous study [139], ~1 μm expansion of 5 μm × 5 μm SU-8 squares was observed, and the SU-8 squares with a thickness of 2 μm were constructed using UV lithography with a dosage of 200 mJ/cm^2. A significantly higher dosage of the first UV exposure (1800 mJ/cm^2) for HNL MNs may result in a larger expansion of SU-8 (>1 μm) at the needle tip.

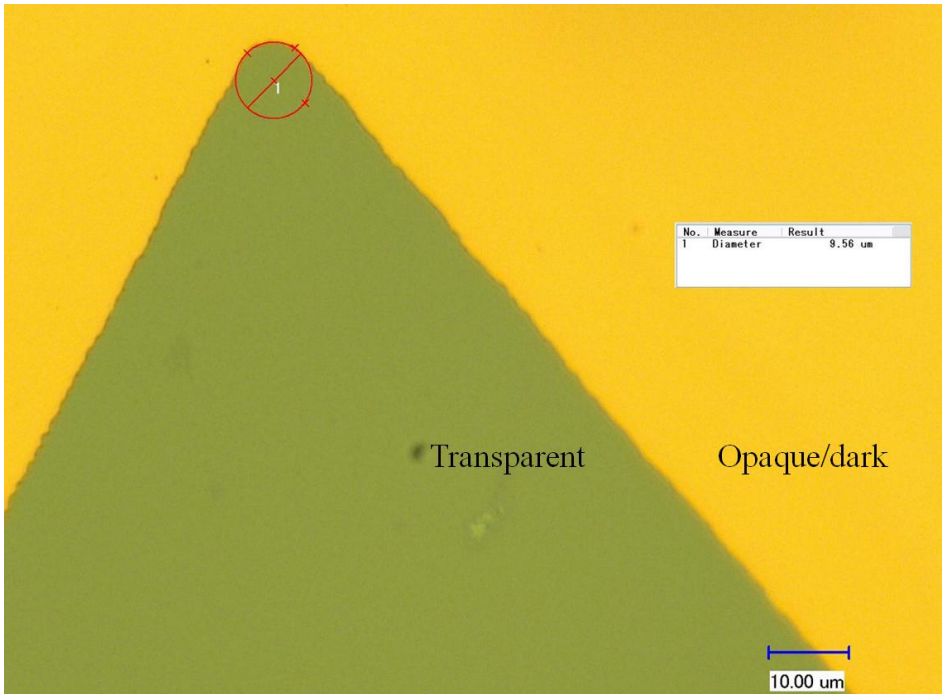

Figure 70. Optical micrograph of a tip pattern of the photomask shown in Figure 67(c). The tip diameter is ~10μm.

To verify the lumens are well-defined inside the fabricated MNs and baseplate, a microfluidic channel test of the fabricated HNL MN array was carried out using a custom package and fluid test setup discussed in Subsection 3.4.3. In the test, a syringe pump drove the blue dye in a syringe at a flow rate of 2.0 ml/min through the tubing, a PDMS housing, a dye reservoir, and then any well-defined lumens in the MN array, followed by

the dye being ejected from the MN array in streams. Figure 71 shows an optical image of the custom package and dye streams ejected from the MN array. The number of the ejected dye streams corresponds to the number of well-defined lumens. Therefore, the observed dye streams in Figure 71 indicated at least 85% of the lumens were open.

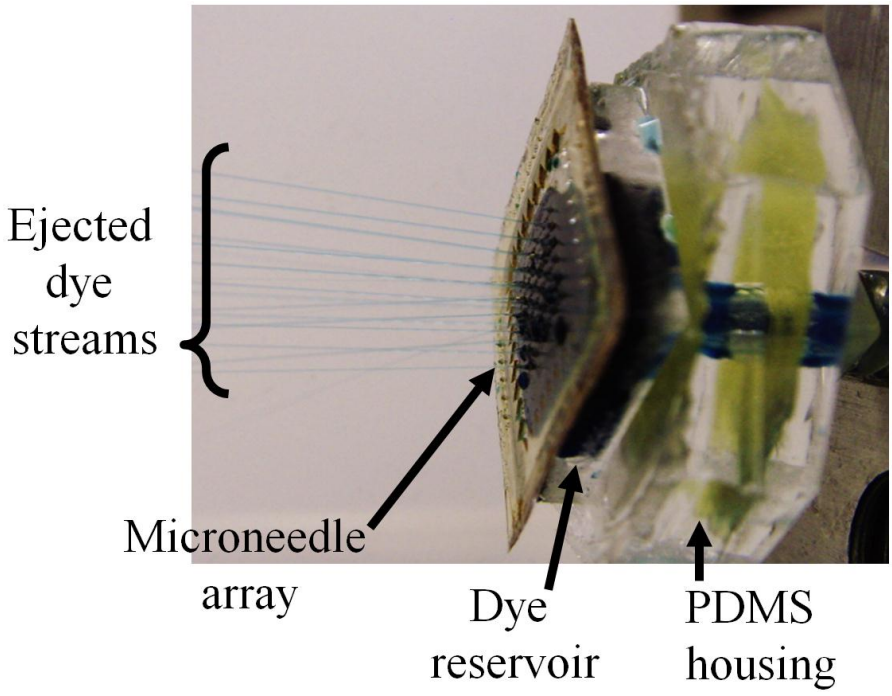

Figure 71. Optical still image of dye streams ejected from a microneedle array attached to a custom package in a microfluidic channel test. Eighteen visible streams ejected from an array of 21 hollow microneedles, suggesting an open lumen yield of 85%.

4.3.4 Process Limitations and Windows

Using UV lithography into micromolds with SU-8 used as the photosensitive material has been demonstrated to construct 1 mm tall HNL MNs as discussed in the previous subsection. Potential process limitations or windows of the height of the needle, the beveled angle of the needle tip, and the tip diameter are discussed in this subsection.

SU-8 microstructures of 1.5 mm in height with no hollow channel through the structure have been fabricated using UV lithography and demonstrated in [71]. With additional bulk processing of SU-8 prior to UV lithography, 1.5 mm tall microtubes have been demonstrated in [141]. Hence, with additional process optimization or modification, fabrication of 1.5 mm tall HNL MNs using UV lithography into micromolds is potentially feasible.

It is discussed in Subsection 4.4.2 that with the reduction of the tip angle and the change of tip geometry, the insertion force per needle is significantly lowered. Therefore, further reduction of the tip angle of HNL MNs may lead to lower insertion force. The tip angle of HNL MNs is defined by the inclined angle of the PDMS trench, as shown in Figure 63. To avoid the total internal reflection of UV radiation at the SU-8 / PDMS interface and subsequent undesired SU-8 crosslinking in the lumen, the inclined angle of the PDMS trench needs to be higher than 27.5 °, as discussed in Subsection 3.3.2. Therefore, the minimum tip angle of HNL MNs to ensure the formation of lumens is 27.5 °.

A smaller tip diameter is desired for HNL MNs, since the insertion force of MNs has been shown to increase with their tip diameter. [28, 129, 142] With additional bulk processing of SU-8 prior to the UV exposure and an antireflective film, consisting of an electrodeposited chromium black layer and two sputtered layers of copper and titanium, coated on the surface of silicon micromolds, a tip radius of 3-6 μm, which corresponds to a tip diameter of 6-12 μm, has been demonstrated in 1 mm tall SU-8 MNs fabricated using UV lithography into silicon micromolds [47], suggesting the feasibility of approximate 10 μm tip diameter fabricated using similar additional processes.

Moreover, the process windows of two critical process parameters, namely the softbake condition and the UV dosage in the first exposure shown in Figure 63(c), in thick SU-8 processing using UV lithography are identified for the fabrication of HNL MNs and summarized in the following discussion.

The SU-8 softbake condition in the fabrication of HNL MNs is 85 ℃ for 16 hours. It is shown in Figure 64 that increasing the softbake temperature and time to 95 ℃ and 24 hours, respectively, results in local polymerization of unexposed SU-8 near the needle tip. Similar phenomenon was observed in SU-8 MNs softbaked at 85 ℃ for 24 hours as shown in Figure 72, suggesting an upper process window of SU-8 softbake time of eight hours. The aim of a softbake process is to remove the solvent in the SU-8. Insufficient softbake of SU-8 may result in an excessive solvent content in the SU-8. Because of the high solvent content, SU-8, instead of being rigid, may be highly viscous. In the fabrication of HNL MNs, highly viscous SU-8 was observed following a softbake process performed at 85 ℃ for 12 hours. A small indent on the surface of this highly viscous SU-8 was created following the application of minor pressure from tweezers. This highly viscous SU-8 also adhered to the chromium photomask in the subsequent contact alignment and exposure. This increase in fabrication difficulty leads to a lower process window of SU-8 softbake time of four hours.

The UV dosage in the first exposure that defines the needle shaft and tip is 1800 mJ/cm^2 for HNL MNs. No significant difference was observed under an optical microscope for HNL MNs fabricated with a UV dosage of 3000 mJ/cm^2 in the first exposure. Nevertheless, significant reduction of the UV dosage in the first exposure may result in poor formation of needle tips, as shown in Subsection 3.3.5.

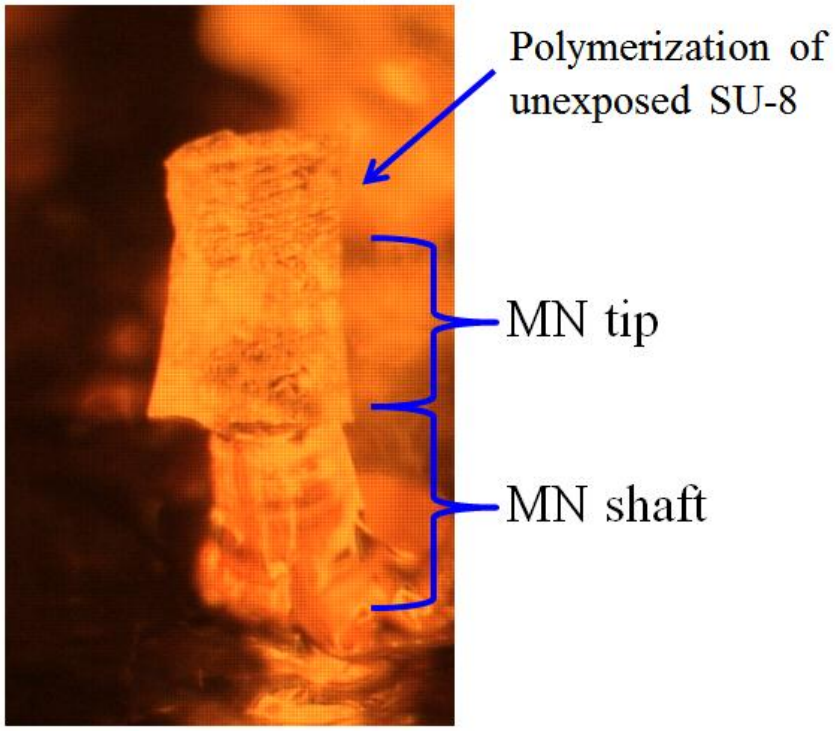

Figure 72. An optical micrograph of the front view of an MN fabricated with an SU-8 softbake condition of 85℃ for 24 hours. Severe local polymerization of unexposed SU-8 near the needle tip is observed.

4.4 Biological Characterization

4.4.1 Manual Insertion of a Microneedle Array into Excised Porcine Skin

The skin penetrability of the fabricated HNL MNs, as shown in Figure 67(c), was assessed with excised porcine skin. The excised porcine skin (Pel-Freez, Rogers, AR, USA) was shaved using a razor to trim the hairs on the skin. Subcutaneous fat on the back of the skin was subsequently removed with a scalpel. The resultant porcine skin was 3-4 mm in thickness. The prepared skin was then mounted under mild tension onto a wooden block using screws. The baseplate of a 6×6 MN array was affixed to the center of

the plate of a scanning electron microscope (SEM) specimen mount using double-sided tape. To insert MNs into the porcine skin, the MN array was then pressed perpendicularly against the skin by manually pushing the SEM mount toward the skin, followed by separation of the array from the skin. Successful insertion of needles into skin was defined as creation of an opening through the stratum corneum (SC) layer, the outmost layer of skin and a substantial barrier to essentially all high-molecular-weight drugs [2, 8]. To confirm the openings in the SC, one drop of blue dye was dispensed onto the skin surface. The dye flowed through the MN-defined pathways, if created as a result of successful insertion, in the SC and stained the viable epidermis (VE) underneath. Stain in the VE serves as an indication of successful insertion of the MN into the skin. The residual dye on the skin surface was then removed using alcohol swabs. The skin surface was examined under an optical microscope.

Figure 73(a) shows an optical micrograph of the top view of the insertion area on the porcine skin following the insertion test. In Figure 73(a), thirty-five stains in the VE can be easily identified, indicating 35 successful insertion loci out of the fabricated 6×6 needle array. The failed insertion point on the upper right corner of the array corresponds to a broken tip of the MN observed prior to the insertion test. A close-up view of an insertion site is shown in Figure 73(b). The red triangle at the center indicates the pathway created by successful insertion of an MN into skin, and the black circle highlights the region where the dye diffused and stained the VE underneath the SC. The side view of the same MN prior to and following insertion are shown in Figure 73(c) and Figure 73(d), respectively. No visible damage to the MN or bending of the MN tip was observed under an optical microscope after the insertion.

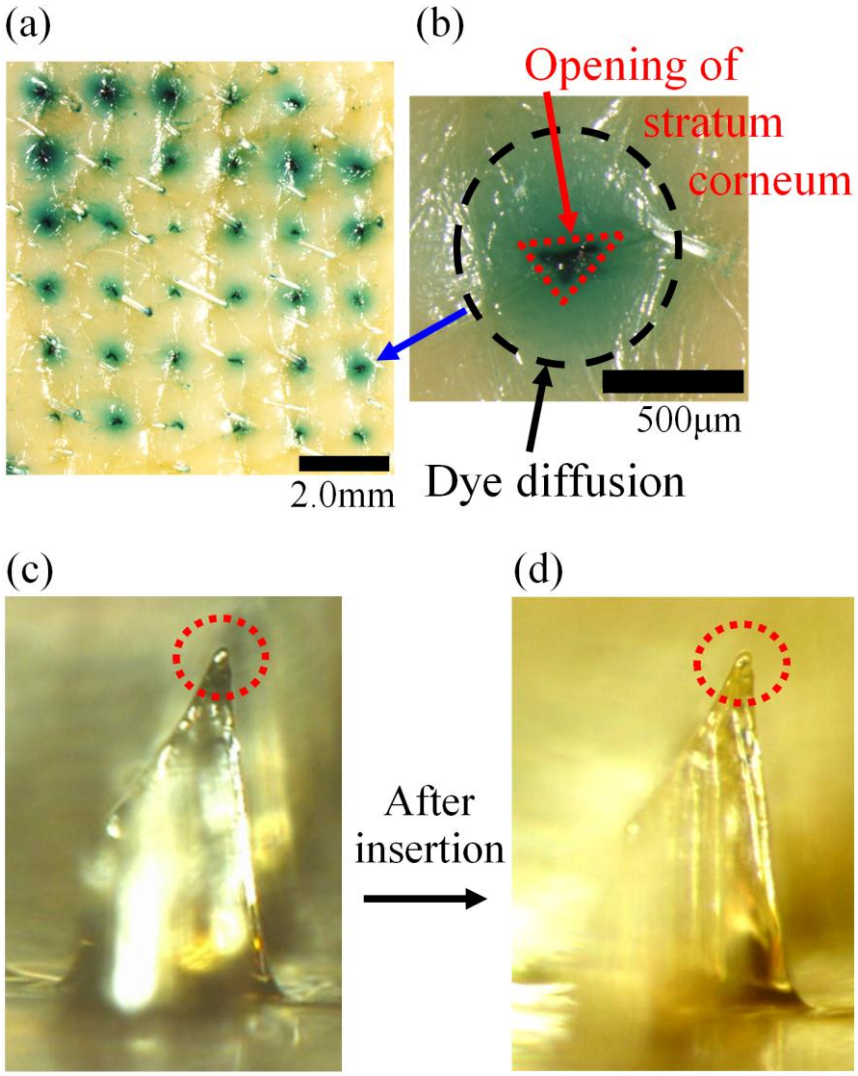

Figure 73. (a) An optical micrograph of the excised porcine skin following the manual insertion of a 6×6 microneedle array. (b) A close-up view of an insertion site, showing the opening in the stratum corneum created by needle insertion and the dye diffusion in the viable epidermis underneath the stratum corneum. (c)(d) Optical micrographs of the side-view of the same microneedle prior to and following manual insertion into skin, respectively. The dashed red circles highlight the needle tip.

4.4.2 Insertion Force Measurement

Mechanical interaction characterization of the HNL MNs was performed by driving individual HNL MNs perpendicularly against excised porcine skin. The required driving force for an HNL MN to successfully insert into skin, which is defined as insertion force, was evaluated. The maximum driving force that can be applied to an HNL MN during insertion without needle fracture was estimated.

To evaluate the insertion force for single HNL MNs, an HNL MN array with a baseplate was coated with 15 nm of chromium and 150 nm of gold using a sputterer for skin resistance measurement discussed in Subsection 3.5.4 to determine the insertion force. An individual HNL MN with its surrounding baseplate was cut from the MN array using a razor blade and then mounted onto the bottom surface of a flat-head steel machine screw. The machine screw was affixed to the center of the plate of an aluminum SEM specimen mount for ease of handling. For insertion force measurement of HNs, a 26G HN was directly mounted to an aluminum SEM specimen mount with the needle hub affixed to the center of the plate.

A force-displacement test station (Model 921A, Tricor Systems Inc., Elgin, IL, USA) with a built-in ohmmeter was used to perform the insertion test. An individual needle was driven perpendicularly against excised porcine skin at a rate of 1.0 mm/s by the load cell of the test station. The test station simultaneously recorded the driving force and displacement of the needle as well as the skin resistance between the needle and the electrode gel that was applied to the skin surface 1-2 inches away from the insertion site. An abrupt decrease in the skin resistance indicated the rupture of the highly-resistive SC layer, which defines successful insertion into skin. The driving force corresponding to the

abrupt skin resistance decrease is taken as the insertion force of the needle. Detailed descriptions of the preparation of individual needles and excised porcine skin as well as the experimental setup and test methodology are discussed in Chapter 3.

Eight individual HNL MNs were tested with each needle inserted into skin one or two times, yielding 14 data points for the insertion force. The mean of these 14 data points is 0.275 N with a standard deviation (SD) of 0.113 N. For the insertion force measurement of HNs, two conventional 26G stainless-steel HNs (305115, Becton Dickinson & Co., Franklin Lakes, NJ, USA) were used and 28 data points were obtained. The mean of the 28 data points is 0.284 N with a SD of 0.059 N. Figure 74 shows a chart of the insertion force for 26G HNs and HNL MNs with the mean, SD, maximum and minimum of obtained data points. The insertion force of HNL MNs is comparable to that of conventional 26G HNs, indicating that HNL MNs exhibit comparable insertion performance to 26G HNs.

As discussed in Subsection 3.5.4, using the skin resistance method shown in Figure 55, both the insertion force and the skin deformation when successful insertion occurs can be determined as shown in Figure 56. Figure 75 shows a chart of the insertion force and the skin deformation when successful insertion occurs for all the 28 data of 26G HNs and 14 data of HNL MNs shown in Figure 74. For both 26G HNs and HNL MNs, the insertion force increases linearly with the skin deformation as shown in Figure 75. Furthermore, for HNL MNs, successful insertion occurs with skin deformation of 400 μm or less. With the zero skin deformation denoting the MN tip touches the skin and the vertical dimension of the needle tip (the bevel portion of the needle) being ~450 μm, this observation on the skin deformation indicates that only the tip portion of the HNL MNs

contributes to successful insertion into skin with no involvement of the needle shaft. Similarly, for 26G HNs, successful insertion occurs with skin deformation of 600 μm or less, indicating that only the tip portion with the two upper side bevels of the 26G HN shown in Figure 61(a) is involved in successful insertion into skin.

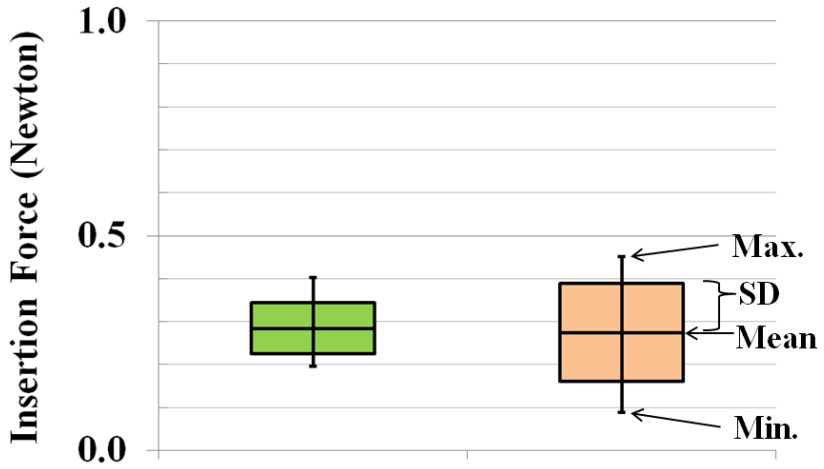

	26G HN (28 data pt. 2 HNs)	HNL MN (14 data pt. 8 MNs)
Mean	**0.284**	**0.275**
Standard Deviation (SD)	**0.059**	**0.113**
Max.	0.402	0.451
Min.	0.196	0.088

Figure 74. A chart showing the insertion force of 26-gauge hypodermic needles and hypodermic-needle-like microneedles. The mean, standard deviation, maximum, and minimum of all obtained data points are shown for both types of needles. The mean insertion force of hypodermic needles and microneedles is 0.284 N and 0.275 N, respectively, indicating that hypodermic-needle-like microneedles exhibit comparable insertion performance to hypodermic needles.

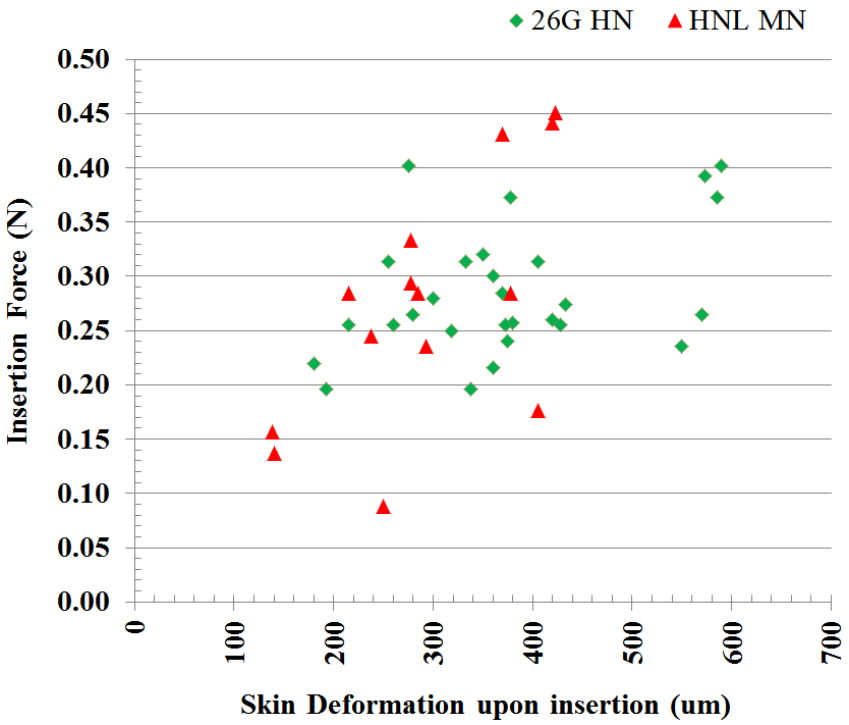

Figure 75. A chart of the insertion force plotted as a function of the skin deformation when successful insertion occurs for all 28 data of 26G HNs and 14 data of HNL MNs shown in Figure 74.

The insertion forces measured for HNL MNs are significantly lower than the previously-fabricated pyramidal-tip (PT) MNs, which were discussed in Chapter 3 and constructed using a similar fabrication approach but had different tip geometry. The insertion force of a PT MN into excised porcine skin was characterized as 2.4 N, which is approximately nine times higher than that of an HNL MN. The tip diameter of a PT MN ranges from 15 μm to 25 μm. Preliminary characterization using a high-magnification (2500X) optical microscope showed that the tip diameter of HNL MNs is ~30 μm as shown in Figure 69. The comparison of PT MNs and HNL MNs in the insertion force and tip diameter showed that the change of tip geometry from a pyramidal shape to an HNL one reduced the insertion force by approximately one order of magnitude with

comparable tip diameters, indicating that the tip geometry is an important factor in utilization of MNs in the applications of drug delivery into skin.

Insertion force of MNs has been shown to increase with their tip diameter or tip interfacial area. [28, 129, 142] A theoretical analysis based on the energy required to tear a membrane suggests that the insertion force increases linearly with the tip interfacial area of MNs. [129] Park et al. and Khanna et al. reported insertion force of MNs with a tip interfacial area ranging from 314 μm^2 to 5,000 μm^2 and from 185 μm^2 to 11,000 μm^2, respectively. [28, 142] Moreover, different linear regression equations were reported by Park and Khanna, which might be a result of different tip geometry and skin conditions. Park reported the insertion force of conical solid MNs into the skin of human subjects. Khanna fabricated hollow cylindrical microtubes with a sharpened wall acting as a tip and used human cadaver skin as a substrate.

For HNL MNs, the tip diameter of 30 μm leads to a tip interfacial area of 707 μm^2. Interpolation of the tip interfacial area of HNL MNs in the linear regression models reported by Park and Khanna suggests the insertion force of 0.085 N and 0.624 N, respectively. The mean of the insertion force of HNL MNs is 0.275 N, which is higher than the one suggested by Park and lower than the one suggested by Khanna. This difference in insertion force may be because of the different tip angles in these three MNs. The conical MNs reported by Park measures 1000 μm in height and 250 μm in base diameter, suggesting a tip angle of 14.3 °. [28] The tip angle of HNL MNs is 35 °, defined by the PDMS mold as shown in Figure 63(a). Khanna reported that the vertical dimension of the tapered tip profiles varied from 30 μm to 40 μm for the sharpened microtubes, and the wall thickness was calculated as 37.5 μm given that the outer and

inner diameters of the microtubes were 160 μm and 85 μm, respectively. [142] With a height of 30 - 40 μm and a base of 37.5 μm, the tip angle was calculated to be 50.2 ° - 64.0 °, higher than that of HNL MNs. An examination of the insertion force of these three MNs with a tip interfacial area of 707 μm^2 and their tip angles suggests that the insertion force increases with the tip angle of MNs. Moreover, the insertion force of HNL MNs ranges from 0.088 N to 0.451 N; these values are bracketed by the two values suggested by Park and Khanna and therefore is comparable to those reported in the literature for MNs with a similar tip interfacial area.

It is possible to obtain lower insertion force with needles of a smaller tip interfacial area. With a tip interfacial area of less than 0.031 μm^2 fabricated using silicon micromachining, insertion force of less than 0.010 N per needle can be achieved. [38]

For MN arrays, the insertion force per needle as a function of the needle spacing is proposed in the following discussion and is shown in Figure 76. Single MNs may be considered as an MN in a needle array with infinite spacing to adjacent MNs, and therefore in Figure 76 the insertion force for single MNs is represented by a small dot on the right of the chart. For MN arrays with large spacing between MNs, i.e., larger than a critical spacing (d_c), the skin deflection caused by an MN driving the skin downward may not interfere with adjacent skin deflection, and the MN and the skin underneath it may be considered as a mechanically independent subsystem from other adjacent subsystems. Therefore, the insertion force per needle does not vary with needle spacing for MN arrays with large spacing between MNs. For needle arrays with small spacing, i.e., smaller than the critical spacing (d_c), the skin deflection created by an MN may be affected by adjacent MNs. With small spacing between MNs, adjacent MNs may drive the skin

underneath the MN downward, resulting in a reduction of mechanical interaction between the MN and the skin underneath it. According to the theoretical model of insertion force presented by Davis in [129], for successful insertion to occur, the work applied to the skin by an MN needs to exceed a threshold energy that is a product of the skin puncture fracture toughness multiplied by the tip interfacial area. As the skin is driven downward and away from the MN by adjacent MNs as well as the mechanical interaction between the MN and the skin decreases, more work may need to be applied to the MN for it to exert the required threshold energy to the skin underneath it, leading to an increase in the required insertion force for the entire array and per needle. As the spacing decreases, the interference of skin deflection caused by adjacent MNs may become more substantial, leading to an increase in the insertion force per needle.

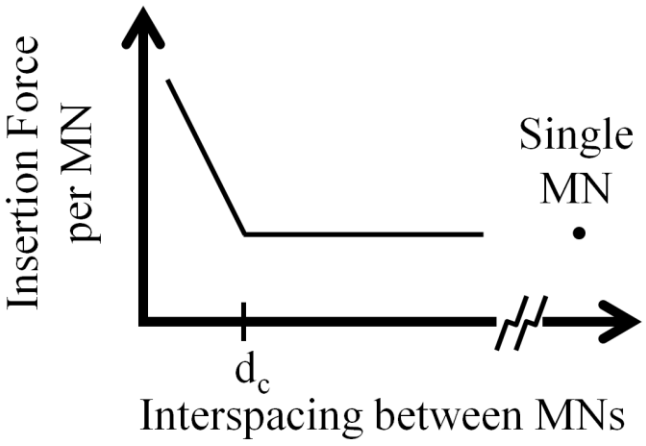

Figure 76. A chart of the insertion force per needle plotted as a function of the needle spacing within a needle array based on a proposed hypothesis.

This discussion of the insertion force per needle for needle arrays is a proposed hypothesis. Nevertheless, empirical results reported in the literature suggest a similar

relation between the insertion force per needle and the needle spacing within a needle array to the one shown in Figure 76. [143, 144] Olatunji et al. reported the insertion force of conical polymer MNs with a height of 600 μm, a base width of 300 μm, and interspacing at base ranging from 30 μm to 600 μm. [143] Excised neonatal porcine skin with a thickness of 700 μm was used as a substrate, and the needles were driven against the skin at a rate of 1.0 mm/s. The insertion force per needle was 0.0214 N for MN interspacing of 600 μm, 300 μm, and 150 μm, and increased to 0.0215 N and 0.0216 N for interspacing of 50 μm and 30 μm, respectively. A similar relation between the insertion force per needle and the needle spacing was observed by Lhernould. [144] Four-by-four arrays of 30-gauge HNs with a height of 1 mm, an outer diameter of 300 μm, and needle spacing ranging from 0.8 mm to 4.5 mm were mounted onto printed circuit boards. Silicone rubbers on top of a sponge-like material were used as a skin substitute, and needles were driven at a rate of 10 mm/s. The insertion force of a 4×4 needle array was ~ 4.0 N for spacing of 3.0 - 4.5 mm and 2.5 N for spacing of 2.5 mm. The insertion force increased to 4.5 N, 5.5 N, 7.0 N, and 9.5 N as the spacing decreases to 2.0 mm, 1.5 mm, 1.2 mm, and 0.8 mm. Therefore, in both experiments conducted separately by Olatunji and Lhernould, the insertion force per needle for a needle array is constant or within a relatively small range for needle arrays with large needle spacing, and for arrays with small needle spacing the insertion force per needle increases as the needle spacing decreases. These empirical results of the insertion force per needle as a function of needle spacing are similar to the one shown in Figure 76.

The critical spacing (d_c) is 150 μm and 2.5 mm, which is 25% of the 600 μm tall MNs and 250% of the 1 mm tall needles, reported by Olatunji and Lhernould,

respectively. The difference in the ratio of the critical spacing to the needle height may be a result of different needle profiles, substrates used as a skin substitute, and driving rates in these two experiments.

4.4.3 Fracture Force Estimation

To estimate the margin of safety, the fracture force of HNL MNs was characterized using excised porcine skin, the same substrate as in the insertion test. Three HNL MNs were tested using another force-displacement test station (ElectroForce 3200 Test Instrument, Bose Co., Eden Prairie, MN, USA) in order to increase the maximum driving force in the test. Similar testing procedures were performed as in the insertion test with an increased maximum driving force of 50 N. Following the test, successful insertion of each needle into skin was confirmed with the examination of the skin staining under an optical microscope. In all three tested HNL MNs, minor bending of the needle tip was observed under an optical microscope after the 50 N force application. Optical micrographs of the side view of one tested needle prior to and following the fracture test are shown in Figure 77(a) and Figure 77(b), respectively. No fracture of the needle was observed in all three needles, indicating that the fracture force of the needle for insertion into porcine skin is in excess of 50 N. With the fracture force higher than 50 N and the mean insertion force of 0.275 N for HNL MNs, the margin of safety for needle insertion into porcine skin prior to needle fracture is at least 180, which is approximately fivefold higher than the demonstrated margin of safety for PT MNs.

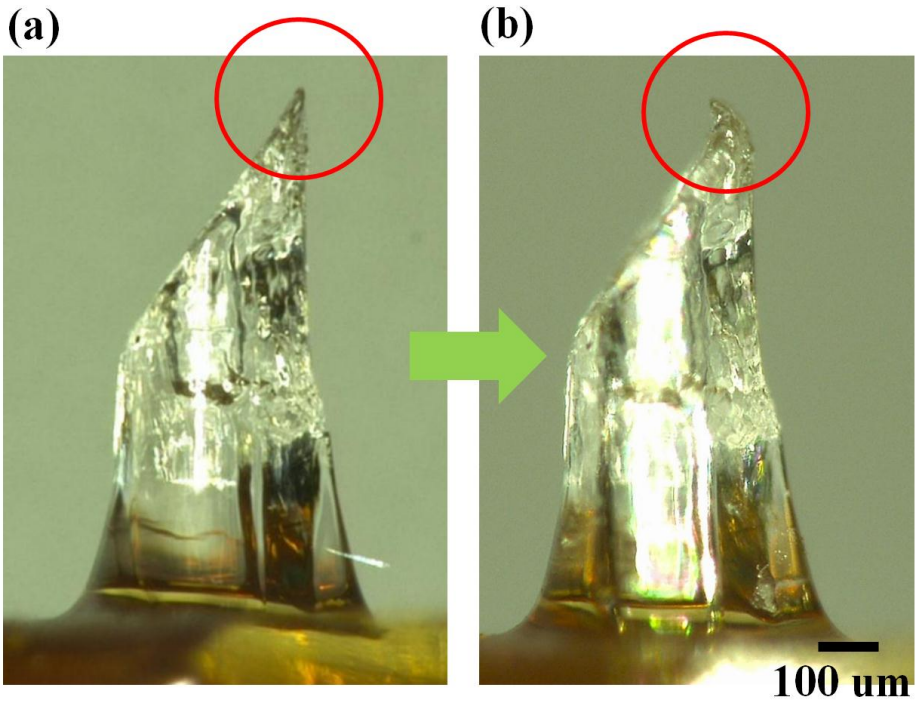

Figure 77. Optical micrographs of the side view of a hypodermic-needle-like microneedle (a) prior to and (b) following the fracture force test with 50 N force application against excised porcine skin. Minor bending of the needle tip was observed following the test. No fracture of the needle structure was observed. The scale bar in (b) is 100 µm.

4.4.4 Fluid Resistance of the Lumen

Fluid resistance is important in estimating the required pressure to drive fluid through a fluid channel at a given flow rate. Both theoretical calculation and empirical characterization of the fluid resistance of a lumen inside an HNL MN and the baseplate were performed. Because of the lumen design with a larger diameter and a higher lumen openness yield than the PT MNs discussed in Chapter 3, HNL MNs are expected to exhibit a lower fluid resistance. Therefore, for PT MNs, the fluid resistance of the lumens was not characterized.

To calculate the theoretical fluid resistance of a lumen, one needs to evaluate the Reynolds number (R_e) to determine the flow behavior in the lumen [145]:

$$R_e = \frac{\rho V d}{\mu} \quad \text{.....(3)}$$

where ρ, V, and μ is the density, average velocity, and viscosity coefficient of the fluid, respectively, and d is the diameter of a circular pipe. The average velocity of the water, V, was calculated as 0.943 m/sec from the volumetric flow rate of 1.0 ml/min divided by the cross-sectional area of a circular lumen with a radius of 75 μm [145]. Furthermore, with a d of 150 μm for a circular lumen, ρ of 998 Kg/m^3 and μ of 1.0×10^{-3} kg/(m-sec) for water at 1 atm and 20 ℃, the Reynolds number was estimated as 141.2. With a Reynolds number less than 1800, a fluid flow in a microtube is a laminar flow [146] and therefore the water flow in the lumen of an HNL MN is considered as a laminar flow. Moreover, the water flow is assumed to be a fully developed flow, denoting that the region studied is far enough from the entrance of the lumen that the velocity of the flow is completely axial [145]. The viscosity coefficient, μ, of water at 1 atm and 20 ℃ is non-zero, and therefore the effects of viscosity, which is a quantitative measure of a fluid's resistance to flow [145], cannot be neglected, leading to the assumption that the water flow in an lumen is a viscous flow [147]. Since the density of water increases only one percent when the pressure is increased by a factor of 220 [145], the density variation inside the water as it flows is assumed to be negligible and therefore the water is an incompressible fluid [145, 147].

With the assumptions of a laminar, fully developed, viscous, and incompressible flow, the Poiseuille equation is valid [145, 148]. Theoretical calculation of the fluid resistance of a lumen was carried out using the Poiseuille equation [145],

$$\Delta P = \frac{128\mu L Q}{\pi d^4} \quad \text{.....(4)}$$

where ΔP is the fluid pressure, Q is the volumetric flow rate, μ is the viscosity coefficient of the fluid, L and d are the length and the diameter of the fluid channel, respectively. The length of the fluid channel consists of the lengths of the lumen in the MN shaft (590 μm) and in the baseplate (310 μm). With a Q of 1.0 ml/min, μ of 1.0×10^{-3} Pa-sec for water at 20 ℃, L of 900 μm, and d of 150 μm, the fluid pressure was calculated to be 1210 Pa, resulting in a theoretical fluid resistance of 1210 Pa/(ml/min).

The fluid resistance of a lumen was empirically determined using a custom fluid system. The custom fluid system involved a three-way fluid adapter. One opening of the adapter was connected to a 10 ml syringe through tubing. The syringe was filled with water and driven by a syringe pump at a constant flow rate of 1.0 ml/min. Another opening of the adapter was directly connected to a manometer (DigiMano 220, Netech, Farmingdale, NY, USA), which measured the fluid pressure. The last opening was connected to the back of the baseplate of an HNL MN through tubing. Initially the tested HNL MN was not attached to the tubing. With a constant flow rate of 1.0 ml/min from the syringe pump, the fluid pressure at the adapter was negligible since it was below the accuracy of the manometer. With the HNL MN attached to the tubing, the fluid pressure

at the adapter increased to 5600 Pa. Therefore, with a flow rate of 1.0 ml/min, the fluid resistance was 5600 Pa/(ml/min).

Although higher than theoretically predicted, it is instructive to compare this empirical result with the pressure required to inject fluid through hollow MNs into skin *in-vivo*. The fluid pressure required for saline injection into live human skin through a glass hollow MN at a flow rate of 1.0 ml/min was empirically characterized to be 10-80 psi (70-550 kPa) [149]. Therefore, the fluid pressure introduced by an HNL MN is negligible in comparison to the required pressure for fluid injection through MNs into live human skin at the flow rate of interest, i.e. 1.0 ml/min.

The deviation of empirical estimation from the theoretical calculation involves the validity of the assumption of a fully developed flow, which denotes that the region studied is far enough from the entrance of the lumen. The region is considered far enough from the lumen entrance when the distance is larger than the entrance length, L_e, [145]

$$\frac{L_e}{d} \approx 0.06 R_e \quad \text{.....(5)}$$

where d is the diameter of the fluid channel and R_e is the Reynolds number. With a d of 150 μm and R_e of 141.2, the entrance length was calculated as 1270 μm. Since the length of an HNL MN lumen is 900 μm and thus shorter than the entrance length, the water flow in the lumen is not fully developed, resulting in an additional fluid resistance [145]. Furthermore, there are two local losses at the entrance of the lumen: entrance loss and sudden contraction loss [145]. The two local losses are caused by local turbulent eddies

that result in energy dissipation and increased fluid resistances [150] and characterized by a loss coefficient [145],

$$K = \frac{2\Delta P}{\rho V^2} \quad \text{.....(6)}$$

where ΔP is the additional fluid pressure, ρ and V are the density and average velocity of the fluid, respectively. The entrance loss depends on the entrance geometry, and with a right-angled lumen entrance the loss coefficient is 0.5 [145]. The sudden contraction loss is a result of the fluid flowing from wide tubing to a narrow MN lumen. Since the tubing diameter is 4 mm and the lumen diameter is 150 μm, the loss coefficient of the sudden contraction loss is 0.42 [145]. With a total loss coefficient of 0.92, ρ of 998 Kg/m^3, and V of 0.943 m/sec, the additional fluid pressure is calculated as 410 Pa, leading to an additional fluid resistance of 410 Pa/(ml/min) at a flow rate of 1.0 ml/min.

4.4.5 Fluid Delivery into Excised Porcine Skin

A preliminary injection test was performed manually using a custom single-HNL-MN injection system, as shown in Figure 78, with excised porcine skin. To construct the custom injection system, an HNL MN with its surrounding baseplate was cut from an HNL MN array using a razor blade. A syringe cap was drilled at its center to open a fluid channel through the cap. The MN sample was affixed to the syringe cap with the opening of the MN lumen aligned within the center opening of the syringe cap. The syringe cap was then directly connected to a 10 ml syringe filled with dye.

To inject the dye into skin, the syringe was held perpendicularly to the skin surface by hand and then moved toward the skin to insert the HNL MN into skin. Following the insertion, thumb pressure was applied to the syringe plunger to drive the dye into skin through the HNL MN. Thumb pressure was applied for 10 seconds to ensure injection and subsequent diffusion of the dye in the VE. The pressure was then removed from the syringe plunger, followed by the retraction of the HNL MN from the skin.

Following the test, the skin was inspected under an optical microscope. An optical micrograph of the top view of the insertion/injection site on the skin is shown in Figure 79. The opening in the SC was caused by successful insertion of the HNL MN into skin. A manual cross-sectional cut using a scalpel was performed to inspect the cross section of the skin at the insertion/injection site. The cut was performed on a vertical plane in Figure 79 at the insertion/injection site, and the cross section of the skin was examined under an optical microscope from the right side in Figure 79. An optical micrograph of the bird's-eye view of the cross section of the skin at the insertion/injection site is shown in Figure 80. The red dashed line in Figure 80 denotes the stratum corneum layer. The injected dye underneath the SC can be clearly identified in Figure 80. The manual cross-sectional cut using a scalpel at the insertion/injection site may distort the skin tissue because of the friction between the scalpel and the skin tissue during the cut. Therefore, the dimension of the region of dye diffusion into the skin tissue shown in Figure 80 may not represent accurately the dimension of that region immediately following the fluid injection of the HNL MN into skin. The skin tissue underneath the SC was stained by the dye, as shown in Figure 79 and Figure 80, indicating that with the HNL MN being inserted into skin, the

dye flowed through the lumen of the HNL MN and into the skin tissue underneath the SC, followed by dye diffusion into the skin tissue. This preliminary manual injection test suggested the potential use of HNL MNs for drug delivery into skin.

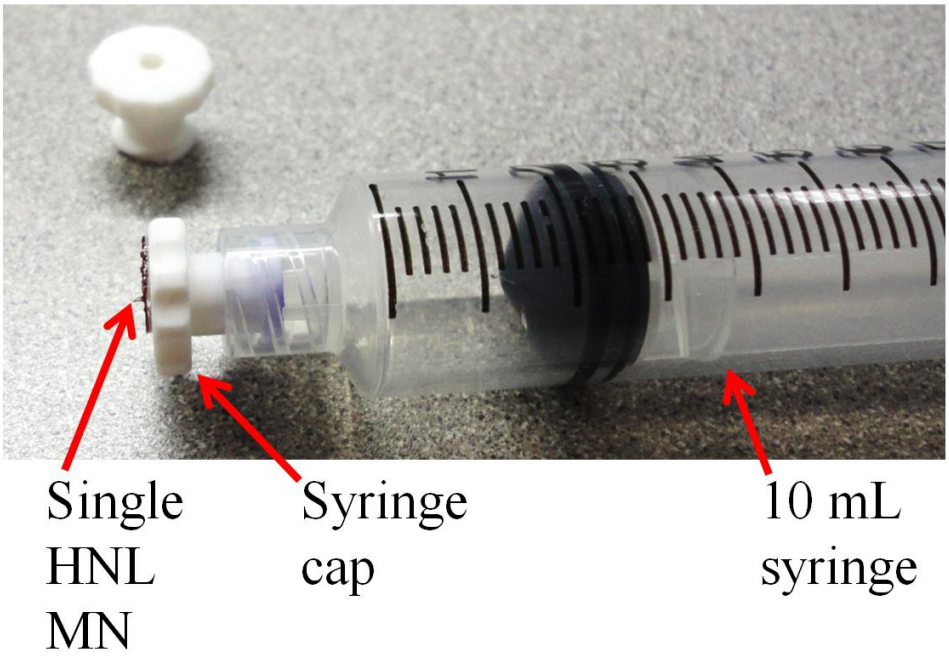

Figure 78. Optical image of the custom single-HNL-MN injection system. An HNL MN with its surrounding baseplate was attached to a center-drilled syringe cap, which was mounted to a 10 ml syringe. Another center-drilled syringe cap is shown in the upper left corner of this image.

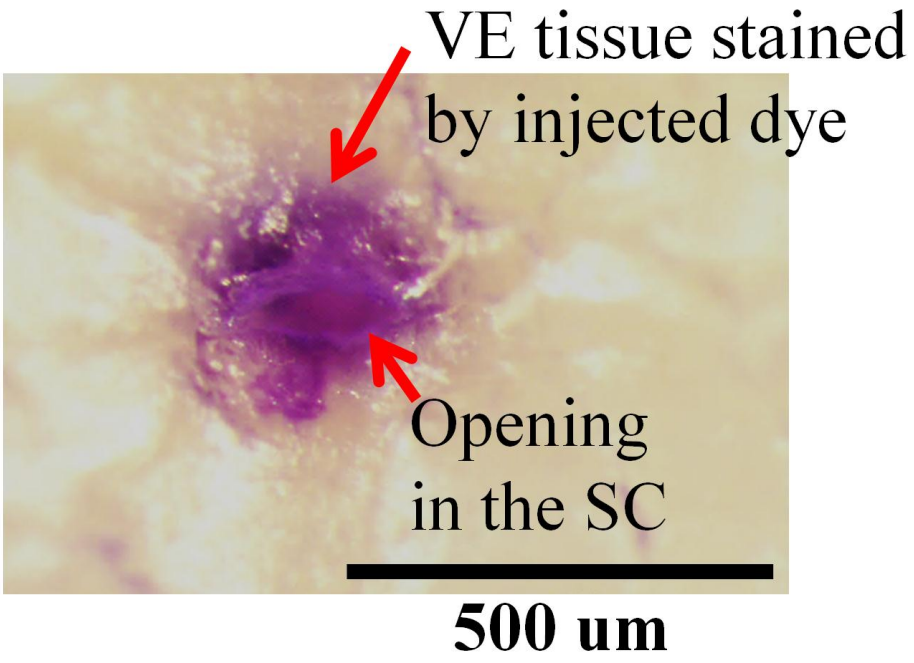

Figure 79. Optical micrograph of the top view of an insertion/injection site on the excised porcine skin following the insertion of an HNL MN and the injection of dye through the HNL MN. The opening in the stratum corneum (SC) was caused by the successful insertion of the needle, followed immediately by dye injection through the HNL MN. The injected dye stained the viable epidermis (VE) underneath the SC.

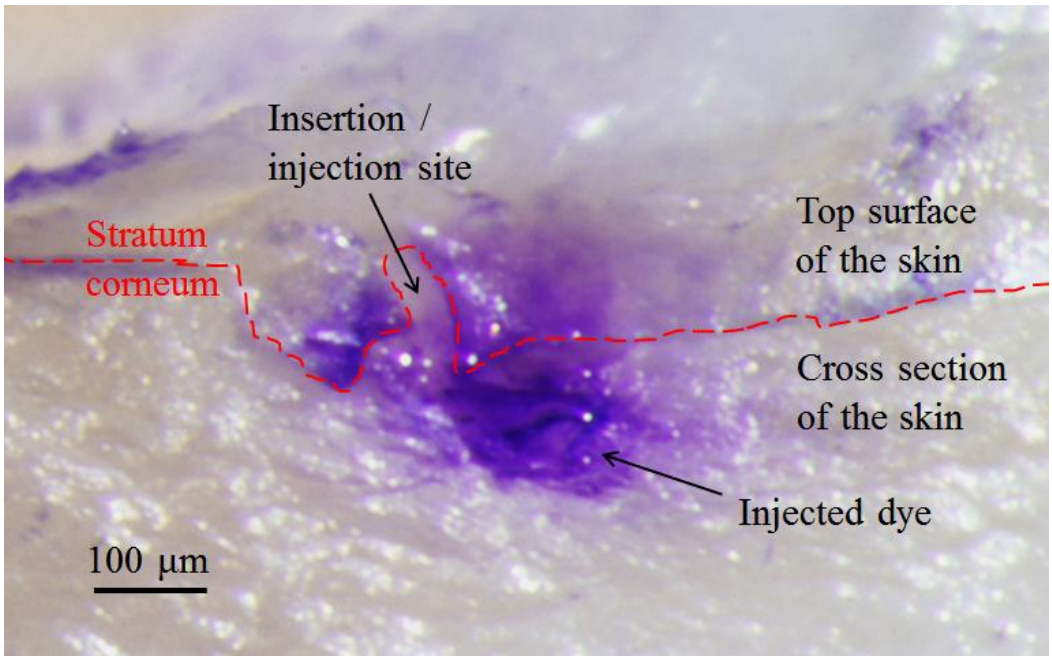

Figure 80. Optical micrograph of the bird's-eye view of the cross section of the insertion/injection site shown in Figure 79 following a manual cross-sectional cut using a scalpel.

4.5 Integration of Skin Adhesive Into A Microneedle Array

For drug delivery into skin through MNs, the required duration of MNs in direct contact with skin varies according to the delivery rate, required drug dosage, and targeted application. To achieve continuous drug delivery, MNs are required to remain in direct contact with skin over a period of time. One millimeter HMNs have been shown to successfully deliver insulin to human subjects with type-1 diabetes through the skin and subsequently to reduce the postprandial glucose level. [96] For insulin therapy to diabetic patients using an insulin pump, the cannula of the infusion set often remains inserted at the same insertion site for 48 to 72 hours. Because of saturation of the absorption tissues at the insertion site and the degradation of insulin in the infusion set, the infusion set needs to be replaced with a new one afterward. [151] Therefore, for potential insulin therapy using HMNs, it is desired that HMNs remain in direct contact with skin for up to 72 hours. Integration of skin adhesive into MN patch designs is essential for continuous drug delivery into skin. Following MN insertion into skin, in addition to the skin adhesive covering the entire MN array over on the skin, skin adhesive that is between the MN baseplate and the skin as shown in Figure 81 increases the total adhesion, yields enhanced resistance to movement between MNs and the skin, and may eliminate aqueous drug leaking onto the skin surface.

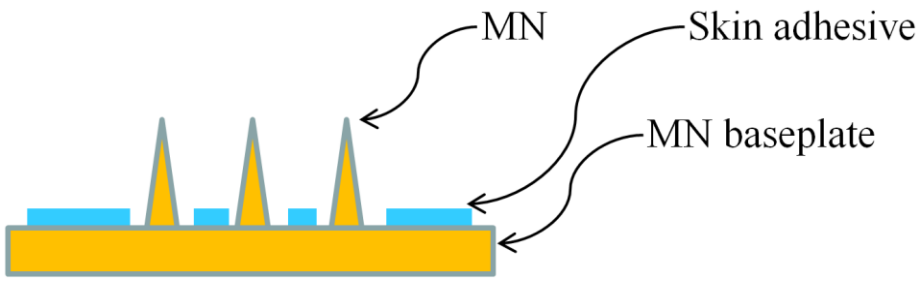

Figure 81. A schematic illustration of an MN array with skin adhesion on the baseplate. Following insertion, the skin adhesive secures the MN array to the skin in direct contact.

The process flow for integration of skin adhesive into an MN array is shown in Figure 82. Commercially available skin adhesive tapes commonly consist of a layer of skin adhesive and a releaser layer, as shown in Figure 82(a). [152] The skin adhesive patch is patterned so that the skin adhesive covers the baseplate and not the MNs (Figure 82(b)). Openings of the patterned skin adhesive patch are aligned with the MNs (Figure 82(c)), followed by application of the skin adhesive patch onto the baseplate (Figure 82(d)). The release layer is removed from the skin adhesive (Figure 82(e)), resulting in a baseplate covered by skin adhesive (Figure 82(f)).

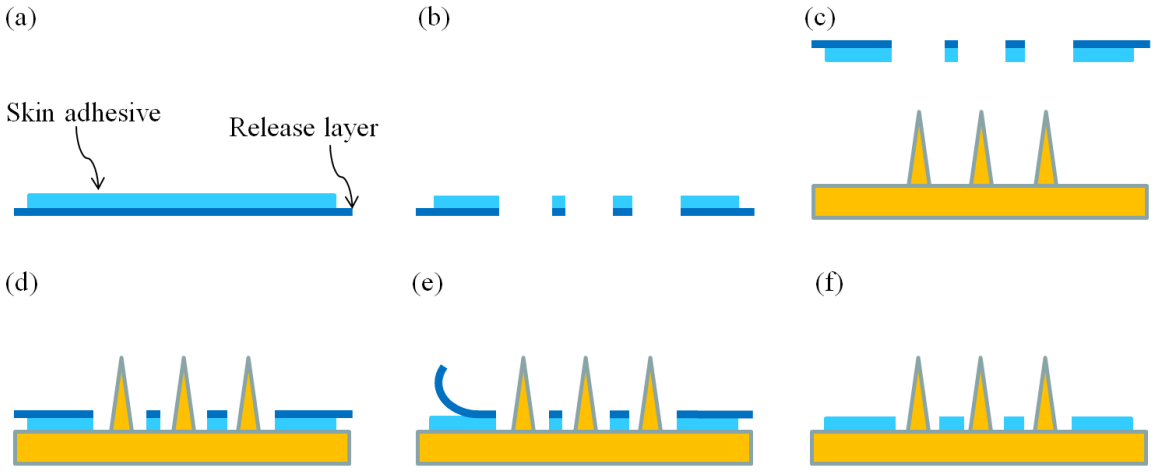

Figure 82. A schematic illustration of the process flow for integration of skin adhesive into an MN baseplate.

To select adhesive for transdermal drug delivery system, there are several factors that need to be taken into consideration, including biocompatibility and formulation compatibility [153]. Biocompatibility requires the adhesive to be biologically inert, non-irritating, non-sensitizing to skin, and with no systemic toxicity. Formulation compatibility requires that the adhesive does not induce drug or excipient degradation, does not react with the drug and other components, and maintains stability and functional properties, e.g., adequate tack, skin-adhesion, and cohesive strength. For preliminary study of integration of skin adhesive into an MN array, a high-tack medical transfer adhesive on an extended liner (3M Medical Specialties #1504XL, 3M Health Care, St. Paul, MN, USA) is selected. The skin adhesive tapes consists of a 110-μm-thick adhesive made of a 3M proprietary synthetic rubber/resin system and a 90-μm-thick release liner made of bleached kraft paper coated by silicone release on both sides.

To pattern the skin adhesive shown in Figure 82(b) is a critical process step in the integration of skin adhesive into an MN array. Several rapid mechanical patterning approaches to remove the unwanted portion of the skin adhesive tape were performed, including using a dermal biopsy punch of one millimeter in diameter, an aluminum milling machine, a paper punch, and 25-gauge hypodermic needle. All these mechanical approaches involve physical contact between the piercing part of a tool and the skin adhesive. Because of the nature of adhesive the skin adhesive often adheres to the piercing part and is subsequently removed from the release layer with the removal of the piercing part from the tape. Therefore, a contact-less patterning approach is desired for the skin adhesive patterning.

Laser micromachining is a contact-less patterning approach and therefore selected to pattern the skin adhesive. A CO_2 laser (LS500XL, Gravotech, Inc., Duluth, GA, USA) with a principal wavelength of ~10.6 μm and a beam size of ~200 μm was used to remove a 6×6 array of circles with a diameter of 800 μm and a center-to-center distance of 1430 μm from the skin adhesive tape. Figure 83(a) shows an optical micrograph of the top view of the patterned skin adhesive tape with skin adhesive on the top and a release layer on the bottom. Figure 83(b) shows a magnified view of Figure 83(a), and the diameter of patterned circles is ~805 μm, ranging from 800 μm to 810 μm.

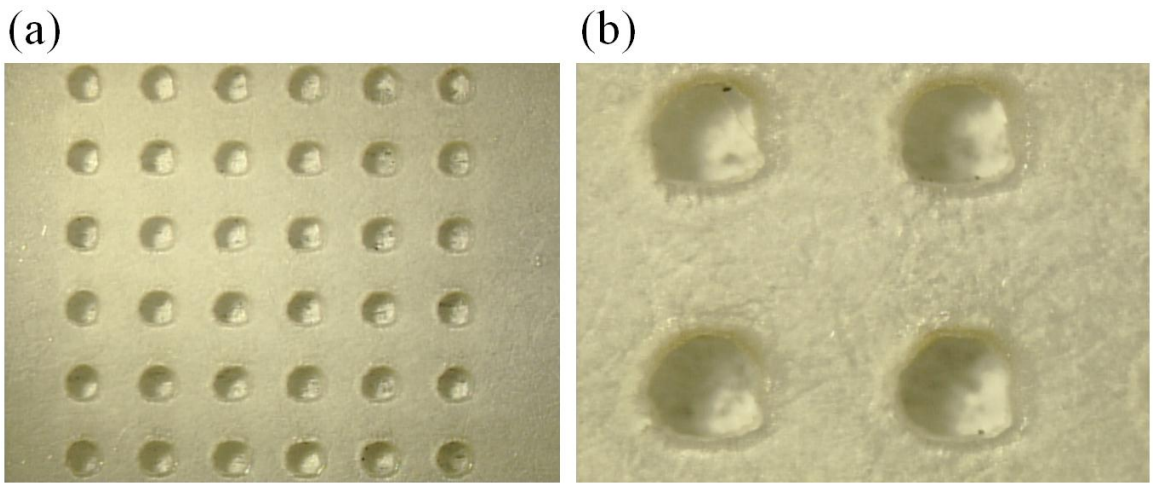

Figure 83. (a) An optical micrograph of the top view of the patterned skin adhesive tape with skin adhesive on the top and a release layer on the bottom. A 6×6 array of circles is removed from the tape. (b) A magnified view of (a) showing the details of the perimeters of the circles in a 2×2 array.

The alignment and application of the patterned skin adhesive tape to an MN array (Figure 82(c) and (d)) was performed using a probe station (Signatone Corp., Gilroy, CA, USA) shown in Figure 84. The probe station is equipped with a movable sample stage and an optical microscope for alignment as well as a C-shape chunk that can be vertically

shifted by the control of a level. The skin adhesive tape was held by a custom adhesive tape holder. Figure 85(a) shows an optical image of the bird's-eye view of the backside of the custom adhesive tape holder, consisting of a corrugated fiberboard with a 50 mm × 50 mm opening at the center and a transparent release liner (1022 release liner, 3M Health Care, St. Paul, MN, USA) with a 20 mm × 20 mm opening aligned to the opening of the fiberboard. The fiberboard and the release liner were clipped together using a binder clip. The skin adhesive tape was attached to the 1022 release liner of the custom adhesive tape holder as shown in Figure 85(b). To align the patterned skin adhesive tape to an MN array, the custom adhesive tape holder was slid into the groove on the inside perimeter of the C-shape chunk with the backside on the bottom. With an MN array placed at the center of the sample stage, the alignment was performed through the optical microscope using the X, Y, and theta turning knobs to move and align the 6×6 MN array with the 6×6 array of circular openings on the skin adhesive tape. Figure 86 shows an optical image of the bird's-eye view of the alignment setup with the custom adhesive tape holder slid into the chunk groove and an MN array placed at the center of the sample stage. Following the completion of the alignment, the C-shape chunk was lowered to bring the skin adhesive side of the patterned tape in direct contact with the MN array. The skin adhesive tape was subsequently cut using a razor blade around the perimeter of the MN array to release the MN array. A pair of flat-headed tweezers was used to apply gentle pressure onto the release layer of the skin adhesive tape to enhance the adhesion between skin adhesive and the baseplate.

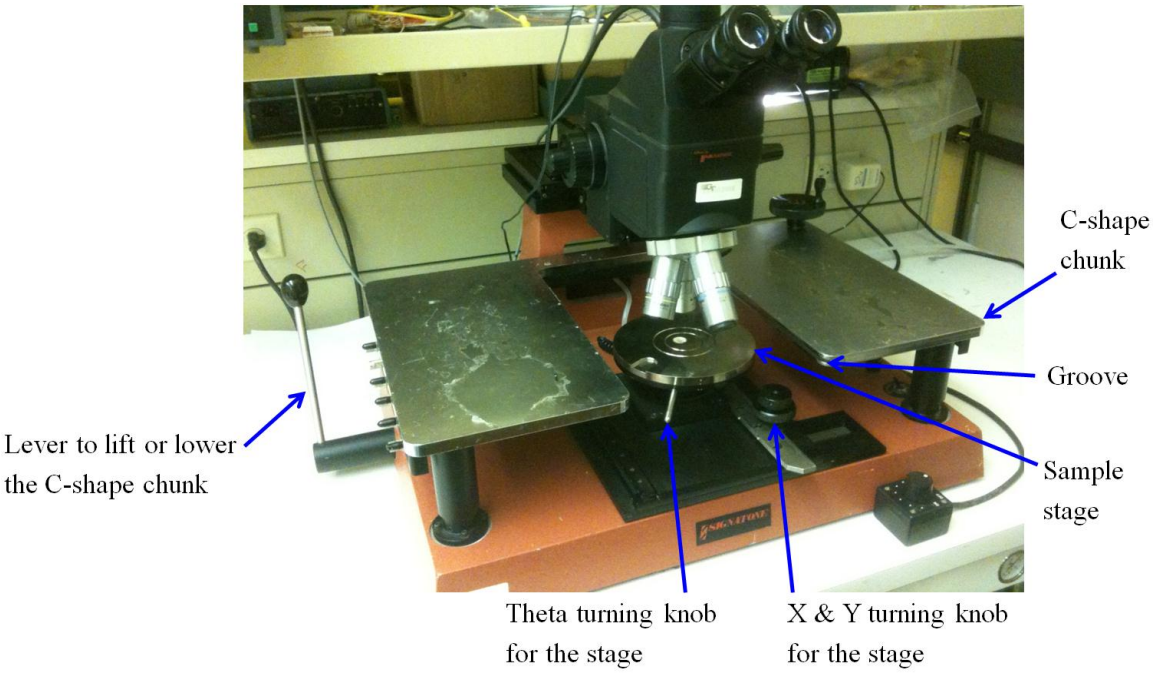

Figure 84. An optical image of the probe station used for alignment and application of the skin adhesive tape to an MN array.

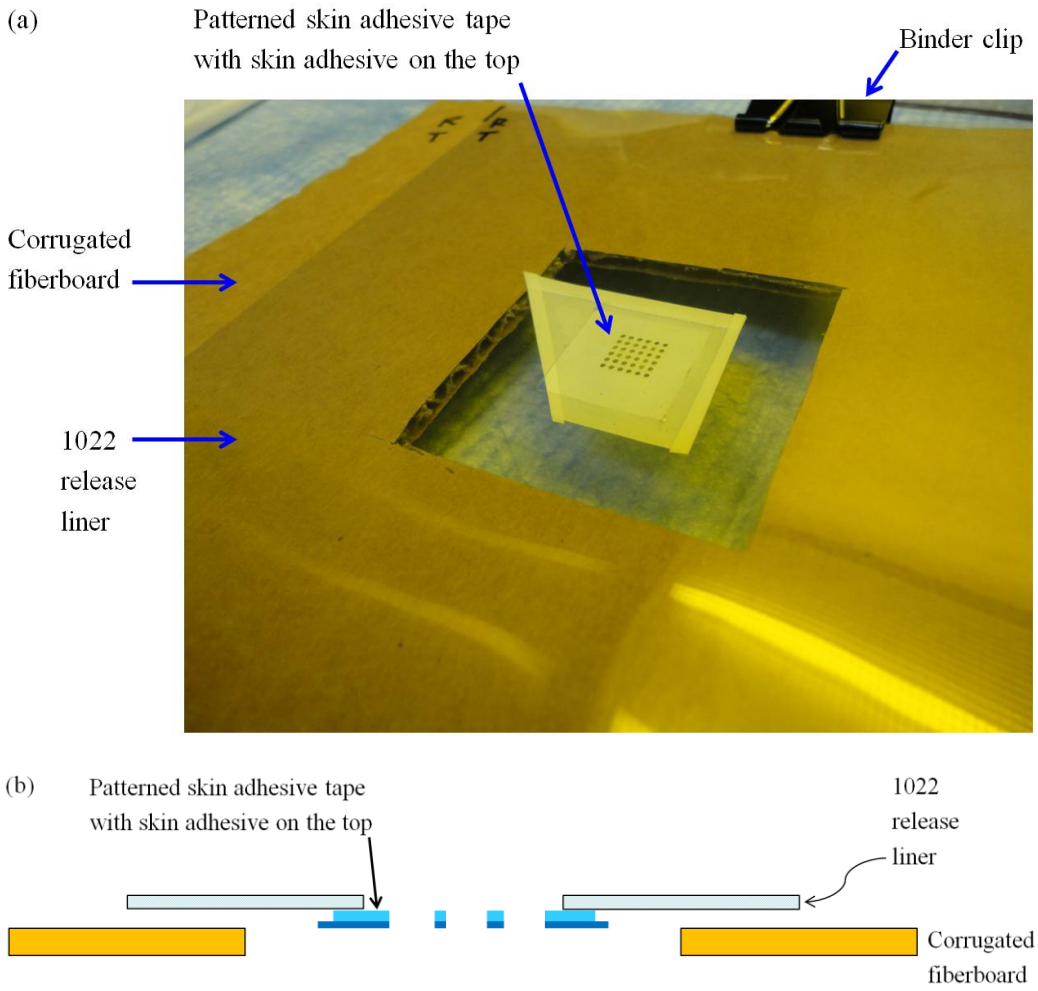

Figure 85. (a) An optical image of the bird's-eye view of the backside of a custom adhesive tape holder with the patterned skin adhesive tape. The 1022 release liner is transparent. (b) A schematic illustration of the cross-sectional view of the custom adhesive tape holder with the patterned skin adhesive tape. The backside of the custom holder is on top.

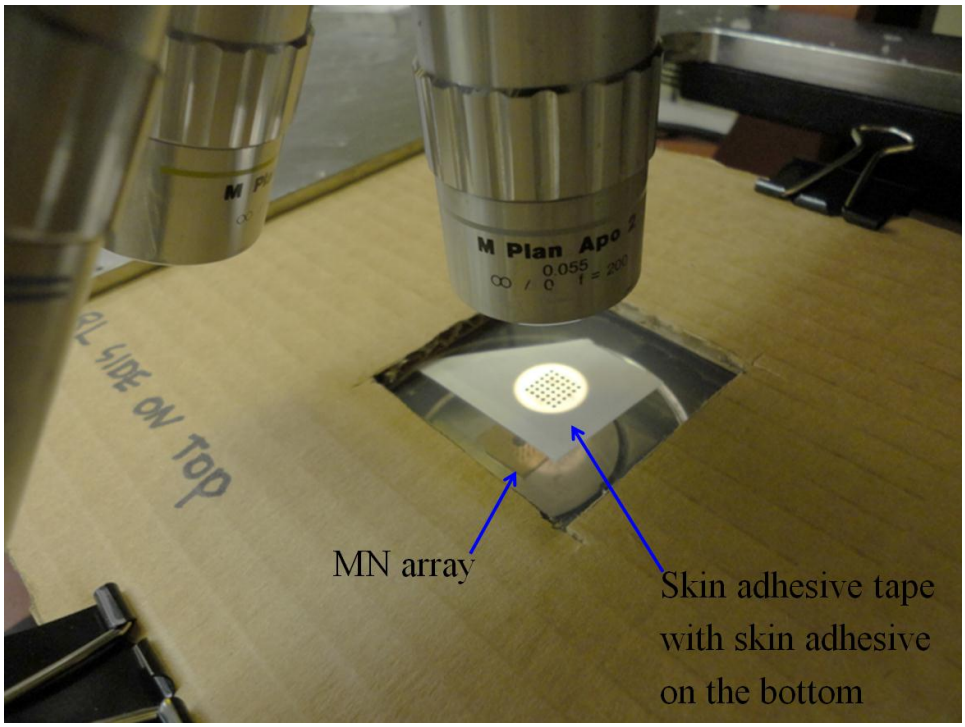

Figure 86. An optical image of the bird's-eye view of the alignment setup with the custom adhesive tape holder slid into the chunk groove and an MN array placed at the center of the sample stage.

Figure 87 shows two optical micrographs of the MN array following the application of the skin adhesive tape onto the baseplate of the MN array. The cross-section of the MN array with the skin adhesive tape is illustrated in Figure 82(d). For the feasibility study of the integration of skin adhesive into an MN array, an MN array fabricated with initial, unoptimized process parameters was used. The release layer of the skin adhesive tape was subsequently removed using a pair of flat-headed tweezers. Figure 88 shows two optical micrographs of the finished MN array with the baseplate covered by skin adhesive. The cross-section of the finished MN array is illustrated in Figure 82(f).

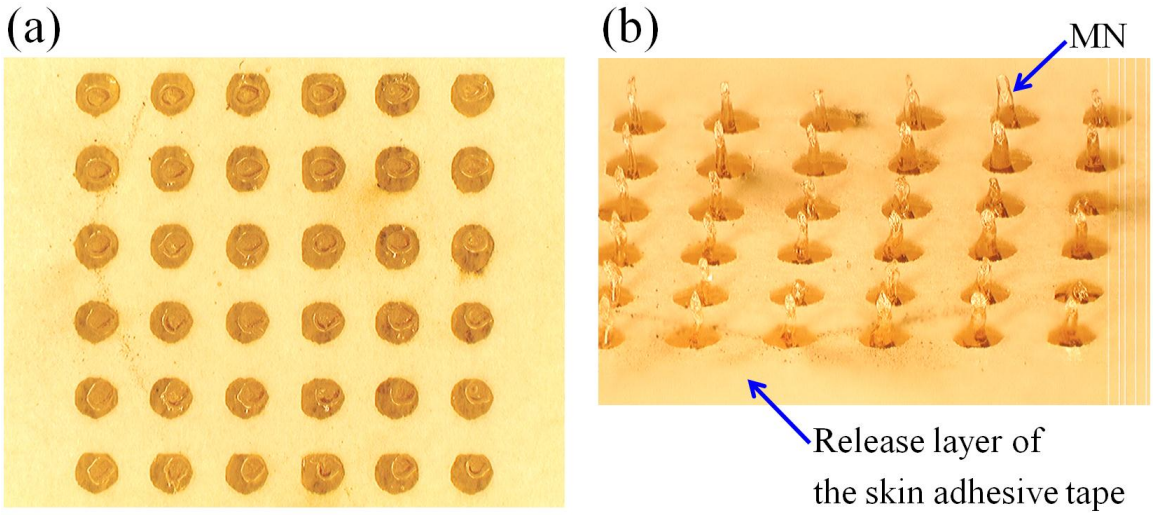

Figure 87. (a) An optical micrograph of the top view of a 6×6 MN array with the baseplate covered by the patterned skin adhesive tape. The release layer is on top of the skin adhesive of the patterned adhesive tape. (b) An optical micrograph of the bird's-eye view of the 6×6 MN array.

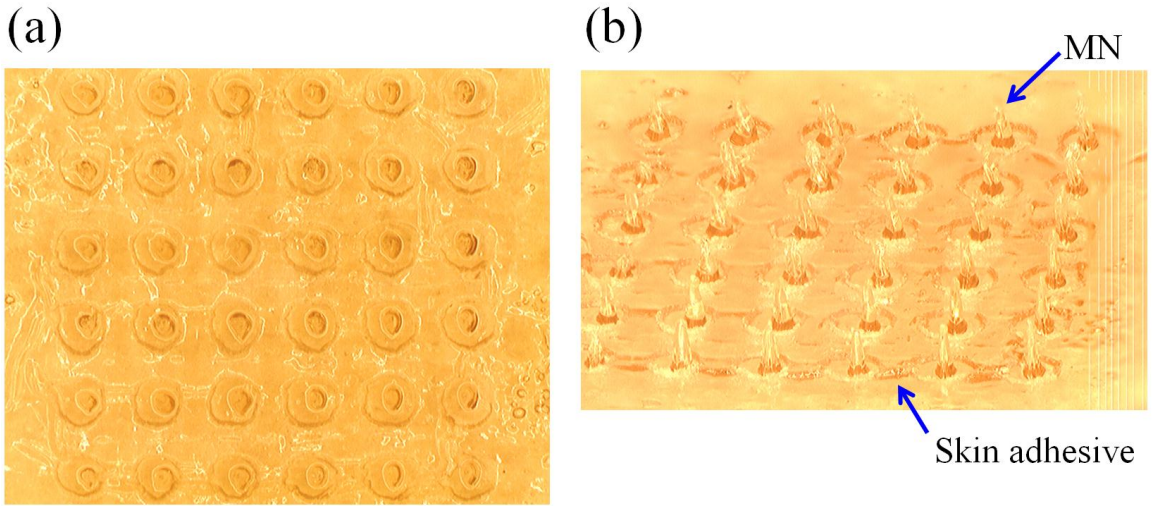

Figure 88. (a) An optical micrograph of the top view of the 6×6 MN array with the baseplate covered by the skin adhesive following the removal of the release layer of the patterned adhesive tape. (b) An optical micrograph of the bird's-eye view of the 6×6 MN array.

4.6 Chapter Conclusion

Conventional hypodermic needles have two key structural characteristics: a sharp beveled tip and a large side-terminated lumen. The sharp beveled tip reduces insertion force and pain perceived by patients, while the large side-terminated lumen provides a large fluid uptake area in the skin and reduces susceptibility to tissue clogging during insertion. Integration of these two key characteristics of HNs into MN design can potentially enhance MN performance. This work demonstrates the incorporation of these key structural features into polymer MNs in a batch-processing-compatible manner by exploiting a combination of UV lithography and micromolding.

This 6 × 6 HNL MN array consists of 1 mm tall high-aspect-ratio hollow SU-8 MNs with sharp beveled tips and 150 μm diameter side-opened lumens as well as a baseplate. A two-dimensional lithographic mask pattern and the topography of the micromold are utilized simultaneously to define the geometry of the beveled tip and the position of the lumen. The needle array was packaged and characterized for skin penetrability and fluidic functionality. A manual insertion test with excised porcine skin showed that the 6 × 6 HNL MN array was successfully inserted into skin with a successful insertion rate of 97% and no fracture or tip bending was observed under an optical microscope following the insertion. A microfluidic channel test indicated that at least 85% of the lumens were open.

Mechanical insertion characterization of HNL MNs was performed using excised porcine skin as a substrate and automatic force-displacement test stations. The insertion force of an HNL MN was determined to be 0.275 N, which is comparable to the insertion force of 0.284 N for a conventional 26G HN, indicating that HNL MNs exhibit

comparable insertion performance to conventional 26G HNs. In comparison to the insertion force of 2.4 N for PT MNs discussed in Chapter 3, HNL MNs exhibit superior insertion performance. With comparable tip diameters of PT MNs and HNL MNs, the approximately one-order-of-magnitude reduction in insertion force indicated that the tip geometry is an important factor in the insertion performance of MNs. With the fracture force of an HNL MN higher than 50 N and the insertion force of 0.275 N with excised porcine skin, the margin of safety for successful needle insertion prior to needle fracture is at least 180 for HNL MNs, an approximately fivefold increase compared to PT MNs.

A preliminary manual injection test was performed using an HNL MN attached to a syringe to insert and then inject fluid into excised porcine skin. Following the test, staining of the VE tissues underneath the SC by the injected dye from the syringe was observed under an optical microscope in addition to an opening of the SC created by successful insertion of the HNL MN into skin. This demonstrated that the delivery of fluids into skin can be achieved through an HNL MN following the insertion into skin. Furthermore, the fluid resistance of an HNL MN was empirically estimated to be 5600 Pa/(ml/min), which is negligible in comparison to the required fluid pressure for saline injection into live human skin at a flow rate of 1.0 ml/min.

Medical transfer skin adhesive was patterned and applied onto the baseplate between MNs within an HNL MN array to increase the adhesion between the needle array and the skin for continuous drug delivery.

In this chapter, HMNs fabricated using a potential batch-manufacturable process are presented with comparable insertion force to HNs and a high margin of safety for

needle fracture using skin as a substrate. With the successful demonstration of fluid injection into skin, HNL MNs have the potential for drug delivery into skin.

CHAPTER 5

CONCLUSIONS

5.1 Summary of This Research

The aim of this research is to demonstrate that micromachined hollow polymer needle arrays fabricated using UV lithography into micromolds, a potential batch-manufacturable process, can exhibit comparable insertion and injection performance to conventional hypodermic needles for drug delivery into skin.

In Chapter 3, a dual-exposure-and-single-development process flow is proposed for the fabrication approach of UV lithography into micromolds to construct a pyramidal-tip hollow microneedle array with a baseplate. Following several process improvement breakthroughs, a 10×10 array of hollow SU-8 microneedles measuring 825 μm in height, 400 μm in width and with a lumen of 120 μm in diameter is successfully demonstrated. The tip diameter of microneedles ranges from 15 μm to 25 μm. Mechanical characterization shows the pyramidal tip of the fabricated microneedles fractures against a rigid surface with a driving force of 12.0 ± 0.8 N. The insertion force of single needles characterized using excised porcine skin as a substrate is 2.4 ± 1.2 N. Moreover, the application of the 90 N force on a single needle causes minor tip deformation with no fracture observed under an optical microscope, leading to a margin of safety higher than 37. Nevertheless, the high insertion force of 2.4 N per needle may cause a significant concern when a large number of needles are required to insert into skin for drug delivery.

Conventional hypodermic needles have two key structural characteristics: a sharp beveled tip and a large side-terminated lumen. The sharp beveled tip reduces insertion

force and pain perceived by patients, while the large side-terminated lumen provides a large fluid uptake area in the skin and reduces susceptibility to tissue clogging during insertion. Integration of these two key characteristics of hypodermic needles into microneedle design can potentially enhance microneedle performance. To reduce the insertion force and to incorporate the two key characteristics of hypodermic needles into the design of microneedles, a new needle tip design, namely the hypodermic-needle-like design, is presented in Chapter 4. With the change from a pyramidal mold to a beveled one, the geometry of the microneedle tip can be optimized three-dimensionally with two dimensions from the design of the photomask pattern and one dimension from the slope angle of the beveled mold. A 6 × 6 array of hypodermic-needle-like microneedles of 1 mm in height, approximate 350 μm in width, and with a lumen of 150 μm in diameter is demonstrated with successful insertion of the needle array into skin and an 85% lumen openness yield. The insertion force is significantly reduced by an order of magnitude with the new needle tip design and is 0.275 ± 0.113 N per needle, comparable to that of hypodermic needles, i.e., 0.284 ± 0.059 N. The hypodermic-needle-like microneedles exhibit a margin of safety of 180 for successful needle insertion into skin prior to needle fracture. A successful manual fluid injection into skin using single microneedle is demonstrated.

Therefore, micromachined hypodermic-needle-like polymer needle arrays presented in this dissertation are fabricated using UV lithography into micromolds, a potential batch-manufacturable process, and exhibit comparable insertion performance to conventional hypodermic needles. Preliminary injection capability into skin is also

demonstrated with a hypodermic-needle-like microneedle. In conclusion, the aim of this research is substantially achieved.

5.2 Contributions of This Dissertation

This dissertation demonstrates the incorporation of key structural features of conventional hypodermic needles into polymer microneedles in a batch-processing-compatible manner by exploiting a combination of UV lithography and micromolding, followed by extensive characterization to confirm the comparable performance of these polymer microneedles to conventional hypodermic needles. Four substantial contributions as a result of this research are summarized as follows:

[1] Demonstration of the feasibility of the research hypothesis: For the manufacturing of hollow microneedles appropriate for single-use devices, a polymer-based fabrication approach using UV lithography into micromolds is highly desired. The hypothesis of this research is that micromachined hollow polymer needles fabricated using UV lithography into micromolds can exhibit comparable insertion and injection performance to conventional hypodermic needles. A dual-exposure-and-single-development process flow is initially designed. Various process optimization and improvements are achieved. A 6 × 6 hypodermic-needle-like microneedle array consisting of 1 mm tall SU-8 needles with a sharp beveled tip and a large side-terminated lumen with a baseplate is demonstrated, and fabricated microneedles are characterized extensively to confirm their comparable insertion and injection performance to conventional hypodermic needles. Therefore, the first contribution of this dissertation is substantial verification of the hypothesis of this research, affirming the feasibility of using a batch-processing-compatible microfabrication approach to construct polymer

microneedles that exhibit comparable insertion and injection performance to conventional hypodermic needles.

[2] Development of UV lithography-based microfabrication for 1 mm tall complex three-dimensional structures: SU-8 structures fabricated using UV lithography with a height of 1.5 mm and an aspect ratio of 15 have been previously demonstrated. [71] Nevertheless, these structures are of simple and open features that have no enclosed feature or pattern, e.g., a hollow channel through the structure. Compared to the construction of these simple and open features, a hollow channel through the structure may raise additional fabrication difficulty given the rationales discussed in Section 3.3. To our knowledge, this research demonstrates the first out-of-plane 1 mm tall SU-8 microneedles with a verified open lumen through the structure and with a functional needle tip fabricated using conventional UV lithography. Moreover, various critical process parameters / conditions are identified, including softbake conditions, UV exposure dosage, and internal UV reflection at the interface, and discussed extensively in Section 3.3, Subsection 3.4.4, and Subsection 4.3.2. Optimization and improvements of these process parameters / conditions are implemented to confirm their efficacy.

[3] Quantitative verification of tip geometry optimization in the insertion performance of microneedles: The tip diameter of microneedles has been shown to significantly affect the required insertion force of the needle, and the quantitative relation between the tip diameter and the insertion force has been previously determined. [28, 129, 142] Nevertheless, no other design parameter of the needle tip has been reported quantitatively to affect or reduce the insertion force of microneedles into skin. As a pioneering effort, this research provides the first quantitative information on the insertion

force in the optimization of the tip geometry. With the change of tip geometry from a pyramidal shape to a hypodermic-needle-like one and the decrease of the tip angle from 70° to 35°, the insertion force per needle is reduced from 2.40 N to 0.275 N, an approximate one-order-of-magnitude reduction, indicating that the tip geometry is an important factor in utilization of microneedles in the applications of drug delivery into skin. Moreover, the fluid resistance of a hypodermic-needle-like microneedle is empirically determined and shown to be negligible in comparison to the required pressure for fluid injection into live human skin.

[4] Demonstration of the inter-needle integration of skin adhesive into a microneedle array: To achieve continuous drug delivery into skin, microneedles are required to remain in direct contact with skin over a period of time. Hence, integration of medical skin adhesive into the design of microneedle patches is essential for continuous drug delivery into skin. In addition to the skin adhesive covering the entire needle array over on the skin, skin adhesive that is between the needle baseplate and the skin may increase the total adhesion, yield enhanced resistance to movement between microneedles and the skin, and eliminate aqueous drug leaking onto the skin surface. This research demonstrates the first integration of skin adhesive onto the between-needle baseplate, i.e., the substrate between microneedles in a needle array, in a 6×6 microneedle array with no interference in needle insertion into skin.

5.3 Suggestions for Future Work

This research demonstrated that hypodermic-needle-like polymer microneedle arrays can be fabricated using UV lithography into micromolds and that single fabricated

microneedles exhibit comparable insertion performance to conventional hypodermic needles and the capability of fluid injection into skin.

Characterization of the insertion and fracture force of HNL MNs was performed using excised porcine skin as a substrate. To investigate the fracture performance of HNL MNs in the worst scenario, fracture force characterization can be carried out using a rigid surface as a substrate. Similar fracture force characterization for PT MNs was discussed in detail in Subsection 3.5.3.

A preliminary manual injection test was performed using an HNL MN attached to a syringe to insert and then inject fluid into excised porcine skin. Quantitative characterization of the fluid injection, such as the applied pressure as a function of the fluid volume delivered into skin at different flow rates, can be performed to further examine the injection performance of HNL MNs. Characterization can be done for fluid volume up to 1 mL, which is the volume of a typical single insulin injection, and for flow rates up to 1 mL/min. Similar characterization of fluid injection through microneedles into skin was discussed in detail in [149].

A number of studies have suggested that processed SU-8 is potentially a biocompatible material. Various treatments of SU-8 have been demonstrated to further enhance the intrinsic biocompatibility performance of SU-8. Nevertheless, medical device regulatory requirements must be met prior to the marketing of any medical device to the general public. ISO 10993 physicochemical and biocompatibility tests have been adopted by the FDA. In a guidance memorandum distributed by the FDA and entitled "Use of International Standard ISO-10993, 'Biological Evaluation of Medical Devices Part 1: Evaluation and Testing,'" required biological evaluation tests are identified

according to the body contact and contact duration of the medical device. [154] For potential insulin therapy using HMNs, HMNs may remain inserted in the skin for up to 72 hours. Therefore, according to the Table 1 entitled “Initial Evaluation Tests for Consideration” in the guidance memorandum, six evaluation tests may be required, including cytotoxicity, sensitization, irritation or intracutaneous reactivity, systemic toxicity, subchronic toxicity, and implantation. Specifications on these evaluation tests can be found in the corresponding ISO 10993 standards [155] with additional information in the guidance memorandum.

For microneedles to become practical devices for drug delivery into skin, the packaging of microneedles needs to be thoroughly studied. The aims of the microneedle packaging design are to provide protection for microneedles and drugs, to enable needle insertion and drug injection into skin, and to remain in direct contact with skin for continuous drug delivery. A typical microneedle package consists of microneedles, a drug reservoir, skin adhesive, a protective structure, and a cover. Mechanical components and/or mechanisms that enable needle insertion and drug injection into skin need to be taken into consideration in the package design. Co-fabrication of microneedles and the package can be explored and studied. Moreover, device characterization of microneedle packages can include inspection of complete insertion of an HNL MN array into skin, verification of continuous drug delivery into skin without leakage, and evaluation of adhesion of the package to the skin over a period of time.

REFERENCES

[1] M. R. Prausnitz, "Microneedles for transdermal drug delivery," *Advanced Drug Delivery Reviews,* vol. 56, no. 5, pp. 581-587, March 2004.

[2] A. Arora, M. R. Prausnitz, and S. Mitragotri, "Micro-scale devices for transdermal drug delivery," *International Journal of Pharmaceutics,* vol. 364, no. 2, pp. 227-236, December 2008.

[3] R. F. Donnelly, T. R. Raj Singh, and A. D. Woolfson, "Microneedle-based drug delivery systems: microfabrication, drug delivery, and safety," *Drug Delivery,* vol. 17, no. 4, pp. 187-207, May 2010.

[4] S. M. Bal, Z. Ding, E. van Riet, W. Jiskoot, and J. A. Bouwstra, "Advances in transcutaneous vaccine delivery: do all ways lead to Rome?," *Journal of Controlled Release,* vol. 148, no. 3, pp. 266-82, December 2010.

[5] M. S. Gerstel and V. A. Place, "Drug delivery device," U.S. Patent 3,964,482, June 22, 1976.

[6] S. Hashmi, P. Ling, G. Hashmi, M. Reed, R. Gaugler, and W. Trimmer, "Genetic transformation of nematodes using arrays of micromechanical piercing structures," *Biotechniques,* vol. 19, no. 5, pp. 766-770, 1995.

[7] S. Henry, D. V. McAllister, M. G. Allen, and M. R. Prausnitz, "Microfabricated microneedles: A novel approach to transdermal drug delivery," *Journal of Pharmaceutical Sciences,* vol. 87, no. 8, pp. 922-925, 1998.

[8] M. R. Prausnitz, S. Mitragotri, and R. Langer, "Current status and future potential of transdermal drug delivery," *Nature Reviews Drug Discovery,* vol. 3, no. 2, pp. 115-24, February 2004.

[9] J. C. Birchall, R. Clemo, A. Anstey, and D. N. John, "Microneedles in clinical practice--an exploratory study into the opinions of healthcare professionals and the public," *Pharmaceutical Research,* vol. 28, no. 1, pp. 95-106, Jan 2011.

[10] J. A. Owen, J. Punt, and S. A. Stranford, *Kuby Immunology*. New York, NY: W. H. Freemand and Company, 2013, pp. 1-64, 141-186, 451-484.

[11] T. S. Kupper and R. C. Fuhlbrigge, "Immune surveillance in the skin: mechanisms and clinical consequences," *Nature Reviews Immunology*, vol. 4, no. 3, pp. 211-222, March 2004.

[12] M. del Pilar Martin, W. C. Weldon, V. G. Zarnitsyn, D. G. Koutsonanos, H. Akbari, I. Skountzou, J. Jacob, M. R. Prausnitz, and R. W. Compans, "Local response to microneedle-based influenza immunization in the skin," *mBio*, vol. 3, no. 2, pp. e00012-12, March/April 2012.

[13] M. Zaric, O. Lyubomska, O. Touzelet, C. Poux, S. Al-Zahrani, F. Fay, LeahWallace, D. Terhorst, BernardMalissen, S. Henri, U. F. Power, C. J. Scott, R. F. Donnelly, and A. Kissenpfennig, "Skin Dendritic Cell Targeting via Microneedle Arrays Laden with Antigen-Encapsulated Poly-d,l-lactide-co-Glycolide Nanoparticles Induces Efficient Antitumor and Antiviral Immune Responses," *American Chemical Society NANO*, vol. 7, no. 3, pp. 2042-2055, March 2013.

[14] J. M. Song, Y. C. Kim, E. O, R. W. Compans, M. R. Prausnitz, and S. M. Kang, "DNA vaccination in the skin using microneedles improves protection against influenza," *Molecular Therapy*, vol. 20, no. 7, pp. 1472-1480, July 2012.

[15] Q. Zhu, V. G. Zarnitsyn, L. Ye, Z. Wen, Y. Gao, L. Pan, I. Skountzou, H. S. Gill, M. R. Prausnitz, C. Yang, and R. W. Compans, "Immunization by vaccine-coated microneedle arrays protects against lethal influenza virus challenge," *Proceedings of the National Academy of Sciences of the U.S.A.*, vol. 106, no. 19, pp. 7968-73, May 12 2009.

[16] H. S. Gill, J. Soderholm, M. R. Prausnitz, and M. Sallberg, "Cutaneous vaccination using microneedles coated with hepatitis C DNA vaccine," *Gene Therapy*, vol. 17, no. 6, pp. 811-4, June 2010.

[17] P. Van Damme, F. Oosterhuis-Kafeja, M. Van der Wielen, Y. Almagor, O. Sharon, and Y. Levin, "Safety and efficacy of a novel microneedle device for dose sparing intradermal influenza vaccination in healthy adults," *Vaccine*, vol. 27, no. 3, pp. 454-9, Jan 14 2009.

[18] S.-O. Choi, "An electrically active microneedle electroporation array for intracellular delivery of biomolecules," Ph.D. Dissertation, School of Electrical and Computer Engineering, Georgia Institute of Technology, Atlanta, GA, 2007.

[19] M. J. Madou, *Fundamentals of microfabrication: the science of miniaturization*. New York: CRC Press, 2002, pp. 195-196.

[20] M. Shikida, M. Ando, Y. Ishihara, T. Ando, K. Sato, and K. Asaumi, "Non-photolithographic pattern transfer for fabricating pen-shaped microneedle structures," *Journal of Micromechanics and Microengineering,* vol. 14, no. 11, pp. 1462-1467, 2004.

[21] K. C. Dee, D. A. Puleo, and R. Bizios, *An introduction to tissue-biomaterial interactions*. Hoboken, NJ: Wiley, 2002, pp. 4-5.

[22] M. J. N. Cormier, A. S. Nat, A. P. Neukermans, and B. Block, "Device for enhancing transdermal agent delivery or sampling," U.S. Patent 6,230,051, May 8, 2001.

[23] J. A. Matriano, M. Cormier, J. Johnson, W. A. Young, M. Buttery, K. Nyam, and P. E. Daddona, "Macroflux microprojection array patch technology: A new and efficient approach for intracutaneous immunization," *Pharmaceutical Research,* vol. 19, no. 1, pp. 63-70, January 2002.

[24] M. Cormier, B. Johnson, M. Ameri, K. Nyam, L. Libiran, D. D. Zhang, and P. Daddona, "Transdermal delivery of desmopressin using a coated microneedle array patch system," *Journal of Controlled Release,* vol. 97, no. 3, pp. 503-11, July 7 2004.

[25] W. Martanto, S. P. Davis, N. R. Holiday, J. Wang, H. S. Gill, and M. R. Prausnitz, "Transdermal Delivery of Insulin Using Microneedles in Vivo," *Pharmaceutical Research,* vol. 21, no. 6, pp. 947-952, June 2004.

[26] J. H. Park, M. G. Allen, and M. R. Prausnitz, "Biodegradable polymer microneedles: fabrication, mechanics and transdermal drug delivery," *Journal of Controlled Release,* vol. 104, no. 1, pp. 51-66, May 2005.

[27] A. U. Daniels, M. K. Chang, and K. P. Andriano, "Mechanical Properties of Biodegradable Polymers and Composites Proposed for Internal Fixation of Bone," *Journal of Applied Biomaterials,* vol. 1, no. 1, pp. 57-78, Spring 1990.

[28] J.-H. Park, Y.-K. Yoon, S.-O. Choi, M. R. Prausnitz, and M. G. Allen, "Tapered conical polymer microneedles fabricated using an integrated lens technique for transdermal drug delivery," *IEEE Transactions on Biomedical Engineering,* vol. 54, no. 5, pp. 903-913, May 2007.

[29] S. P. Sullivan, N. Murthy, and M. R. Prausnitz, "Minimally Invasive Protein Delivery with Rapidly Dissolving Polymer Microneedles," *Advanced Materials,* vol. 20, no. 5, pp. 933-938, 2008.

[30] J. W. Lee, J. H. Park, and M. R. Prausnitz, "Dissolving microneedles for transdermal drug delivery," *Biomaterials,* vol. 29, no. 13, pp. 2113-24, May 2008.

[31] S. P. Sullivan, D. G. Koutsonanos, M. Del Pilar Martin, J. W. Lee, V. Zarnitsyn, S. O. Choi, N. Murthy, R. W. Compans, I. Skountzou, and M. R. Prausnitz, "Dissolving polymer microneedle patches for influenza vaccination," *Nature Medicine,* vol. 16, no. 8, pp. 915-20, Aug 2010.

[32] *Dermaroller S.a.r.l. | Official Site* [Online]. Available: dermaroller.com/en/home (Accessed October 24, 2011).

[33] M. M. Badran, J. Kuntsche, and A. Fahr, "Skin penetration enhancement by a microneedle device (Dermaroller) in vitro: dependency on needle size and applied formulation," *European Journal of Pharmaceutical Sciences,* vol. 36, no. 4-5, pp. 511-23, March 2009.

[34] *Zosano Pharma - Home* [Online]. Available: zosanopharma.com (Accessed October 24, 2011).

[35]H. J. G. E. Gardeniers, R. Luttge, E. J. W. Berenschot, M. J. d. Boer, S. Y. Yeshurun, M. Hefetz, R. v. t. Oever, and A. v. d. Berg, "Silicon micromachined hollow microneedles for transdermal liquid transport," *Journal of Microelectromechanical Systems,* vol. 12, no. 6, pp. 855-862, December 2003.

[36] B. Stoeber and D. Liepmann, "Two-Dimensional Arrays of Out-of-Plane Needles," in *2000 ASME International Mechanical Engineering Congress and Exposition*, Orlando, FL, USA, 2000, pp. 355-9.

[37] B. Stoeber and D. Liepmann, "Arrays of hollow out-of-plane microneedles for drug delivery," *Journal of Microelectromechanical Systems,* vol. 14, no. 3, pp. 472-9, June 2005.

[38] N. Roxhed, T. C. Gasser, P. Griss, G. A. Holzapfel, and G. Stemme, "Penetration enhanced ultrasharp microneedles and prediction on skin interaction for efficient transdermal drug delivery," *Journal of Microelectromechanical Systems,* vol. 16, no. 6, pp. 1429-1440, December 2007.

[39] N. Baron, J. Passave, B. Guichardaz, and G. Cabodevila, "Investigations of development process of high hollow beveled microneedles using a combination of ICP RIE and dicing saw," *Microsystem Technologies,* vol. 14, no. 9-11, pp. 1475-1480, 2008.

[40] S. P. Davis, W. Martanto, M. G. Allen, and M. R. Prausnitz, "Hollow metal microneedles for insulin delivery to diabetic rats," *IEEE Transactions on Biomedical Engineering,* vol. 52, no. 5, pp. 909-15, May 2005.

[41] K. Kim, D. S. Park, H. M. Lu, W. Che, K. Kim, J.-B. Lee, and C. H. Ahn, "A tapered hollow metallic microneedle array using backside exposure of SU-8," *Journal of Micromechanics and Microengineering,* vol. 14, no. 4, pp. 597-603, 2004.

[42] K. Lee, H. C. Lee, D. S. Lee, and H. Jung, "Drawing lithography: three-dimensional fabrication of an ultrahigh-aspect-ratio microneedle," *Advanced Materials,* vol. 22, no. 4, pp. 483-6, Jan 26 2010.

[43] C. G. Li, C. Y. Lee, K. Lee, and H. Jung, "An optimized hollow microneedle for minimally invasive blood extraction," *Biomedical Microdevices,* vol. 15, no. 1, pp. 17-25, February 2013.

[44] P. E. Laurent, S. Bonnet, P. Alchas, P. Regolini, J. A. Mikszta, R. Pettis, and N. G. Harvey, "Evaluation of the clinical performance of a new intradermal vaccine administration technique and associated delivery system," *Vaccine,* vol. 25, no. 52, pp. 8833-42, Dec 17 2007.

[45] R. Luttge, E. J. W. Berenschot, M. J. d. Boer, D. M. Altpeter, E. X. Vrouwe, A. v. d. Berg, and M. Elwenspoek, "Integrated lithographic molding for microneedle-based devices," *Journal of Microelectromechanical Systems,* vol. 16, no. 4, pp. 872-884, August 2007.

[46] B. P. Chaudhri, F. Ceyssens, H. P. Neves, A. La Manna, C. Van Hoof, and R. Puers, "Out-of-Plane High strength Polymer Microneedles for Transdermal Drug Delivery," in *33rd Annual International Conference of the IEEE Engineering in Medicine and Biology Society*, Boston, MA, USA, 2011, pp. 3680-3683.

[47] F. Ceyssens, B. P. Chaudhri, C. Van Hoof, and R. Puers, "Fabrication process for tall, sharp, hollow, high aspect ratio polymer microneedles on a platform," *Journal of Micromechanics and Microengineering,* vol. 23, no. 7, p. 075023, June 2013.

[48] P.-C. Wang, S.-J. Paik, J. Kim, S.-H. Kim, and M. G. Allen, "Hypodermic-needle-like hollow polymer microneedle array using UV lithography into micromolds," in *2011 IEEE 24th International Conference on Micro Electro Mechanical Systems*, Cancun, Mexico, 2011, pp. 1039-1042.

[49] S.-J. Paik, S.-H. Kim, P.-C. Wang, B. A. Wester, and M. G. Allen, "Dissolvable-tipped, drug-reservoir integrated microneedle array for transdermal drug delivery," in *2010 IEEE 23rd International Conference on Micro Electro Mechanical Systems*, Hong Kong, China, 2010, pp. 312 - 315.

[50] Z. Xiang, H. Wang, A. Pant, G. Pastorin, and C. Lee, "Development of vertical SU-8 microtubes integrated with dissolvable tips for transdermal drug delivery," *Biomicrofluidics*, vol. 7, no. 2, p. 026502, March 2013.

[51] Y. Choi, M. A. McClain, M. C. LaPlaca, A. B. Frazier, and M. G. Allen, "Three dimensional MEMS microfluidic perfusion system for thick brain slice cultures," *Biomedical Microdevices*, vol. 9, no. 1, pp. 7-13, February 2007.

[52] V. K. Varadan, A. S. Pillai, and D. Mukherji, *Nanoscience and Nanotechnology in Engineering*. Singapore: World Scientific Publishing Company, 2010, pp. 85-86.

[53] F. Pérennès, B. Marmiroli, M. Matteucci, M. Tormen, L. Vaccari, and E. D. Fabrizio, "Sharp beveled tip hollow microneedle arrays fabricated by LIGA and 3D soft lithography with polyvinyl alcohol," *Journal of Micromechanics and Microengineering*, vol. 16, no. 3, pp. 473-479, 2006.

[54] A. Ovsianikov, B. Chichkov, P. Mente, N. A. Monteiro-Riviere, A. Doraiswamy, and R. J. Narayan, "Two photon polymerization of polymer-ceramic hybrid materials for transdermal drug delivery," *International Journal of Applied Ceramic Technology*, vol. 4, no. 1, pp. 22-9, 2007.

[55] A. Doraiswamy, C. Jin, R. J. Narayan, P. Mageswaran, P. Mente, R. Modi, R. Auyeung, D. B. Chrisey, A. Ovsianikov, and B. Chichkov, "Two photon induced polymerization of organic-inorganic hybrid biomaterials for microstructured medical devices," *Acta Biomater*, vol. 2, no. 3, pp. 267-75, May 2006.

[56] I. Mansoor, U. O. Hafeli, and B. Stoeber, "Hollow Out-of-Plane Polymer Microneedles Made by Solvent Casting for Transdermal Drug Delivery," *Journal of Microelectromechanical Systems*, vol. 21, no. 1, pp. 44-52, February 2012.

[57] K. Hansen, S. Burton, and M. Tomai. (2009, September) A Hollow Microstructured Transdermal System (hMTS) for Needle-Free Delivery of Biopharmaceuticals. *Drug Delivery Technology* [Magazine article]. 38-44. Available: drugdeliverytech-online.com/drugdelivery/200909/?pg=39#pg39

[58] K. J. Hansen, J. K. Simons, and T. A. Peterson, "Transdermal delivery of high volume liquid formulations using hollow microstructures," presented at the Annual Meeting of the American Association of Pharmaceutical Scientists, Atlanta, GA, USA, 2008.

[59] S. A. Burton, F. L. Frederickson, K. J. Hansen, R. P. Simmers, P. T. Fenn, and C. S. Moeckly, "Hollow microneedle array and method," US Patent Application 13/128,066, November 17, 2009.

[60]K. L. Yung, Y. Xu, C. Kang, H. Liu, K. F. Tam, S. M. Ko, F. Y. Kwan, and T. M. H. Lee, "Sharp tipped plastic hollow microneedle array by microinjection moulding," *Journal of Micromechanics and Microengineering*, vol. 22, no. 1, p. 015016, January 2012.

[61] G. G. Matthews, *Cellular physiology of nerve and muscle*. Malden, MA: Blackwell Publishing, 2003, pp. 124-126.

[62]J. D. Bronzino, *Medical Devices and Systems*. Boca Raton, FL: CRC Press, 2006, pp. 47-10.

[63] W. Martanto, J. S. Moore, O. Kashlan, R. Kamath, P. M. Wang, J. M. O'Neal, and M. R. Prausnitz, "Microinfusion using hollow microneedles," *Pharmaceutical Research*, vol. 23, no. 1, pp. 104-113, January 2006.

[64] S. A. Burton, C. Y. Ng, R. Simmers, C. Moeckly, D. Brandwein, T. Gilbert, N. Johnson, K. Brown, T. Alston, G. Prochnow, K. Siebenaler, and K. Hansen, "Rapid intradermal delivery of liquid formulations using a hollow microstructured array," *Pharmaceutical Research*, vol. 28, no. 1, pp. 31-40, Jan 2011.

[65] J. Ezell. *BD Soluvia™ Microinjection System Used For First Approved Intradermal Influenza Vaccine in the European Union* [Press release]. Available: bd.com/contentmanager/b_article.asp?Item_ID=23817&ContentType_ID=1&BusinessCode=20001&d=BD+Worldwide&s=&dTitle=&dc=&dcTitle= (Accessed November 14, 2011).

[66] *The MicronJet Needle* [Online]. Available: nanopass.com/content-e.asp?cid=19 (Accessed November 21, 2011).

[67] N.-T. Nguyen and S. T. Wereley, *Fundamentals and Applications of Microfluidics*. Borwood, MA, U.S.A.: Artech House, Inc., 2002, pp. 99-103.

[68] A. del Campo and C. Greiner, "SU-8: a photoresist for high-aspect-ratio and 3D submicron lithography," *Journal of Micromechanics and Microengineering*, vol. 17, no. 6, pp. R81-R95, June 2007.

[69]MicroChem. *SU-8 2000 Permanent Epoxy Negative Photoresist* [Online]. Available: http://microchem.com/pdf/SU-82000DataSheet2025thru2075Ver4.pdf (Accessed August 9, 2013).

[70] R. Yang and W. Wang, "A numerical and experimental study on gap compensation and wavelength selection in UV-lithography of ultra-high aspect ratio SU-8 microstructures," *Sensors and Actuators B: Chemical*, vol. 110, no. 2, pp. 279-288, October 2005.

[71] C.-H. Lin, G.-B. Lee, B.-W. Chang, and G.-L. Chang, "A new fabrication process for ultra-thick microfluidic microstructures utilizing SU-8 photoresist," *Journal of Micromechanics and Microengineering*, vol. 12, no. 5, pp. 590-597, September 2002.

[72] W. H. Teh, U. Dürig, U. Drechsler, C. G. Smith, and H. J. Güntherodt, "Effect of low numerical-aperture femtosecond two-photon absorption on (SU-8) resist for ultrahigh-aspect-ratio microstereolithography," *Journal of Applied Physics*, vol. 97, no. 5, p. 054907, March 2005.

[73]G. Kotzar, M. Freas, P. Abel, A. Fleischman, S. Roy, C. Zorman, J. M. Moran, and J. Melzak, "Evaluation of MEMS Materials of Construction for Implantable Medical Devices," *Biomaterials*, vol. 23, no. 13, pp. 2737-2750, July 2002.

[74] S. Alpert. *Use of International Standard ISO-10993, 'Biological Evaluation of Medical Devices Part 1: Evaluation and Testing'* [Online]. Available: http://www.fda.gov/MedicalDevices/DeviceRegulationandGuidance/GuidanceDocuments/ucm080735.htm (Accessed October 28, 2013).

[75] C. Hassler, T. Boretius, and T. Stieglitz, "Polymers for neural implants," *Journal of Polymer Science Part B: Polymer Physics*, vol. 49, no. 1, pp. 18-33, January 2011.

[76] K. V. Nemani, K. L. Moodie, J. B. Brennick, A. Su, and B. Gimi, "In vitro and in vivo evaluation of SU-8 biocompatibility," *Materials Science and Engineering: C*, vol. 33, no. 7, pp. 4453-4459, October 2013.

[77] G. Voskerician, M. S. Shive, R. S. Shawgo, H. v. Recum, J. M. Anderson, M. J. Cima, and R. Langer, "Biocompatibility and biofouling of MEMS drug delivery devices," *Biomaterials*, vol. 24, no. 11, pp. 1959-1967, May 2003.

[78] S.-H. Cho, H. M. Lu, L. Cauller, M. I. Romero-Ortega, J.-B. Lee, and G. A. Hughes, "Biocompatible SU-8-Based Microprobes for Recording Neural Spike Signals From Regenerated Peripheral Nerve Fibers," *IEEE Sensors Journal*, vol. 8, no. 11, pp. 1830-1836, November 2008.

[79] V. N. Vernekar, D. K. Cullen, N. Fogleman, Y. Choi, A. J. Garcia, M. G. Allen, G. J. Brewer, and M. C. LaPlaca, "SU-8 2000 rendered cytocompatible for neuronal bioMEMS applications," *Journal of Biomedical Materials Research. Part A*, vol. 89, no. 1, pp. 138-151, April 2009.

[80] S. L. Tao, K. C. Popat, J. J. Norman, and T. A. Desai, "Surface Modification of SU-8 for Enhanced Biofunctionality and Nonfouling Properties," *Langmuir*, vol. 24, no. 6, pp. 2631-2636, March 2008.

[81] H. R. Rawls and J. Esquivel-Upshaw, "Restorative Resins," in *Phillips's Science of Dental Materials*, K. J. Anusavice, Ed., 11th ed St. Louis, MO: Saunders Elsevier, 2003, pp. 339-441.

[82] Invenios. *FOTURAN® Photo-Structurable Glass-Ceramics* [Online]. Available: http://invenios.com/products/photo-structurable-glass/ (Accessed October 28, 2013).

[83] S. H. Kravitz, J. H. Flemming, C. F. Schmidt, and D. Ingersoll, "A Quick Reliable and Versatile Method for Creating Microneedles for Bio-Harvesting," in *2004 Joint International Meeting of the Electrochemical Society*, Honolulu, HI, 2004, pp. 308-313.

[84] P. Abgrall and A. M. Gué, "Lab-on-chip technologies: making a microfluidic network and coupling it into a complete microsystem—a review," *Journal of Micromechanics and Microengineering*, vol. 17, no. 5, pp. R15-R49, May 2007.

[85] E. Meng, X. Zhang, and W. Benard, "Additive Processes for Polymeric Materials," in *MEMS Materials and Processes Handbook*, R. Ghodssi and P. Lin, Eds., First ed New York, NY: Springer, 2011, pp. 220-222.

[86] J. S. Kochhar, W. J. Goh, S. Y. Chan, and L. Kang, "A simple method of microneedle array fabrication for transdermal drug delivery," *Drug Development and Industrial Pharmacy*, vol. 39, no. 2, pp. 299-309, February 2013.

[87] E. J. Tarte, J. J. FitzGerald, N. Lago, S. Benmerah, J. Serra, C. P. Watling, R. E. Cameron, S. P. Lacour, S. B. McMahon, and J. W. Fawcett, "The Spiral Peripheral Nerve Interface: Design, Fabrication and Performance," in *5th European Conference of the International Federation for Medical and Biological Engineering*, Budapest, Hungary, 2011, pp. 1338-1341.

[88] P. Jothimuthu, A. Carroll, A. A. S. Bhagat, G. Lin, J. E. Mark, and I. Papautsky, "Photodefinable PDMS thin films for microfabrication applications," *Journal of Micromechanics and Microengineering*, vol. 19, no. 4, p. 045024, April 2009.

[89] L. Y. Chu and M. R. Prausnitz, "Separable arrowhead microneedles," *Journal of Controlled Release*, vol. 149, no. 3, pp. 242-249, February 2011.

[90] J. Sandby-Moller, T. Poulsen, and H. C. Wulf, "Epidermal thickness at different body sites: relationship to age, gender, pigmentation, blood content, skin type and smoking habits," *Acta Dermato-Venereologica*, vol. 83, no. 6, pp. 410-413, November 2003.

[91] H. S. Gill, D. D. Denson, B. A. Burris, and M. R. Prausnitz, "Effect of microneedle design on pain in human volunteers," *Clinical Journal of Pain*, vol. 24, no. 7, pp. 585-594, September 2008.

[92] D. Arenholt-Bindslev, R. Jolanki, and L. Kanerva, "Diagnosis of Side Effects of Dental Materials, with Special Emphasis on Delayed and Immediate Allergic Reactions," in *Biocompatibility of Dental Materials*, G. Schmalz and D. Arenholt-Bindslev, Eds., First ed Berlin, German: Springer, 2009, pp. 335-366.

[93] S. A. Campbell, "Optical Lithography," in *The Science and Engineering of Microelectronic Fabrication*, Second ed New York NY Oxford University Press, 2001, pp. 151-182.

[94] S. Kuo and Y. Chou, "A Novel Polymer Microneedle Arrays and PDMS Micromolding Technique," *Tamkang Journal of Science and Engineering*, vol. 7, no. 2, pp. 95-98, 2004.

[95] H. Fruhstorfer, G. Schmelzeisen-Redeker, and T. Weiss, "Capillary blood sampling-relation between lancet diameter- lancing pain and blood volume," *European Journal of Pain*, vol. 3, no. 4, pp. 283-286, December 1999.

[96] J. Gupta, E. Felner, and M. Prausnitz, "Minimally Invasive Insulin Delivery in Subjects with Type 1 Diabetes Using Hollow Microneedles," *Diabetes Technology & Therapeutics*, vol. 11, no. 7, pp. 329-337, July 2009.

[97] *BD Pen Needles* [Online]. Available: http://www.bd.com/us/diabetes/page.aspx?cat=7002&id=7409 (Accessed October 31, 2013).

[98] T. R. Kucklick, "Introduction to Needles and Cannulae," in *The Medical Device R&D Handbook*, T. R. Kucklick, Ed., Second ed Boca Raton, FL: CRC Press, 2013, pp. 43-64.

[99] J. H. Park and M. R. Prausnitz, "Analysis of Mechanical Failure of Polymer Microneedles by Axial Force," *Journal of the Korean Physical Society*, vol. 56, no. 4, pp. 1223-1227, April 2010.

[100] SUSSMicroTec. *MA/BA 6: Manual High Precision Mask & Bond Aligner* [Online]. Available: http://www.suss.com/fileadmin/user_upload/brochures/BR_MABA6_2012_V1.pdf (Accessed November 1, 2013).

[101] SUSSMicroTec. *Mask Aligner MA6* [Online]. Available: http://www.coltronics.com.au/DATA/MA6.pdf (Accessed November 1, 2013).

[102] T. C. Merkel, V. I. Bondar, K. Nagai, B. D. Freeman, and I. Pinnau, "Gas Sorption Diffusion and Permeation in PDMS," *Journall of Polymer Science: Part B: Polymer Physics*, vol. 38, no. 3, pp. 415-434, February 2000.

[103] M. S. Rogalski and S. B. Palmer, *Advanced University Physics*. Boca Raton, FL, USA: CRC Press, 2005, pp. 411-428.

[104] B. H. Ong, X. Yuan, and S. C. Tjin, "Adjustable refractive index modulation for a waveguide with SU-8 photoresist by dual-UV exposure lithography," *Applied Optics,* vol. 45, no. 31, pp. 8036-8039, 2006.

[105] S. Owega, D. Poitras, and K. Faid, "Solid-state optical coupling for surface plasmon resonance sensors," *Sensors and Actuators B: Chemical,* vol. 114, no. 1, pp. 212-217, 2006.

[106] N. J. Giordano, *College Physics: Reasoning and Relationships*. Stamford, CT: Cengage Learning, 2010, pp. 448.

[107] A. Govindaraju, A. Chakraborty, and C. Luo, "Reinforcement of PDMS masters using SU-8 truss structures," *Journal of Micromechanics and Microengineering,* vol. 15, no. 6, pp. 1303-1309, 2005.

[108] R. Feng and R. J. Farris, "Influence of processing conditions on the thermal and mechanical properties of SU8 negative photoresist coatings," *Journal of Micromechanics and Microengineering,* vol. 13, no. 1, pp. 80-88, 2003.

[109] Y. S. Shin, K. Cho, S. H. Lim, S. Chung, S. Park, C. Chung, D. Han, and J. K. Chang, "PDMS-based micro PCR chip with Parylene coating," *Journal of Micromechanics and Microengineering,* vol. 13, no. 5, pp. 768-774, September 2003.

[110] B. Valeur and M. N. Berberan-Santos, "Molecular Fluorescence: Principles and Applications," Second ed Weinheim, Germany: Wiley-VCH Verlag & Co., 2012, pp. 39-45.

[111] M. Despont, H. Lorenz, N. Fahrni, J. Brugger, P. Renaud, and P. Vettiger, "High-aspect-ratio, ultrathick, negative-tone near-UV photoresist for MEMS applications," in *1997 IEEE 10th International Conference on Micro Electro Mechanical Systems,* Nagoya, Japan, 1997, pp. 518-522.

[112] H. Lorenz, M. Despont, N. Fahrni, J. Brugger, P. Vettiger, and P. Renaud, "High-aspect-ratio, ultrathick, negative-tone near-UV photoresist and its applications for MEMS," *Sensors and Actuators A: Physical,* vol. 64, no. 1, pp. 33-39, January 1998.

[113] Y.-K. Yoon, J.-W. Park, and M. G. Allen, "Polymer-Core Conductor Approaches for RF MEMS," *Journal of Microelectromechanical Systems,* vol. 14, no. 5, pp. 886-894, October 2005.

[114] K. Wouters and R. Puers, "Diffusing and swelling in SU-8: insight in material properties and processing," *Journal of Micromechanics and Microengineering,* vol. 20, no. 9, p. 095013, September 2010.

[115] Y.-K. Yoon, J.-H. Park, F. Cros, and M. G. Allen, "Integrated vertical screen microfilter system using inclined SU-8 structures," in *IEEE Sixteenth Annual International Conference on Micro Electro Mechanical Systems,* Kyoto, Japan, 2003, pp. 227-230.

[116] J. Kim, M. G. Allen, and Y.-K. Yoon, "Computer-controlled dynamic mode multidirectional UV lithography for 3D microfabrication," *Journal of Micromechanics and Microengineering,* vol. 21, no. 3, p. 035003, 2011.

[117] S. Rajaraman, M. A. McClain, S. O. Choi, J. D. Ross, S. P. DeWeerth, M. C. LaPlaca, and M. G. Allen, "Three-dimensional metal transfer micromolded microelectrode arrays (MEAs) for in-vitro brain slice recordings," in *Transducers '07 & Eurosensors XXI,* Lyon, France, 2007, pp. 1251-1254.

[118] S. Rajaraman, J. A. Bragg, J. D. Ross, and M. G. Allen, "Micromachined three-dimensional electrode arrays for transcutaneous nerve tracking," *Journal of Micromechanics and Microengineering,* vol. 21, no. 8, p. 085014, June 2011.

[119] B. D. Gates, Q. Xu, M. Stewart, D. Ryan, C. G. Willson, and G. M. Whitesides, "New Approaches to Nanofabrication: Molding, Printing, and Other Techniques," *Chemical Reviews,* vol. 105, no. 4, pp. 1171-1196, April 2005.

[120] P. A. Hammond and D. R. S. Cumming, "Encapsulation of a liquid-sensing microchip using SU-8 photoresist," *Microelectronic Engineering,* vol. 73-74, pp. 893-897, June 2004.

[121] X. Wang, Y. Chen, S. Banu, H. Morgan, S. Fu, and Z. Cui, "High density patterns fabricated in SU-8 by UV curing nanoimprint," *Microelectronic Engineering,* vol. 84, no. 5-8, pp. 872-876, May-August 2007.

[122] Z. Li and R. J. Goitz, "Biomechanical evaluation of the motor function of the thumb," *Technology and Health Care,* vol. 11, no. 4, pp. 233-243, 2003.

[123] J. Gupta, S. S. Park, B. Bondy, E. I. Felner, and M. R. Prausnitz, "Infusion pressure and pain during microneedle injection into skin of human subjects," *Biomaterials,* vol. 32, no. 28, pp. 6823-6831, October 2011.

[124] M. A. Meyers and K. K. Chawla, *Mechanical Behavior of Materials*, First ed. Upper Saddle River, NJ: Prentice-Hall, 1998, pp. 412-416.

[125] S. D. Senturia, *Microsystem Design*. Norwell, MA: Kluwer Academic Publishers, 2001, pp. 196-197.

[126] C. Suryanarayana, *Experimental Techniques in Materials and Mechanics*. Boca Raton, FL, USAS: CRC Press, 2011, pp. 338-339.

[127] M. A. Meyers and K. K. Chawla, *Mechanical Behavior of Materials*, Second ed. Cambridge, UK: Cambridge University Press, 2009, pp. 205-208.

[128] M. R. King and N. A. Mody, *Numerical and Statistical Methods for Bioengineering*. New York, NY: Cambridge University Press, 2010, pp. 244-249.

[129] S. P. Davis, B. J. Landis, Z. H. Adams, M. G. Allen, and M. R. Prausnitz, "Insertion of microneedles into skin: measurement and prediction of insertion force and needle fracture force," *Journal of Biomechanics,* vol. 37, no. 8, pp. 1155-1163, August 2004.

[130] E. Forvi, M. Soncini, M. Bedoni, F. Rizzo, M. Casella, C. O'Mahony, and F. Gramatica, "A method to determine the margin of safety for microneedles arrays," in *The World Congress on Engineering 2010*, London, U.K., 2010, pp. 1550-1554.

[131] L. Vedrine, W. Prais, P. E. Laurent, C. Raynal-Olive, and M. Fantino. (2003, May) Improving needle-point sharpness in prefillable syringes. *Medical device technology*. 32-35.

[132] A. Jaber, G. B. Bozzato, L. Vedrine, W. A. Prais, J. Berube, and P. E. Laurent, "A novel needle for subcutaneous injection of interferon beta-1a: effect on pain in volunteers and satisfaction in patients with multiple sclerosis," *BMC Neurology*, vol. 8, no. 1, p. 38, October 10 2008.

[133] R. K. Sivamani, B. Stoeber, G. C. Wu, H. Zhai, D. Liepmann, and H. Maibach, "Clinical microneedle injection of methyl nicotinate: Stratum corneum

penetration," *Skin Research and Technology*, vol. 11, no. 2, pp. 152-156, May 2005.

[134] T. Frisk, N. Roxhed, and G. Stemme, "MEMS for medical technology applications," in *Conference on MEMS Adaptive Optics*, San Jose, CA, USA, 2007, pp. 646513-1-9.

[135] P. Zhang, C. Dalton, and G. A. Jullien, "Design and fabrication of MEMS-based microneedle arrays for medical applications," *Microsystem Technologies*, vol. 15, no. 7, pp. 1073-1082, 2009.

[136] M. R. Prausnitz, J. A. Mikszta, M. Cormier, and A. K. Andrianov, "Microneedle-based Vaccines," in *Vaccines for Pandemic Influenza*, R. W. Compans and W. A. Orenstein, Eds., 1st ed Dordrecht, The Netherlands: Springer, 2009, pp. 369-393.

[137] Y.-K. Yoon, J.-H. Park, and M. G. Allen, "Multidirectional UV Lithography for Complex 3-D MEMS Structures," *Journal of Microelectromechanical Systems*, vol. 15, no. 5, pp. 1121-1130, October 2006.

[138] T. A. Anhoj, A. M. Jorgensen, D. A. Zauner, and J. Hübner, "The effect of soft bake temperature on the polymerization of SU-8 photoresist," *Journal of Micromechanics and Microengineering*, vol. 16, no. 9, pp. 1819-1824, September 2006.

[139] S. Keller, G. Blagoi, M. Lillemose, D. Haefliger, and A. Boisen, "Processing of thin SU-8 films," *Journal of Micromechanics and Microengineering*, vol. 18, no. 12, p. 125020, December 2008.

[140] S. A. Campbell, "Diffusion," in *The Science and Engineering of Microelectronic Fabrication*, Second ed New York NY Oxford University Press, 2001, pp. 39-64.

[141] B. P. Chaudhri, F. Ceyssens, P. De Moor, C. Van Hoof, and R. Puers, "A high aspect ratio SU-8 fabrication technique for hollow microneedles for transdermal drug delivery and blood extraction," *Journal of Micromechanics and Microengineering*, vol. 20, no. 6, p. 064006, June 2010.

[142] P. Khanna, K. Luongo, J. A. Strom, and S. Bhansali, "Sharpening of hollow silicon microneedles to reduce skin penetration force," *Journal of Micromechanics and Microengineering*, vol. 20, no. 4, p. 045011, April 2010.

[143] O. Olatunji, D. B. Das, M. J. Garland, L. Belaid, and R. F. Donnelly, "Influence of array interspacing on the force required for successful microneedle skin penetration: theoretical and practical approaches," *Journal of Pharmaceutical Sciences,* vol. 102, no. 4, pp. 1209-1221, April 2013.

[144] M. S. Lhernould, C. Gobillon, and P. Lambert. (2013, March / April) Microneedle Array Penetration Tests: Understanding The "Bed Of Nails" Phenomenon. *ONdrugDelivery*. 29-32. Available: http://www.ondrugdelivery.com/publications/Transdermal_Microneedles_NFI_March_2013/ULB.pdf

[145] F. M. White, *Fluid Mechanics*, 7th ed. New York, NY, USA: McGraw-Hill, 2011, pp. 19, 20, 25-28, 152, 268-273, 352-354, 357, 388-394.

[146] K. V. Sharp and R. J. Adrian, "Transition from laminar to turbulent flow in liquid filled microtubes," *Experiments in Fluids,* vol. 36, no. 5, pp. 741-747, May 2004.

[147] M. C. Potter and D. C. Wiggert, *Mechanics of Fluids*, 2nd ed. Upper Saddle River, NJ, USA: Prentice-Hall, Inc., 1997, pp. 96, 97, 100.

[148] V. L. Streeter, E. B. Wylie, and K. W. Bedford, *Fluid Mechanics*, 9th ed. Boston, MA, USA: WCB/McGraw-Hill, 1998, pp. 270-271.

[149] J. Gupta, "Microneedles for transdermal drug delivery in human subjects," Ph.D. dissertation, School of Chemical & Biomolecular Engineering, Georgia Institute of Technology, Atlanta, GA, U.S.A., 2009.

[150] B. Massey and J. Ward-Smith, *Mechanics of Fluids*, 7th ed. Cheltenham, UK: Stanley Thornes Ltd, 1998, pp. 274-278.

[151] J. B. Roemer. *Tips and Tools for Insulin Pump Use* [Online]. Available: http://www.diabetesselfmanagement.com/articles/kids-and-diabetes/tips-and-tools-for-insulin-pump-use/all/ (Accessed August 25, 2013).

[152] 3M. *3M™ Hi-Tack Medical Transfer Adhesive 1504XL* [Online]. Available: http://solutions.3m.com/wps/portal/3M/en_US/Medical-Devices-NA/Home/Products/Product-Catalog/~/3M-Hi-Tack-Medical-Transfer-Adhesive-1504XL-4-0-mil-62-Liner?N=4294701151+5515306&Nr=AND%28hrcy_id%3AT3Q9LPXN5Ngs_Q

KNJ3CK8J8_N2RL3FHWVK_GPD0K8BC31gv%29&rt=d (Accessed August 3, 2013).

[153] H. S. Tan and W. R. Pfister, "Pressure-sensitive adhesives for transdermal drug delivery systems," *Pharmaceutical Science & Technology Today*, vol. 2, no. 2, pp. 60-69, February 1999.

[154] *Use of International Standard ISO-10993, 'Biological Evaluation of Medical Devices Part 1: Evaluation and Testing'* [Online]. Available: http://www.fda.gov/downloads/MedicalDevices/DeviceRegulationandGuidance/GuidanceDocuments/UCM348890.pdf (Accessed November 2, 2013).

[155] *Biological evaluation of medical devices* [Online]. Available: http://www.iso.org/iso/home/store/catalogue_tc/catalogue_tc_browse.htm?commid=54508 (Accessed November 2, 2013).

VITA

Po-Chun "Kirk" Wang

Kirk was born and grew up in Taipei, Taiwan. He received the B.S. degree in Electronics Engineering from National Chiao-Tung University, Hsin-Chu, Taiwan, in 1997 and the M.S. degree in Electrical Engineering from Pennsylvania State University, State College, PA, in 2002. His master thesis is entitled "V/Al/Pt/Au Low Resistance Ohmic Contacts to n-type AlGaN/GaN Heterostructures," and his thesis advisor is Prof. Suzanne Mohney.

From 2002 to 2007, he was with Taiwan Semiconductor Manufacturing Company, Hsin-Chu, Taiwan, where he enhanced yield and performance of silicon CMOS integrated circuits. In August 2007, he came to the Georgia Institute of Technology in pursuit of his Ph.D. degree. He joined Prof. Mark Allen's research group in January 2008. His Ph.D. research focuses on fabrication and characterization of micromachined hollow polymer needle arrays for drug delivery into skin.